Title
Annual and interannual evolution of Eighteen Degree Water and oxygen in the western North Atlantic

Author
Billheimer, Samuel

Publication Date
2016

UNIVERSITY OF CALIFORNIA, SAN DIEGO

Annual and interannual evolution of Eighteen Degree Water and oxygen in the western North Atlantic

A Dissertation submitted in partial satisfaction of the
requirements for the degree
Doctor of Philosophy

in

Oceanography

by

Samuel James Billheimer

Committee in charge:

Professor Lynne Talley, Chair
Professor Andreas Andersson
Professor Dean Roemmich
Professor Dan Rudnick
Professor Sutanu Sarkar

2016

The Dissertation of Samuel James Billheimer is approved, and it is acceptable in quality and form for publication on microfilm and electronically:

Chair

University of California, San Diego

2016

TABLE OF CONTENTS

LIST OF FIGURES

LIST OF TABLES

ACKNOWLEDGEMENTS

I would like to thank Lynne Talley for her guidance during my time at Scripps. She has gone above and beyond her role as research adviser with extraordinary mentorship and approachability. Many thanks are due to my committee for their role in shaping this dissertation, in particular Andreas Andersson for his enthusiasm and helpful conversation. I would also like to acknowledge the CLIMODE group, in particular Terry Joyce for his helpful comments and discussion, while Young-Oh Kwon and Jamie Palter also contributed to helpful discussions. Yui Takeshita deserves acknowledgement for his help with delayed mode calibration of the CLIMODE float oxygen data, along with Todd Martz for helpful suggestions and discussion. I would like to acknowledge the CLIVAR repeat hydrography program for giving me the opportunity to go to sea twice as a student. In particular chief scientists Jim Swift and Ruth Curry deserve thanks. Finally I would like to thank all of my professors, friends, and colleagues at Scripps who have supported me and taught me so much, making my time there truly enjoyable.

Chapter 2 is a reprint of the material as it appears in Billheimer, S., and L. D. Talley (2013), Near cessation of Eighteen Degree Water renewal in the western North Atlantic in the warm winter of 2011-2012, *J. Geophys. Res. Oceans*, 118(12), 68386853 (Copyright of the American Geophysical Union 2013). The dissertation author was the primary researcher and first author.

Chapter 3 is a reprint of the material as it appears in Billheimer, S., and L. D. Talley (2016), Annual cycle and destruction of Eighteen Degree Water, *J. Geophys. Res. Oceans*, doi:10.1002/2016JC011799 (Copyright of the American Geophysical Union 2016). The dissertation author was the primary researcher and first author.

VITA

2007	B. A. in Mathematics, Reed College
2011	M.S. Oceanography, Scripps Institution of Oceanography, University of California, San Diego
2016	Ph.D. Oceanography, Scripps Institution of Oceanography, University of California, San Diego

PUBLICATIONS

Billheimer, S., and L. D. Talley (2016), Annual cycle and destruction of Eighteen Degree Water, *J. Geophys. Res. Oceans*, doi:10.1002/2016JC011799.

Billheimer, S., and L. D. Talley (2016), Extraordinarily weak Eighteen Degree Water production concurs with strongly positive North Atlantic Oscillation in late winter 2014/15 [in "State of the Climate in 2015"], *Bull. Amer. Meteor. Soc.*, 97(8), S78-S79.

Billheimer, S., and L. D. Talley (2013), Near cessation of Eighteen Degree Water renewal in the western North Atlantic in the warm winter of 2011-2012, *J. Geophys. Res. Oceans*, 118(12), 68386853.

ABSTRACT OF THE DISSERTATION

Annual and interannual evolution of Eighteen Degree Water and oxygen in the western North Atlantic

by

Samuel James Billheimer

Doctor of Philosophy in Oceanography

University of California, San Diego, 2016

Professor Lynne Talley, Chair

Eighteen Degree Water (EDW), the subtropical mode water of the western North Atlantic, is a voluminous, weakly-stratified upper ocean water mass that is formed via a global extreme in ocean-to-atmosphere heat exchange. In this dissertation, data from Argo profiling floats and the CLIVAR Mode Water Dynamics Experiment (CLIMODE) observational campaign are used to quantify EDW formation strength and to identify the relevant mechanisms that drive the interannual variation in EDW renewal. Evaluating the Sargasso Sea buoyancy budget from 2004-2012, we find that interannual changes in winter buoyancy removal, and thus EDW renewal, are more significantly associated with late winter surface forcing than changes in lateral oceanic heat transport.

Next, observations from Argo together with acoustically-tracked, isothermally-bound profiling CLIMODE "bobbers" are used to investigate the dominant processes that drive the large annual erosion of EDW and quantify EDW destruction rates. We find that EDW destruction is dominated by 1-D vertical diffusion, while mesoscale, along-isopycnal stirring is also significant, explaining approximately 1/3 of the total annual EDW destruction, particularly in the northern Sargasso Sea where larger potential vorticity gradients and enhanced mesoscale activity exist.

Finally, we employ CLIMODE profiling floats equipped with oxygen sensors to determine the structure and seasonality of oxygen evolution in the Sargasso Sea and evaluate the physical processes that modify the distribution of oxygen. Applying estimates of vertical mixing estimated from the previous EDW destruction component of the dissertation, we are able to determine the seasonality and depth-dependence of net biological production and consumption and obtain an estimate of the remineralization of organic carbon that occurs in the region.

Chapter 1

Introduction

The Gulf Stream and Kuroshio Extension are the largest oceanic heat loss regions in the northern hemisphere. Associated with that enormous winter cooling are deep winter mixed layers, which become what we call subtropical mode water.

Mode waters constitute a large portion of the volumetric distribution of the upper ocean and are comprised of nearly uniform temperature and salinity. These water masses outcrop during winter, at which point they are stamped with the current atmospheric conditions. Vigorous convection drives the creation of deep mixed layers that entrain heat, freshwater, and anthropogenic CO_2 into the upper ocean. When air-sea heat flux changes sign in late summer, the upper ocean begins to restratify, and the thick subtropical mode water layer is isolated from the atmosphere by the development of a seasonal pycnocline. In subsequent winters, when the seasonal pycnocline breaks down, it exposes a thick layer of nearly uniform temperature set by previous winters heat loss to the atmosphere, which renews the mode water.

Eighteen Degree Water (EDW) is the subtropical mode water associated with the Gulf Stream Extension in the western North Atlantic [*Worthington*, 1959]. EDW volume and properties are affected both regionally by the Gulf Stream and by large-scale atmospheric conditions.

The strength of EDW formation during winter is strongly associated with the North Atlantic Oscillation (NAO) [*Talley*, 1996; *Joyce et al.*, 2000]. During strongly negative NAO index winters, the ocean-to-atmosphere heat flux that produces deep mixed layers occurs primarily in the subtropical regions [*Dickson et al.*, 1996], resulting in vigorous EDW formation. During strongly positive NAO winters, vigorous buoyancy forcing occurs in the subpolar regions and the subtropical EDW region is deprived of strong winter atmospheric forcing, resulting in weak to near cessation of EDW formation.

The Gulf Stream also plays a role in EDW formation. Strong lateral and vertical shears within the Gulf Stream jet modify convective processes, driving cross-frontal mixing [*Joyce et al.*, 2009, 2013; *Thomas et al.*, 2013]. The entrainment of fresh slope water originating north of the Gulf Stream, which occurs approximately between 65W and 55W, produces a colder, fresher variety of EDW. This mechanism of EDW formation is apparently much less affected by the intensity of winter subtropical surface heat flux [*Billheimer and Talley*, 2013].

The interannual variability of EDW formation has implications for the nutrient supply to the euphotic zone in the Sargasso Sea, modifying annual net productivity [*Palter et al.*, 2005], and may have a significant impact on the CO_2 uptake variability in the North Atlantic [*Bates*, 2012]. Despite the implications, the relative contributions of processes that modulate the vigor and extent of EDW renewal are unclear. Furthermore, the EDW layer acts as an interannually persistent subsurface reservoir of heat, nutrients, and CO_2, but nearly half of its volume is mixed away seasonally, diffusing its properties into the thermocline [*Kwon and Riser*, 2004]. The mechanisms that drive the seasonal dispersal and erosion of the layer are also poorly understood.

The CLIVAR Mode Water Dynamics Experiment (CLIMODE) [*Marshall et al.*, 2009] was an observational campaign designed to address these questions of EDW formation and destruction. From 2004 to 2007, the Sargasso Sea was intensively surveyed using and array of ship-board hydrography, profiling floats, drifters, moorings, a towed CTD platform, and buoys monitoring air-sea interaction. This dissertation focuses on the use of CLIMODE hydrography, profiling floats, and acoustically-tracked, isothermally bound "bobbers" that profiled temperature in the EDW layer.

Nine CLIMODE profiling floats were equipped with optode oxygen sensors in addition to CTDs. The development of stable, profiling float oxygen sensors in recent years provides unprecedented temporal resolution and spatial coverage for observing seasonal oxygen cycles.

In what follows, we address the following questions:

- What is the relative influence of oceanic heat transport vs. atmospheric forcing in driving the interannual variability of EDW renewal strength?
- What is the annual cycle of EDW erosion, and what are the dominant mechanisms that drive the seasonal restratification of the layer?
- How do physical processes, including the annual erosion of EDW, affect the seasonal cycle of oxygen in the Sargasso Sea, and what is the resulting influence on the determination of regional remineralization rates?

In Chapter 2 we show that the winter of 2011-2012 was an extraordinarily weak EDW renewal season. To determine the reasons why, we compare the wintertime oceanic and atmospheric conditions of winter 2011-2012 with those of the previous winters for which there are sufficient oceanic observations from the Argo array of profiling floats and construct the buoyancy budget in the EDW region during the Argo era.

In Chapter 3, we use Argo float data to quantify the seasonality of EDW destruction and to construct the EDW potential vorticity budget, which is used to obtain an estimate for vertical eddy diffusivity. CLIMODE “bobber” data and the Roemmich-Gilson Argo climatology are then used to determine the relative influence of vertical vs. along-isopycnal mixing in the seasonal restratification of the EDW layer.

In Chapter 4, oxygen observations from CLIMODE profiling floats are used to describe the seasonal oxygen structure of the upper ocean of the Sargasso Sea and calculate a seasonal rate of change. We apply estimates of vertical diffusivity obtained in Chapter 3 to evaluate the role of mixing in the evolution of oxygen and estimate biologically-driven net community production and remineralization.

Chapter 2

Near-cessation of Eighteen Degree Water renewal in the western North Atlantic in the warm winter of 2011-2012

2.1 Abstract

The winter of 2011-2012 was a particularly weak season for the renewal of "Eighteen Degree Water" (EDW), the subtropical mode water of the western North Atlantic, as demonstrated by Argo and repeat hydrography. Weak, late winter buoyancy forcing produced shallower than usual winter mixed layers throughout the subtropical gyre, failing to thoroughly ventilate the underlying mode water, and can likely be attributed to the coinciding high, positive phase of the North Atlantic Oscillation (NAO). The only region where EDW was renewed was in the far northeastern Sargasso Sea where it is understood that the Gulf Stream plays a central role in formation; no EDW formed over the large regions of the gyre where deep winter mixed layers driven by surface buoyancy loss normally create EDW.

The present investigation evaluates 2011-2012 winter buoyancy content anomalies, surface buoyancy fluxes, and advection of buoyancy via the Gulf Stream and compares them with the previous seven winters that exhibited more vigorous EDW formation. The weak 2011-2012 formation did not result from increased Gulf Stream heat advection, and was also not driven by preconditioning as the buoyancy content of the region prior to the onset of winter forcing was not unusually high. Rather, the weak formation resulted from climatologically weak surface cooling late in winter. The winter of 2007-2008 also experienced particularly weak EDW formation under similar conditions, including a high NAO and weak late winter surface cooling.

2.2 Introduction

Mode Waters are upper ocean water masses characterized by a thick, vertically homogeneous layer, occupying a mode in the volumetric T/S distribution. The Subtropical Mode Water (STMW) present in the western North Atlantic is usually referred to as Eighteen Degree Water (EDW). EDW renewal is traditionally viewed as being dominated by wintertime surface buoyancy forcing, whereby ocean buoyancy loss to the atmosphere (surface cooling) leads to deep convection, destroying the seasonal pycnocline and ventilating the pre-existing, low potential vorticity (PV) EDW below, which resides above the permanent pycnocline [*Worthington*, 1959]. Recent studies argue that large vertical and lateral shears within the Gulf Stream also contribute to EDW formation by modifying convective processes and stimulating cross-frontal mixing [*Joyce et al.*, 2009, 2013]. Within the Gulf Stream frontal region, between approximately 65 °W and 55 °W, the entrainment of low-salinity slope water produces a slightly colder, fresher variety of EDW, compared to the aforementioned 1-D production of warm-salty EDW to the south and west within the tight recirculation of the subtropical gyre. Regardless of the formation mechanism, recently formed EDW may be subducted via lateral induction and advected to remote regions of the subtropical gyre, where it could possibly be renewed the following year.

The interannual variability of STMW formation is significant in the context of climate. EDW ventilation variability affects the short term storage of anthropogenic CO_2 in the North Atlantic [*Bates et al.*, 2002; *Bates*, 2012] and modulates the nutrient supply to the surface layer, modifying annual primary production and the vigor of the spring bloom [*Palter et al.*, 2005]. Furthermore, STMW volumes and properties represent an oceanographic "memory" of climatic conditions, reflecting temporal variations in wintertime atmospheric forcing at the formation region as well as the larger scale variations of climate indexes and oceanic heat transport [*Kwon and Riser*, 2004; *Dong et al.*, 2007]. In particular, *Joyce et al.* [2000] show that EDW formation intensity is closely related to the NAO and Gulf Stream separation latitude via the associated winter storm tracks and SST anomalies in the subtropical gyre, respectively.

We show here that the exceptionally warm winter of 2011-2012 in the eastern United States [*NOAA National Climatic Data Center*, 2012; *Knutson et al.*, 2013; *Peterson et al.*, 2013] coincided with near-cessation of Sargasso Sea mixed layers with EDW properties, hence any widespread renewal of the upper ocean layer. Based on the record of EDW observed at Bermuda station "S" starting in 1954, lack of EDW renewal is extremely unusual, with evidence of only a few occurrences during a strongly positive NAO in the mid-1970s [*Talley and Raymer*, 1982; *Talley*, 1996; *Joyce et al.*, 2000]. Analyses of interannual EDW volume provide further evidence that winters with such limited EDW formation are rare [*Kelly and Dong*, 2013; *Forget et al.*, 2011; *Maze et al.*, 2009]. Additionally, *Knutson et al.* [2013] find that March-May 2012 anomalous warmth over the eastern United States, extending over the Gulf Stream region in the North Atlantic, was particularly extreme relative to the record extending back to 1851.

A number of processes, examined in what follows, could have been responsible for the 2011-2012 EDW anomaly: 1) Prior to the onset of winter, an excess of heat and stratification in the upper water column would precondition the subtropical gyre to resist the vigorous mixing required to renew the underlying mode water. 2) Throughout the course of the winter, abnormally excessive advection of warm Gulf Stream water into the formation region would provide the same resistance. 3) Abnormally weak winter surface buoyancy forcing alone or combined with 1 and/or 2 would inhibit convection, leaving the EDW layer unventilated.

In this study, we compare the wintertime oceanic and atmospheric conditions of winter 2011-2012 with those of the previous winters for which there are sufficient oceanic observations from the Argo array of profiling floats beginning in 2004. We focus on comparison with a "normal" EDW formation year, 2006-2007, during which a greater number of hydrographic observations were made as a part of the CLIvar MOde Water Dynamic Experiment (CLIMODE) [*Marshall et al.*, 2009]. In Section 3, mixed layer properties obtained from Argo float profiles are used to show that EDW outcropping was nearly non-existent during the formation season in 2012, and only marginally appeared in the eastern part of the subtropical gyre. These observations are supplemented by comparison of hydrographic sections from March 2012 and March 2007. In Section 4, EDW formation intensity is quantified in terms of buoyancy content and a buoyancy budget is introduced to establish the contributions of surface vs. lateral fluxes of buoyancy. The budget is constructed using two independent approaches, using mapped Argo and using the ECCO state estimate, both revealing the importance of weak surface buoyancy forcing in late winter

2011-2012, and the general importance of late winter surface forcing for EDW renewal. Finally, in section 5, we relate interannual variations in EDW formation intensity from 2004 to 2012 to net winter cumulative surface buoyancy loss and the phase of the North Atlantic Oscillation (NAO).

2.3 Data

2.3.1 Profiling float data

Argo is an array of profiling floats that monitor temperature and salinity in the upper 2000 m of the global ocean, with a significant number of profiles in the northwestern Atlantic beginning in 2004. Nine additional Argo-type profiling floats, including oxygen measurements, were deployed in this region as part of CLIMODE (http://www-pord.ucsd.edu/climode_apexfloats/). We take advantage of all floats in the region with quality control flag "good". For the calculation of vertically integrated density and buoyancy transport via geostrophic currents (fields incorporated into the buoyancy budget), we use the Roemmich-Gilson (RG) gridded Argo temperature and salinity fields [*Roemmich and Gilson*, 2009], which are objectively mapped from quality controlled Argo profiles from 2004 to the present on a uniform, $1^\circ \times 1^\circ$ grid with monthly temporal resolution. Since the RG objective mapping of temperature and salinity is performed on pressure levels, spurious overturns are present in the resulting density field. For the present analysis, these spurious overturns are removed and replaced by linear interpolation. RG Argo is also used to calculate the Gulf Stream "north wall," which is defined by the location of the $15\,^\circ$C isotherm at 200 m depth [*Fuglister*, 1963; *Joyce et al.*, 2000].

2.3.2 Ship-based hydrography

Hydrographic sections of temperature, salinity, oxygen, nutrients, and carbon parameters were collected by the U.S. Climate Variability and Predictability and Carbon (USCLIVAR/CO2) Repeat Hydrography occupations of 52 °W (A20) and along the line from Woods Hole to Bermuda (A22) (*http://ushydro.ucsd.edu/*); data are available from the CLIVAR and Carbon Hydrographic Data Office or CCHDO (*http://cchdo.ucsd.edu*). A20 and A22 are compared with a section along approximately 66 °W composed of stations from the CLIMODE 4 hydrographic survey performed in March 2007 (*http://www-pord.ucsd.edu/ ltalley/climode_ctdhydro/*), which included temperature, salinity, oxygen and nutrient sampling. Water masses along the original occupations of A20 and A22 in 1997 are described by *Joyce et al.* [1999].

2.3.3 Air-sea fluxes and sea surface properties

Air-sea fluxes are drawn from NCEP/NCAR Reanalysis 1 [*Kalnay et al.*, 1996]. Precipitation rate, net longwave and shortwave radiation, and latent and sensible heat fluxes are monthly on a T62 Gaussian grid ($1.9047^\circ \times 1.875^\circ$ in the subtropics). We calculate evaporation rate [m/s] using the formulation $E = Q_{lh}/(\rho_0 L_e)$ [*Yu*, 2007], where Q_{lh} is daily latent heat flux [W/m^2] and $\rho_0 = 1000$ kg/m^3, the reference density for seawater. L_e is the latent heat of vaporization, $L_e = [2.501 - (0.00237 \times SST)] \times 10^6$, using sea surface temperature (SST) from the optimally interpolated $1/4^\circ$ daily sea surface temperature from *Reynolds et al.* [2007] decimated to colocate with the coarser NCEP reanalysis grid. Evaporation rates are then monthly averaged. Surface fluxes are combined with sea surface salinity from the NCEP Global Ocean Data Assimilation System (GODAS, *http://www.esrl.noaa.gov/psd/*) to calculate the surface buoyancy flux, B_{surf} (negative for ocean buoyancy loss), defined as the sum of heat and freshwater flux contributions [*Gill*, 1982]:

$$B_{surf} = \frac{\alpha g}{\rho_0 c_p} Q - \beta g S(E-P), \tag{2.1}$$

where α and β are the thermal expansion and saline contraction coefficients, ρ_0 is the reference density, c_p is the specific heat for seawater, S is the sea surface salinity, $E-P$ is the net evaporation minus precipitation rate [m/s], and Q is the net surface heat flux (negative for ocean heat loss, W/m^2).

2.3.4 Absolute dynamic topography

Surface geostrophic velocities are calculated from $1/3^\circ$ maps of absolute dynamic topography, the SSALTO/DUACS product distributed by Aviso (*http://www.aviso.oceanobs.com/duacs/*). Weekly maps of dynamic topography were interpolated onto the RG Argo grid, averaged monthly, and then finally used to calculate a reference geostrophic velocity at the surface.

2.3.5 ECCO state estimate

We employ the ECCO state estimate, provided by the ECCO Consortium for Estimating the Circulation and Climate of the Ocean funded by the National Oceanographic Partnership Program (NOPP), in order to determine the volume balance in the western North Atlantic, as well as to assess the sensitivity of the buoyancy budget to geostrophic transports derived from Argo and altimetry. In particular, we employ JPL ECCO (*http://ecco.jpl.nasa.gov/external/*), which provides 10-day output at 1-degree zonal and meridional resolution in our study region.

We elect to use Argo as our primary data source, as the state estimate has some deficiencies in the Gulf Stream region (see section 4.4). Relative to ship-based hydrography and Argo float profiles, EDW is not well represented by ECCO as ECCO is too dense and too well-stratified at EDW depths. Furthermore, the Gulf Stream separation latitude in ECCO is too far to the south.

2.4 Observations of weak EDW in spring 2012

Winter mixed layer densities provide both a measure of the severity of wintertime mixing and a proxy for EDW outcropping, provided that the mixed layer density is within the typical EDW density range. The winter of 2011-2012 exhibited shallow mixed layers with a density well below this range, suggesting a winter lacking severity and one in which EDW was not ventilated.

A potential density range of $\sigma_\theta = 26.2 - 26.7$ kg/m^3 and a salinity range of $36.3 < S < 36.7$ psu are used here to identify EDW mixed layers, in which EDW from years past is supposed to be renewed or new EDW is actively being formed. A low planetary PV ($\equiv -\frac{f}{\rho}\frac{\partial\rho}{\partial z}$, [m^{-1}s^{-1}]) signature is the dynamical characteristic of all STMWs, and PV sections across the subtropical gyre of the N. Atlantic (Fig. 2.1) show that the chosen density range is appropriate for EDW, spanning the low PV (PV$< 10^{-10}$ m^{-1}s^{-1}) water mass. Furthermore, the chosen ranges are consistent with Bermuda station “S” time series of density and salinity at the EDW core, defined as the PV minimum [*Talley*, 1996].

The signature of “missing” new EDW at the end of winter 2011-2012 was first detected on the US CLIVAR Repeat Hydrography section A22 (Fig. 2.1b), occupied in March, 2012, during the month when formation occurs in almost all years. The CLIMODE March 2007 hydrographic survey (CLIMODE 4, Fig. 2.1a) is useful for comparison, as a year with moderately vigorous EDW formation relative to the 2004-2012 climatology and in accordance with *Joyce et al.* [2013]. In the 2012 sections, it is clear that the seasonal pycnocline, identified as a layer of high PV below the mixed layer and above the EDW layer, remained intact, hence devoid of any sign of EDW outcropping, particularly along A22, which is a location where EDW is normally strongly developed in March. A20, a line further to the east at approximately 52 °W, shows evidence of a single remnant mixed layer at 36.5 °N that may have connected with the underlying EDW layer, but otherwise shows an intact seasonal pycnocline at all other locations (Fig. 2.1c). In 2007, on the other hand, the mixed layer obliterated the seasonal pycnocline, thoroughly ventilating the pre-existing EDW layer; these are the conditions that are usually observed in late winter.

The relatively low EDW oxygen along A22 makes it clear that the EDW layer there was unventilated (Fig. 2.2b,e), as the layer was isolated from surface waters by the intact seasonal pycnocline at approximately 200 – 250 m depth. A20 shows some signs of recent ventilation (Fig. 2.2c, near 36 °N), but has nowhere near the oxygen concentration of the EDW layer along the CLIMODE section in 2007 (Fig. 2.2a,d), which was clearly thoroughly renewed. Phosphate (measured but not shown) inversely reflects the oxygen distribution, with high levels in the EDW layer across A22 in March 2012, low levels in the EDW layer along CLIMODE 4 in March 2007, and a bimodal distribution across A20 in May 2012.

All available Argo profiles from February to April reveal an overall significantly lighter, shallower mixed layer in 2012 than in 2007 (Fig. 2.3). Mixed layers with EDW properties (“EDW mixed layers,” $36.3 < S < 36.7$ psu and $\sigma_\theta > 26.2$ kg/m^3) were prevalent throughout the subtropical gyre in 2007, within the tight recirculation gyre, as far south as Bermuda, and eastward, extending beyond 50 °W. EDW mixed layers in 2012 occurred only in the northern Sargasso Sea, east of 57 °W. Only 5.9% of the observed mixed layers during winter 2012 had EDW properties, considering only profiles south of the Gulf Stream and north of 30 °N, compared to 57% in 2007, indicating dramatically reduced EDW renewal in 2012.

The absence of 2012 EDW mixed layers is clear from T-S diagrams (Fig. 2.4). The very few mixed layers with EDW properties that did exist in 2012 were warmer and fresher than those in the same region in 2007, with mean temperatures of 18.2 °C compared to 18.0 °C, and mean salinities of 36.45 psu compared to 36.54 psu.

The small set of 2012 EDW mixed layers occurred in the "downstream" region of the Gulf Stream Extension, east of 60 °W, and hence may be the result of the aforementioned frontal formation process for EDW [*Joyce et al.*, 2009; *Joyce*, 2012; *Joyce et al.*, 2013]: via cross-frontal mixing, fresher waters from north of the Gulf Stream are expected to contribute to newly formed EDW. It is tempting to attribute the fresher 2012 EDW mixed layers to this formation mechanism, but winter surface forcing could have just as easily contributed to the fresher mixed layers, as local freshwater flux ($E - P$, [m/s]) was 9% weaker in January-February-March (JFM) 2012 than JFM 2007. Furthermore, fresher EDW or surface waters before the onset of winter could have preconditioned fresher winter EDW mixed layers. Cross-frontal EDW formation should not be ruled out, however, because in addition to the E-P changes in 2012, it is not inconsistent for this type of EDW production to have occurred and to have contributed an additional freshwater flux to the observed mixed layers.

It is interesting to note that EDW renewal in February-April 2008 was also weak, with EDW mixed layers also exclusively in the eastern, downstream region of the Gulf Stream (Fig. 2.3d). As shown in the next section, the winter of 2007-2008 was similar to that of 2011-2012, experiencing weak surface buoyancy loss, a strongly positive NAO, and weak EDW renewal.

2.5 Buoyancy Content and Winter Buoyancy Loss

In this section, we develop the buoyancy budget in the western subtropical North Atlantic, within and above the EDW layer. EDW buoyancy content anomaly (BCA) is introduced to quantify the excess buoyancy ($b = -\rho g$, [kg m^{-2} s^{-1}]) that must be removed for EDW outcropping. We then estimate the contributions of surface buoyancy flux and geostrophic advection of buoyancy via the Gulf Stream to changes in winter BCA within the control volume. Other winter buoyancy removal processes, e.g. horizontal Ekman advection, diapycnal diffusion, and/or eddy buoyancy flux, are accounted for in the residual.

2.5.1 Buoyancy Content Anomaly

We find it useful to define an EDW buoyancy content anomaly (BCA) as the vertically integrated difference in buoyancy from a water parcel of potential density $\rho = 1026.7$ kg/m^3:

$$BCA = \frac{1}{\rho_0} \int_{z(\sigma_\theta = 26.7)}^{0} [26.7 - \sigma_\theta(z)]\, g\, dz \tag{2.2}$$

where g is gravitational acceleration (maps in Fig. 2.5). Units are m^2/s^2. We calculate BCA from monthly RG Argo fields, focusing on the region south of the Gulf Stream Extension. A high BCA value indicates that much of the buoyancy in the upper water column must be removed for EDW outcropping, and a value of zero indicates strong EDW ventilation. This quantity incorporates both the stratification above the EDW layer as well as the depth of the bottom of the EDW layer, represented by the $26.7\sigma_\theta$ isopycnal. In the region south of the Gulf Stream Extension, the point-wise correlation between BCA and the depth of

$\sigma_\theta = 26.7$ is significant but not dominant, with the depth of $26.7\sigma_\theta$ accounting for just under a third of the BCA variability. $\sigma_\theta = 26.7$ is a reasonable, conservative choice for the EDW bottom boundary, given that none of the observed 2005-2012 EDW mixed layers exceed this density (Fig. 2.4a-h), the isopycnal lies below the low PV ($< 10^{-10}$ m^{-1}s^{-1}) EDW layer for both 2007 and 2012 hydrographic sections (Fig. 2.1a-c), and the choice is consistent with previous analyses of the historical low PV layer [*Talley*, 1996].

The autumn to late winter difference in BCA is a useful way to quantify the strength of an EDW formation season (maps in Fig. 2.6). We also calculate the area-integrated BCA inventory over the region south of the Gulf Stream Extension that is dashed in Figures 2.5 and 2.6, hence excluding Slope Waters north of the Gulf Stream from the area integral. October BCA maps (Fig. 2.5a,b) indicate a large amount of excess buoyancy above the EDW layer, particularly in the Gulf Stream Extension. By the end of the strong EDW formation season in April 2007 (Fig. 2.5c), much of the domain south of the Gulf Stream appears to have no or very little BCA, indicating EDW formation or renewal, particularly in the region east of 60 °W. In contrast, by April 2012 (Fig. 2.5d), BCA remained at excessive levels throughout the entire domain south of the Gulf Stream, reflecting a weak EDW formation season.

Area-integrated BCAs in February, March, and April (FMA) 2012 and in FMA 2008 are the highest over the eight years of the Argo record (Fig. 2.7a), indicating that both had an unusually large excess of buoyancy in the upper water column. The autumn to late winter total difference in BCA (ΔBCA) distinguishes the 2007-2008 and 2011-2012 EDW formation seasons (Fig. 2.9). Autumn BCA was slightly higher in 2007 than in 2011 (Fig. 2.7a) and so ΔBCA of 2007-2008 exceeds ΔBCA of 2011-2012; thus, 2011-2012 was the weakest year of the eight for winter buoyancy removal.

2.5.2 Preconditioning

Oceanic and atmospheric conditions outside of winter may be important for setting the strength of winter EDW renewal. In the North Pacific, the dynamic state of the Kuroshio Extension is known to have a large influence on setting the stratification of North Pacific Subtropical Mode Water (NPSTMW) [*Qiu and Chen*, 2006], therefore controlling the degree to which the water mass is renewed each winter. The eddy variability produced by an energetic Kuroshio Extension plays a larger role in determining the decadal strength of NPSTMW than year-to-year changes in surface forcing. In the North Atlantic, *Dong et al.* [2007] show that high autumn SST in the subtropical gyre can precondition the water column, inhibiting the formation of EDW during the subsequent winter.

Preconditioning did not play a large role in the 2011-2012 EDW renewal season, but may have influenced the stronger EDW renewal in 2006-2007. Before the onset of winter, 2011 BCA within the Gulf Stream and tight recirculation gyre was large relative to 2006 (Fig. 2.5a,b), which gives the impression that the 2011 water column was predisposed to resist EDW formation. However, relative to the 2004-2011 area averaged BCA envelope and ensemble mean (Fig. 2.7a), the 2006-2007 winter was preconditioned for strong EDW formation with low autumn BCA. The 2006-2007 winter surface forcing was not unusual, yet end of winter BCA was also low (Table 2.2, Fig. 2.7ab). The low autumn BCA in 2006, in the form of either weak EDW stratification or cooler surface temperatures, may have contributed to this low end of winter value in 2007. Comparing autumn 2011 with the climatological mean, area-integrated BCA is just below average, indicating that there were no clear oceanic conditions preforming a particularly weak EDW formation season.

2.5.3 Surface Buoyancy Flux

Surface buoyancy loss (Eq. (2.1)) drives deep mixed layer formation and is central to EDW formation. The accumulation of buoyancy loss through fall and winter is a major factor in determining the mixed layer properties at the end of winter. Here, cumulative surface buoyancy flux, $\int_t B_{surf}$, is taken as the time integral of Eq. (2.1) from October to April.

Geographic patterns of the wintertime cumulation of surface buoyancy flux qualitatively reflect patterns of changes in BCA over the course of the winter. Fig. 2.6d depicts cumulative surface buoyancy loss over the winter of 2011-2012 concentrated near the Gulf Stream west of 60 °W, which mirrors the maximum change in BCA from October to April in that region. Over the winter of 2006-2007, cumulative surface buoyancy loss extends east of 60 °W, where the maximum BCA loss from October to April occurs. These similar patterns in cumulative surface buoyancy loss and BCA loss suggest that changes in surface buoyancy flux contribute to changes in BCA, and that weak, less extensive surface buoyancy flux over the course of the 2011-2012 winter is partially responsible for the lack of EDW formation. One should take into consideration, however, that the surface buoyancy flux and ΔBCA maps in Fig. 2.6 are not identical, particularly in the western domain, revealing that buoyancy transfer processes other than surface buoyancy flux also play a role in BCA changes over the course of the winter.

Time series of regionally averaged cumulative surface buoyancy flux and BCA demonstrate the wintertime progression of surface buoyancy extraction and the degree to which it removes excess buoyancy content (Fig. 2.7). Integration is over the entire domain north of 30 °N and south of the Gulf Stream, which is determined by the location of $T(200\,\mathrm{m}) = 15\,^{\circ}\mathrm{C}$. The northern boundary fluctuates with the Gulf Stream, and therefore introduces a time-varying area of integration. *Dong et al.* [2007] compensate for this by meridionally shifting the southern boundary to maintain a fixed area of integration, but find that using a fixed southern boundary instead has little impact on their conclusions. Here we elect to use a fixed southern boundary, finding that the mean latitude of the Gulf Stream does not significantly contribute to interannual changes in area-integrated surface buoyancy forcing or annual minimum BCA. The area of integration is a measure of Gulf Stream latitude, and is very weakly (and insignificantly) anti-correlated with cumulative winter surface buoyancy flux (r = -0.31, below the 95% significance level of 0.71). The sign of the correlation suggests that a larger integration area (higher Gulf Stream latitude) may be weakly associated with more area-integrated surface buoyancy loss.

As mentioned previously, the 2011-2012 winter had the highest end of winter (March and April) BCA levels and widest autumn to late winter difference in BCA over all eight years on record, indicating that it was the weakest year for EDW renewal from 2004-2012. Over 2011-2012, only 46% of the autumn BCA was lost by the end of winter, compared to 61% BCA loss over the course of the 2006-2007 winter. Greater cumulative surface buoyancy loss to the atmosphere from October 2006 to April 2007 contributes to this difference, as the 2007 to 2012 difference in BCA widens drastically in February as 2012 surface buoyancy loss simultaneously weakens (Fig. 2.7a). The 2011-2012 winter was among the least severe of all eight winters, given that the October through April cumulative surface buoyancy loss is narrowly the second weakest of the eight years for buoyancy loss, second to 2007-2008.

Since the only EDW formation in 2012 occurred far to the east, where EDW is typically fresher and colder than that found in the tight recirculation gyre [*Kwon and Riser*, 2004; *Joyce*, 2012] and may have a formation mechanism other than simple 1-D buoyancy extraction [*Joyce et al.*, 2009; *Joyce*, 2012; *Joyce et al.*, 2013], we consider the western and eastern domains separately, separated by the 60 °W meridian (Fig. 2.7b,c). The average BCA in the eastern domain is overall lower than that in the west, indicating that the region may be more susceptible to EDW outcropping via either surface buoyancy loss or wind-driven cross-frontal exchange. Note that the shallower depth of $26.7\sigma_\theta$ in the eastern domain (white contours, Fig. 2.5) may also contribute to lower BCA there. In the east, the autumns of 2006, 2011, and the eight year mean have very similar BCA, but the gap is widened among all three in late winter due to changes in buoyancy forcing in February. Even though wind-driven instabilities within the Gulf Stream are thought to largely contribute to EDW formation in this region [*Joyce et al.*, 2009; *Thomas et al.*, 2013], this demonstrates the importance of late winter sea-air buoyancy exchange for removing BCA east of 60 °W, and hence for the formation of EDW there.

2.5.4 Geostrophic Buoyancy Flux

Advection of buoyancy via the Gulf Stream provides a positive buoyancy input into the observation region. For every winter over the record, the cumulation of surface buoyancy loss exceeds the September to April loss of BCA (Fig. 2.7). This can only be so if there is a supply of buoyancy throughout the winter feeding excessive surface buoyancy fluxes. Here, we estimate contributions of BCA from the Gulf Stream by calculating the geostrophic BCA flux:

$$B_{geostr} = \frac{1}{\rho_0} \int_y \left(\sum_{\rho_i} u_g(\rho_i) \left[1026.7 - \rho_i\right] g \right) dy \tag{2.3}$$

where the summation is over density layers ρ_i ranging from the lightest observed density up to ρ=1026.7 kg/m^3, with uniform spacing $\Delta\rho = 0.05$ kg/m^3. u_g is the layer geostrophic velocity normal to the boundary and y is the along-boundary (e.g. along 75 °W, 45 °W, 30

°N, or 43 °N) lateral coordinate. Geostrophic velocities are calculated from RG Argo density sections referenced to surface velocities derived from altimetry. Geostrophic transport is likely underestimated by the monthly smoothing of the Gulf Stream jet, which weakens lateral density gradients, thereby weakening geostrophic velocities.

Winter 2011-2012 did not exhibit unusual advection of buoyancy via the Gulf Stream relative to 2006-2007 and the 2004-2011 climatology. Integrating from October to April, the cumulative geostrophic BCA flux was 2.5×10^{12} m^4/s^2 for 2011-2012, compared to 3.0×10^{12} m^4/s^2 in 2006-2007 and 2.5×10^{12} m^4/s^2 on average for 2004-2011.

The volume budget does not close using RG Argo with velocities referenced to satellite SSH, with a surplus convergence of 18 ± 5.8 Sv, which cannot be accounted for with other estimated transports, such as Ekman. This large volume transport imbalance is concerning for its impact on the buoyancy budget, and so we consider separately the buoyancy budget using the ECCO state estimate for the same region. We find that the ECCO volume budget does close using the same geostrophic components, with divergence of geostrophic transport balancing the time rate of change of volume in the control volume bounded by 75 °W, 45 °W, 30 °N, and 43 °N. The Ekman contribution, discussed below, is very small. The ECCO residual is a convergence of 1.6 ± 1.0 Sv. The lack of closure in the RG Argo volume budget probably results from a poor estimate for the reference velocity rather than from neglecting important terms. Regardless, we opt to focus on the RG Argo analysis as it provides a more realistic description of the EDW layer than ECCO. Relative to ship-based hydrography, RG Argo does a better job of reproducing the EDW layer observed during the March 2012 occupation of A22 (Fig. 2.8). ECCO is too dense at EDW depths, and does not represent the weakly stratified layer well. We compensate for this in the ECCO volume budget by redefining the bottom boundary as the σ_θ=27.1 isopycnal rather than

σ_θ=26.7. Thus, ECCO is used here mainly as a diagnostic to assess the dominant terms in the volume budget.

2.5.5 Buoyancy Content Anomaly (BCA) Budget

Consider a control volume bounded by 75 °W, 45 °W, 30 °N, and the Gulf Stream Extension, and bounded below by the σ_θ=26.7 kg/m^3 isopycnal. We model the seasonal change in BCA as being described by the cumulative surface and geostrophic buoyancy fluxes:

$$\Delta\mathcal{BCA} = \int_t \left(\mathcal{B}_{surf} - \nabla\cdot\mathcal{B}_{geostr}\right) dt + res \tag{2.4}$$

where calligraphic lettering indicates area-integrated fields. $\Delta\mathcal{BCA}$ is the annual winter change (April minus the previous September) in area-integrated BCA and the right hand side time integration is from September to April. $\Delta\mathcal{BCA}$ is negative due to buoyancy loss over the course of the winter. $\nabla\cdot\mathcal{B}_{geostr}$ is the divergence of the total geostrophic flux of buoyancy across 75 °W, 45 °W, 30 °N, and 43 °N and $\mathcal{B}_{surf}$ is the area-integrated surface buoyancy flux (negative for ocean buoyancy loss). Note that we use a fixed northern boundary (43 °N) to calculate the divergence of geostrophic transport but that the area of integration for surface buoyancy flux and $\Delta\mathcal{BCA}$ fluctuates with the meanders of the Gulf Stream. The 43 °N latitude is chosen because it lies just north of the maximum winter Gulf Stream latitude from 2004-2012, which is 42.8 °N.

res represents all residual terms of Eq. 2.4, including the effects of diapycnal diffusion, Ekman transport, and poleward eddy buoyancy fluxes out of the control volume. Diapycnal mixing across the bottom boundary σ_θ=26.7 kg/m^3 is a buoyancy sink term (decreases BCA), as the mixing entrains denser fluid from below. Diapycnal diffusivity is likely enhanced within the Gulf Stream [*Inoue et al.*, 2010], but on the gyre scale we assume its effect is limited, as in *Dong et al.* [2007].

Horizontal Ekman advection is another buoyancy sink term, as along-front westerlies generate advection of dense surface subpolar waters southward across the Gulf Stream north wall and into outcropping EDW isopycnal layers [*Thomas*, 2005; *Thomas et al.*, 2013]. In an inverse model formulation similar to Eq. (2.4), *Dong et al.* [2007] find the contribution of Ekman advection to be negligible for describing changes in heat content on interannual time scales, relative to the contributions of geostrophic advection and sea-air heat exchange. We have calculated the winter cumulation of Ekman buoyancy divergence in the control volume and agree that the contribution is negligible (not shown). Inferring Ekman buoyancy transport from NCEP wind stress and RG Argo, we find that the contribution is smaller than the combined error of the other fields in the buoyancy budget, with mean 0.017×10^{12} m^4/s^2 and standard deviation 0.22×10^{12} m^4/s^2. Thus, we do not explicitly include it as a term in Eq. 2.4 or a curve in Fig. 2.9 and leave it to the residual.

Eddy buoyancy flux across the Gulf Stream is also a neglected sink term, given that one should expect a poleward eddy heat flux across the front [*Newton*, 1961; *deSzoeke and Levine*, 1981]. *Wunsch* [1999] finds the eddy heat flux across 36 °N in the upper 300 m (0.06 PW) to be unimportant relative to the total meridional heat flux (1 ± 0.3 PW). A recent estimate of mixed layer poleward eddy heat flux across the Gulf Stream is in agreement [*Hausmann and Czaja*, 2012]. These estimates of heat transport translate to approximately 0.6×10^{12} m^4/s^2 of buoyancy loss from September to April, an order of magnitude below the contributions from surface and geostrophic buoyancy flux and within their combined error. We expect all of the neglected terms discussed above to contribute to buoyancy loss in the region, and should therefore expect a negative residual.

Each side of Eq. (2.4) is calculated, limited by the RG Argo record of eight winters

(Fig. 2.9a). $\Delta\mathcal{BCA}$ and $\int_t \left(\mathcal{B}_{surf} - \nabla\cdot\mathcal{B}_{geostr}\right)$ have a correlation coefficient of $r = 0.57$, below the the 95% significance level of 0.71. Considering the mean of these eight years of data, the BCA budget closes despite the large imbalance in the volume budget:

$$\begin{array}{ccccc} \Delta\mathcal{BCA} & & \int_t \mathcal{B}_{surf} & \int_t -\nabla\cdot\mathcal{B}_{geostr} & res \\ -5.0\pm 0.53 & = & -7.0\pm 0.38 & +2.3\pm 0.55 & -0.34\pm 0.85 \end{array} \tag{2.5}$$

Units are $10^{12}\,\mathrm{m}^4/\mathrm{s}^2$. The residual term of Eq. (2.5) is smaller than the total error, which is propagated from the sum of bootstrap 95% confidence intervals. The residual is negative, which is the sign expected given the neglected processes. It should be noted that $\int_t -\nabla\cdot\mathcal{B}_{geostr}$ is likely an underestimate, given the smoothing of the Gulf Stream by the monthly resolution RG Argo product and AVISO SSH, reducing the magnitude of the geostrophic currents. A correction for this bias, which would increase buoyancy, would drive the residual to be even more negative. Furthermore, it is well documented that NCEP overestimates ocean heat loss and $E - P$, particularly over western boundary currents [*Zeng et al.*, 1998; *Vivier et al.*, 2002; *Cerovečki et al.*, 2011], introducing a bias toward ocean buoyancy loss. Again, a correction for excessive ocean buoyancy loss would result in a more negative residual, further away from zero.

$\Delta\mathcal{BCA}$ is more closely related to surface buoyancy fluxes than to the advection of buoyancy via the Gulf Stream, given that the interannual $\Delta\mathcal{BCA}$ to $\int_t \mathcal{B}_{surf}$ correlation ($r = 0.89$; 95% significance level is 0.71) is much higher than the weak, insignificant $\Delta\mathcal{BCA}$ to $\int_t \mathcal{B}_{geostr}$ correlation ($r = 0.24$). This finding appears to be in contrast to the results of *Dong et al.* [2007], who conclude that the interannual variability in upper ocean heat content is dominated by the anomalous advection of geostrophic currents. On the other hand, they found that mixed layer interannual variability is dominated by surface heat flux.

The analysis here evaluates only winter buoyancy content (September through April), which is probably largely influenced by deep mixed layers occupying much of the water column. Here, a large influence of winter mixed layer temperature on the winter heat content, as opposed to heat content observed throughout the entire annual cycle evaluated by *Dong and Kelly* [2004], is in agreement with the above result that interannual variations in winter heat content are better described by surface heat flux anomalies than anomalies in geostrophic advection. Furthermore, that study is over a smaller region further to the west (limited by data availability), missing much of the EDW formation region where surface forcing plays a larger role.

Constructing the buoyancy budget of Eq. 2.4 using output data from ECCO, the budget closes with similar results (Fig. 2.9b): There is a stronger correlation between $\int_t \mathcal{B}_{surf}$ and ΔBCA (r = 0.93) than between $\int_t -\nabla \cdot \mathcal{B}_{geostr}$ and $\Delta\mathcal{BCA}$ (r = 0.78). Using ECCO, the latter correlation is very much stronger than that using RG Argo (r = 0.24), further suggesting that the lack of closure in the RG Argo volume budget results from a poor estimate for the reference velocity and that lateral buoyancy input may actually play a more important role in the buoyancy budget. In particular, the residual in 2008 is not an extreme outlier in ECCO, suggesting that the large residual in 2008 using RG Argo may be the result of error in the transport estimate. As discussed previously, we opt to focus on the results using RG Argo as that data set provides a better representation of the density and stratification of the EDW layer (Fig. 2.8).

Regardless of the weaker correlation between $\Delta\mathcal{BCA}$ and $\int_t -\nabla \cdot \mathcal{B}_{geostr}$ in both data sets, cumulative geostrophic buoyancy flux is still required to close the budget. Including $\int_t -\nabla \cdot \mathcal{B}_{geostr}$ in Eq. (2.4) reduces the correlation between the right and left hand sides, but it is a significant contribution, making up the difference in magnitude between $\Delta\mathcal{BCA}$ and

$\int_t \mathcal{B}_{surf}$.

The winter of 2011-2012 provides an example of the strong relationship between seasonal BCA fluctuation and cumulative surface buoyancy flux (Table 2.2, Fig. 2.9a). The winter divergence of cumulative geostrophic buoyancy transport was unextraordinary relative to the mean ($\int_{t=2011-2012} -\nabla \cdot \mathcal{B}_{geostr} = 2.1 \times 10^{12}$ m^2/s^2), while 2012 cumulative surface buoyancy flux and the seasonal fluctuation in $\mathcal{BCA}$ were anomalous ($\int_{t=2011-2012} -\nabla \cdot \mathcal{B}_{surf} = -6.5 \times 10^{12}$ m^2/s^2, $\Delta_{2011-2012}\mathcal{BCA} = -3.9 \times 10^{12}$ m^2/s^2). Thus, the anomalously high $\Delta\mathcal{BCA}$ observed in 2012, and hence lack of EDW formation, was likely related to weak winter cumulative surface buoyancy loss rather than stronger winter advective input of buoyancy from the Gulf Stream.

In the same sense, another example of the strong relationship between $\Delta\mathcal{BCA}$ and surface forcing is the winter of 2007-2008 (Table 2.2, Fig. 2.9a). Again, weak EDW renewal ($\Delta\mathcal{BCA}$) occurs with weak surface buoyancy loss ($\int_t \mathcal{B}_{surf}$). The 2007-2008 and 2011-2012 seasons also share a high NAO (Table 2.2, Fig. 2.10b). In the opposite sense, the relation holds for the winter of 2009-2010 (Table 2.2, Fig. 2.9a), with strong winter surface forcing coinciding with a large seasonal $\mathcal{BCA}$ fluctuation. End of winter average BCA was low even though the autumn average BCA was high (Figs. 2.7a, 2.10c), indicating no effects due to preconditioning. The 2010 NAO was was strongly negative, opposing that of 2007-2008 and 2011-2012.

In 2006-2007, neither $\Delta\mathcal{BCA}$ nor $\int_t \mathcal{B}_{surf}$ were unusual (Table 2.2, Fig. 2.9a). Regardless, average BCA was among the lowest by the end of the winter. This suggests that low autumn BCA in 2006 may have preconditioned the water column for more intense EDW renewal.

2.6 Interannual Variability and the NAO

The weak buoyancy forcing observed in late winter 2012 is likely related to the concurrent high phase of the NAO (Fig. 2.10a,b). The high, positive winter NAO during the weak 2011-2012 EDW formation season is consistent with the conclusions of previous investigations linking the NAO with EDW formation strength [*Dickson et al.*, 1996; *Talley*, 1996; *Joyce et al.*, 2000]. In particular, *Joyce et al.* [2000] find a significant correlation between winter NAO and PV at $\sigma_\theta = 26.5$ observed at Station "S" near Bermuda. The $26.5\sigma_\theta$ isopycnal represents the low PV core of the EDW layer [*Talley and Raymer*, 1982; *Talley*, 1996], so higher levels of PV on that isopycnal reflect a weak EDW formation season. In this sense, winters with weak EDW renewal are associated with a high NAO index, with maximum correlation at zero years lag.

Minimum annual BCA in late winter is a comparable measure of annual EDW formation intensity to PV on $\sigma_\theta = 26.5$, as demonstrated by Fig. 2.10c and the significant correlation between the annual winter minima from winters 2004-2012 ($r = 0.72$; 95% significance level is 0.67). Furthermore, winter minimum BCA was significantly correlated with the winter (JFM averaged) NAO over the same time period ($r = 0.73$) with maximum correlation occurring at zero year lag.

There are also strong relationships between the NAO and cumulative surface buoyancy flux (Fig. 2.10a,b) and between the NAO and cumulative buoyancy transport convergence. Using the 30 year time series from 1983 to 2012, winter (JFM) NAO and area integrated cumulative (JFM) NCEP surface buoyancy flux are significantly correlated with correlation coefficient $r = 0.64$ (95% significance level is 0.37). The January through March characterization of winter maximizes the strength of the relationship. From 2005-2012, JFM NAO and ECCO $\int_t -\nabla \cdot \mathcal{B}_{geostr}$ are also significantly correlated with correlation coefficient r

= 0.74 (95% significance level of 0.71). Associations between the NAO and gyre circulation could provide a partial explanation, as *Curry and McCartney* [2001] point out the relation between the NAO and Gulf Stream Extension transport where increased transport occurs with a strongly positive NAO on interannual and decadal time scales. In summary, both surface and geostrophic fluxes are correlated with the NAO, but surface flux makes the dominant contribution to changes in BCA.

It should be noted that the winter of 2007-2008 was very similar to that of 2011-2012 in all respects considered in this study: winter 2007-2008 exhibited a large seasonal fluctuation in $\mathcal{BCA}$ (Fig. 2.9), high late winter, minimum average BCA (Fig. 2.10c), strongly positive NAO (Fig. 2.10a,b), weak late winter surface buoyancy loss (Fig. 2.10b), and a lack of EDW mixed layers observed in the western region of the domain (Fig. 2.3d). The primary difference between the two winters is that autumn 2007 had a slightly higher than average BCA.

2.7 Conclusion

The winter of 2011-2012 was the weakest EDW formation season over at least the past eight years. This is demonstrated by a lack of 2011-2012 winter mixed layers with EDW properties, with only 5.9% in the study region meeting EDW density and salinity criteria in 2012, by far the lowest of the previous eight years, which average 50% with EDW properties. Furthermore, end-of-season BCA was higher in 2012 than any of the past eight years, with only a 46% loss of autumn BCA in 2011-2012 compared to a 60% loss on average.

The location of the few sites at which EDW renewal occurred in 2012, in the northeastern Sargasso Sea near the Gulf Stream, suggests that a frontal formation mechanism remained in play, but the extent to which this mechanism was manifested is unclear.

Autumn 2011 did not have unusual levels of BCA relative to the climatology, thus preconditioning neither a strong nor weak EDW formation year. Also, the cumulation of geostrophic buoyancy transport was not unusually strong through winter 2011-2012, precluding the possibility that an excess of buoyancy was advected into the region by the Gulf Stream over the course of the winter. Thus, the agent most likely responsible for the lack of vigorous EDW formation in 2012 was unusually weak late winter buoyancy loss, particularly east of 60 °W. The anomalously mild late winter was related to the strongly positive phase of the NAO, given that we find the phase of the NAO to be significantly correlated with late winter cumulative surface buoyancy forcing and end of winter BCA, consistent with previous studies [*Dickson et al.*, 1996; *Talley*, 1996; *Joyce et al.*, 2000]. *Knutson et al.* [2013] estimate that anthropogenic forcing contributed about 35% of the 2012 warm anomaly in the region by diagnosing control model run internal variability as natural variability.

Assessing the buoyancy budget from 2004-2012, we find that interannual changes in winter buoyancy removal, and thus EDW renewal, are most significantly associated with winter surface forcing. Constructing a similar budget, *Dong et al.* [2007] find that interannual heat content variability is dominated by oceanic advection of heat rather than by surface forcing. Our study differs from the previous work by exclusively calculating winter anomalies, ignoring the remainder of the year, and by including a larger study region, extending further to the east where surface forcing is more intense.

The significant association of EDW renewal with surface forcing over the years in the analysis is in contrast to the renewal of NPSTMW in the western North Pacific, which is more clearly associated with oceanic preconditioning. *Qiu and Chen* [2006] show that the strength of NPSTMW on decadal scales is far more closely associated with the dynamic state of the Kuroshio Extension, and therefore eddy variability, than with wintertime atmospheric conditions.

EDW imparts the influence of its oceanographic “memory” in that it mediates information from the mixed layers of previous winters. As new winter mixed layers deepen, they entrain underlying EDW, so that the thick, homogeneous mode water substantially affects the properties of the mixed layer [*Dong and Kelly*, 2004]. If there were an extended period of mild winters, one might expect that several years of limited EDW renewal would contribute to warmer winter mixed layers and winter SSTs in the subtropical gyre. In turn, warmer winter mixed layers may influence winter ocean heat loss to the atmosphere by enhancing the air-sea temperature gradient during winter. This closed feedback loop may have occurred in the past, reproducing a modified mode water layer: The EDW layer was nearly eliminated in the mid 1970’s and returned with altered properties, becoming warmer and less dense, which persisted throughout the following two decades [*Talley*, 1996].

2.8 Acknowledgments

The authors wish to thank the reviewers for their helpful comments. They would also like to express appreciation to Ruth Curry, chief scientist of CLIVAR Repeat Hydrography A22, and Michael S. McCartney, chief scientist of A20, for collection of data on those cruises and for the opportunity for Sam Billheimer to participate on A22. Funding was provided by NSF Ocean Sciences OCE-0960928 (‘CLIMODE’) and NSF Ocean Sciences OCE-0752970 (‘U.S. CLIVAR/CO2 Repeat Hydrography’).

Chapter 2 is a reprint of the material as it appears in Billheimer, S., and L. D. Talley (2013), Near cessation of Eighteen Degree Water renewal in the western North Atlantic in

the warm winter of 2011-2012, *J. Geophys. Res. Oceans*, 118(12), 68386853 (Copyright of the American Geophysical Union 2013). The dissertation author was the primary researcher and first author.

Table 2.1: Qualitative buoyancy budget (Eq. 2.4) absolute values with September BCA, winter minimum BCA, and January-February-March NAO. “High,” “Mid,” and “Low” are selected based on the lower, middle, and upper third values over the 2004-2012 RG Argo record.

Year	BCA(autumn)	BCA(winter)	ΔBCA	$\int_t B_{surf}$	$\int_t B_{geostr}$	NAO
2004-05	High	Low	High	Mid	Mid	Mid
2005-06	Mid	Mid	Low	Low	Low	Mid
2006-07	Low	Low	Mid	Low	High	High
2007-08	Mid	High	Low	Low	High	High
2008-09	High	High	Mid	Mid	Mid	High
2009-10	High	Low	High	High	Low	Low
2010-11	Low	Low	Mid	Mid	Low	Mid
2011-12	Mid	High	Low	Low	Mid	High

Table 2.2: Buoyancy budget (Eq. 2.4) numerical values with September BCA and winter minimum BCA. Units are $m^4/s^2 \times 10^{12}$. The January-February-March NAO is also included.

Year	BCA(autumn)	BCA(winter)	ΔBCA	$\int_t B_{surf}$	$\int_t B_{geostr}$	NAO
2004-05	9.05	3.01	-6.04	-7.26	2.52	-0.123
2005-06	8.49	3.28	-4.55	-6.73	1.46	-0.173
2006-07	7.69	2.96	-4.73	-6.85	3.00	0.396
2007-08	8.37	4.15	-4.22	-6.27	3.65	0.567
2008-09	9.31	4.07	-5.23	-7.14	2.76	0.207
2009-10	9.30	2.64	-6.08	-8.14	1.84	-1.32
2010-11	8.14	2.89	-5.22	-7.09	1.34	0.143
2011-12	8.29	4.40	-3.90	-6.49	2.14	0.953

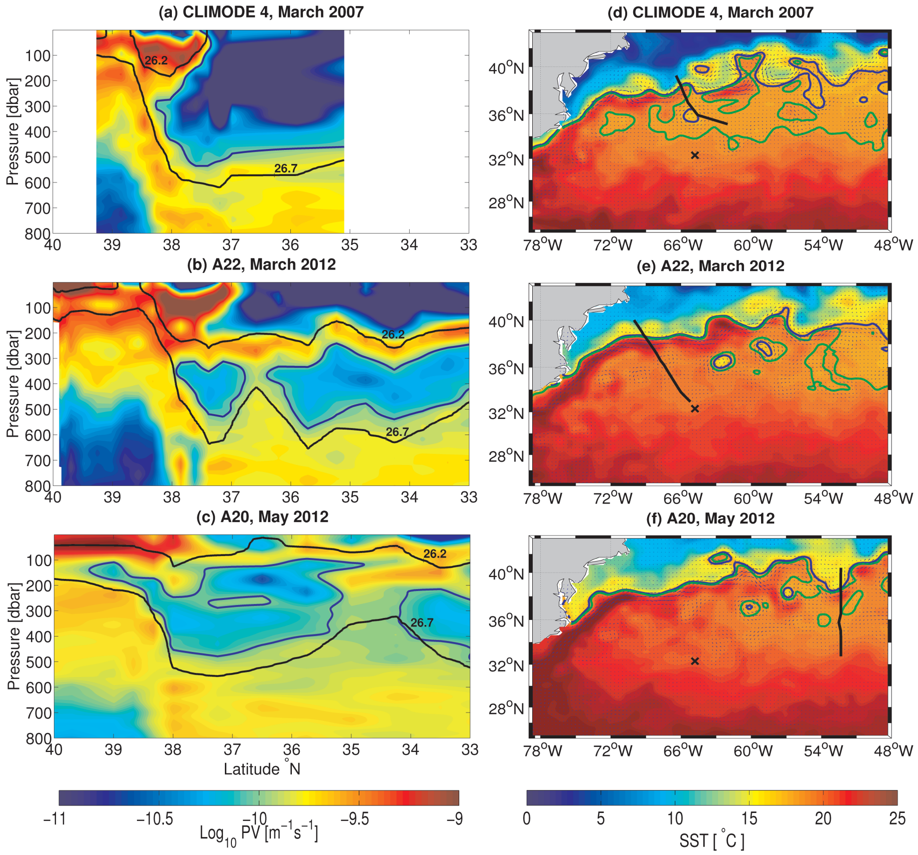

Figure 2.1: Potential vorticity sections. (a)-(c): Potential vorticity sections from CLIMODE 4 (March 2007), A22 (March 2012), and A20 (May 2012). σ_θ contours are in black. Blue contours ($Q = 10^{-10}$ m^{-1}s^{-1}, bounded by 26.2σ_θ and 26.7σ_θ) represent the EDW layer. (d)-(f) SST (color shading) and OSCAR (*http://www.oscar.noaa.gov/*) surface currents (blue arrows) for March 7, 2007, March 27, 2012, and May 7, 2012, the dates when CLIMODE 4, A22, and A20 crossed the Gulf Stream, respectively. The 17.5 °C (green) and 18.5 °C (blue) SST contours are marked, with cruise tracks (black bold) and the location of Bermuda (black "x") also included.

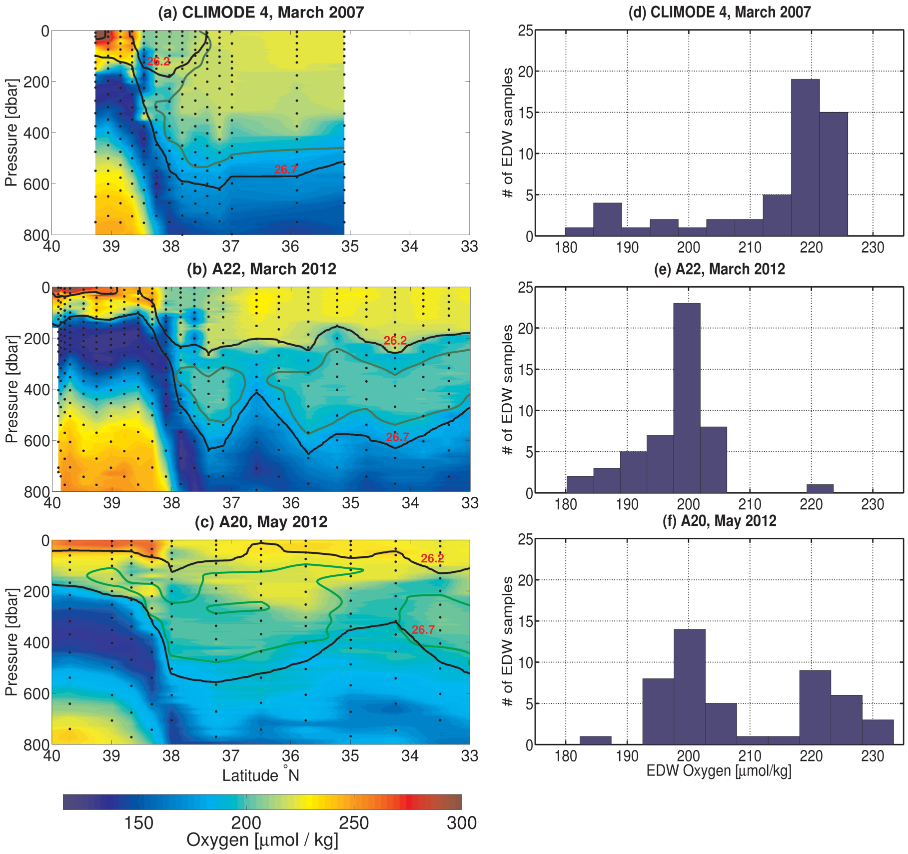

Figure 2.2: Dissolved oxygen sections. (a)-(c): Dissolved oxygen (SBE43) sections from CLIMODE 4 (March 2007), A22 (March 2012), and A20 (May 2012). σ_θ contours are in black. Green contours ($Q = 10^{-10}$ m^{-1}s^{-1}, bounded by 26.2σ_θ and 26.7σ_θ) represent the EDW layer. Black dots are the locations of oxygen bottle samples. (d)-(f): Histograms of EDW bottle oxygen, using the number of oxygen samples found within the EDW layer, which is contoured in (a)-(c).

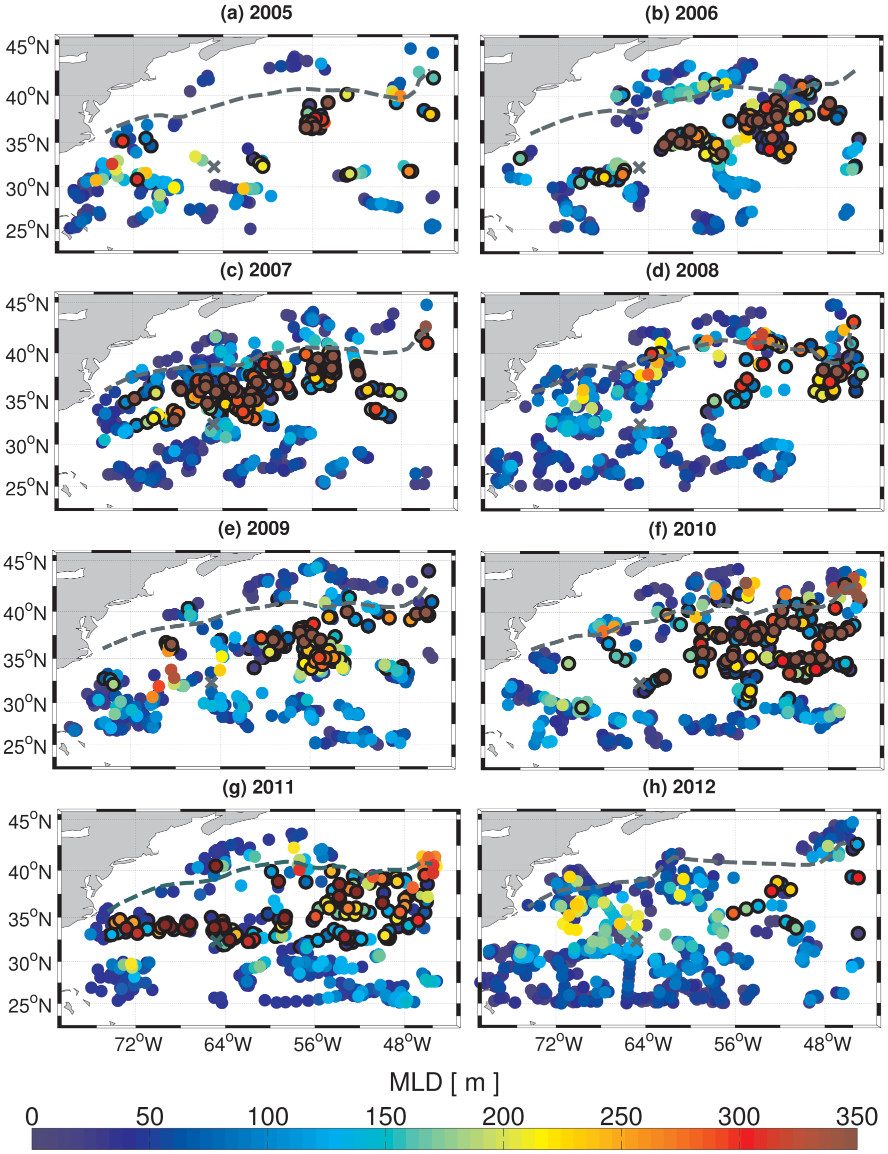

Figure 2.3: Maps of all available Argo profile mixed layers from February - April, 2005-2012, including profiles from nine CLIMODE floats which were deployed in the northern Sargasso Sea in late 2005. Also included are profiles from A22 (March 2012) and CLIMODE 4 (February-March 2007) ship-based hydrography. Bold circles signify mixed layers with $26.2 < \sigma_\theta < 26.7$ and $36.3 < S < 36.7$ psu, indicating EDW formation/renewal. Mixed layer depth (MLD) is defined as the depth for which the density deviates by a threshold of 0.03 kg/m^3 from the density at 10 m [*de Boyer Montégut et al.*, 2004]. Mean February-March-April Gulf Stream position is delineated by the dashed grey curve, defined by the location of $T(z = 200\,\text{m}) = 15\,^\circ\text{C}$ using the RG Argo grid. For reference, the location of Bermuda is represented by a grey “x”.

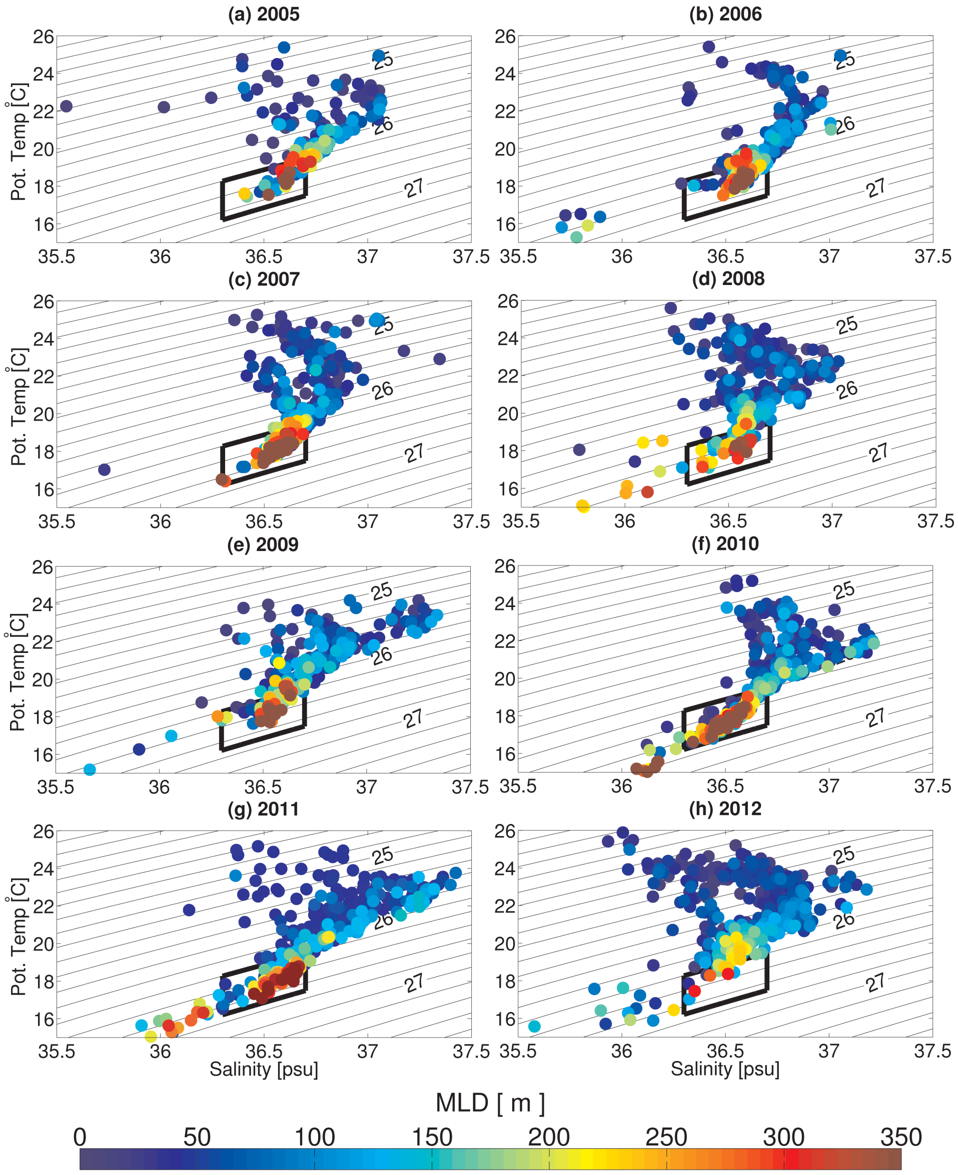

Figure 2.4: Mixed layer T-S diagrams from all float and ship-based profiles displayed in Fig. 2.3. Mixed layers with EDW properties ($26.2 < \sigma_\theta < 26.7$ and $36.3 < S < 36.7$ psu) are contained within the bold, black rectangle and correspond to those with bold circles in Fig. 2.3. Black contour lines represent σ_θ levels.

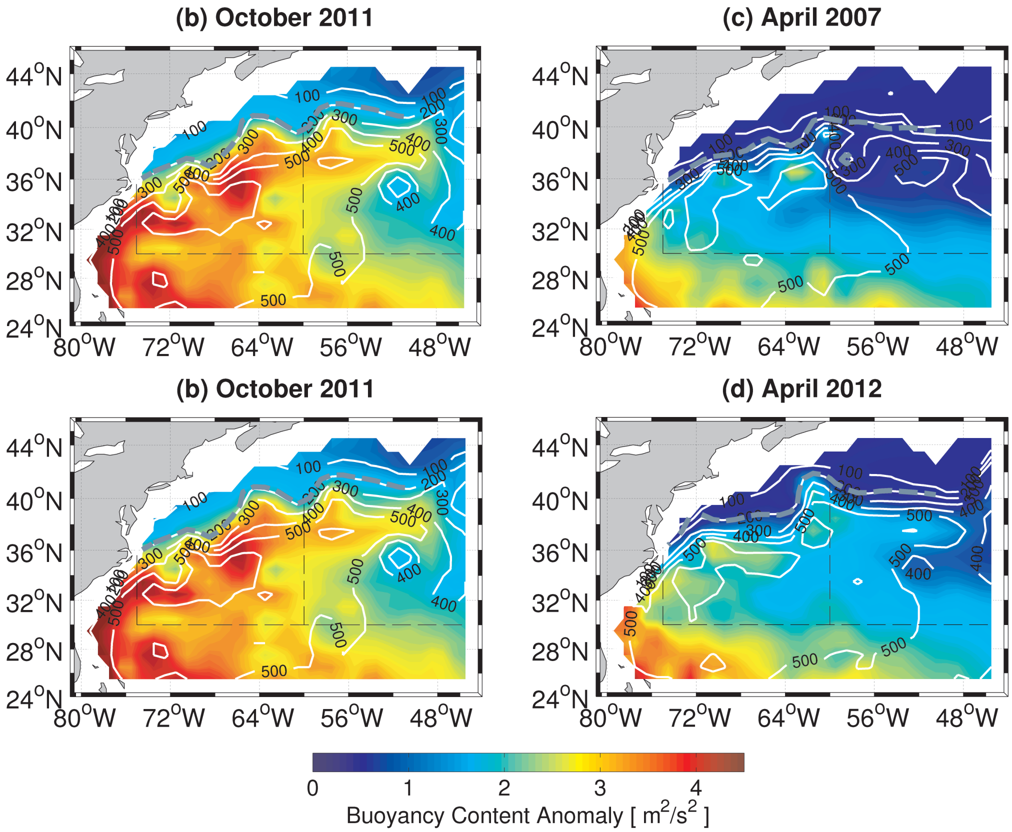

Figure 2.5: Maps of EDW buoyancy content anomaly (BCA), calculated using monthly gridded Argo data (RG) from *Roemmich and Gilson* [2009] (color shading). White contours give the depth of the $\sigma_\theta = 26.7$ isopycnal. The Gulf Stream position is delineated in dashed grey, determined by the location of $T(z = 200\,\mathrm{m}) = 15\,^\circ\mathrm{C}$, calculated monthly from the RG Argo grid. Black dashed lines bound the two "east" and "west" integration domains for Fig. 2.7b,c.

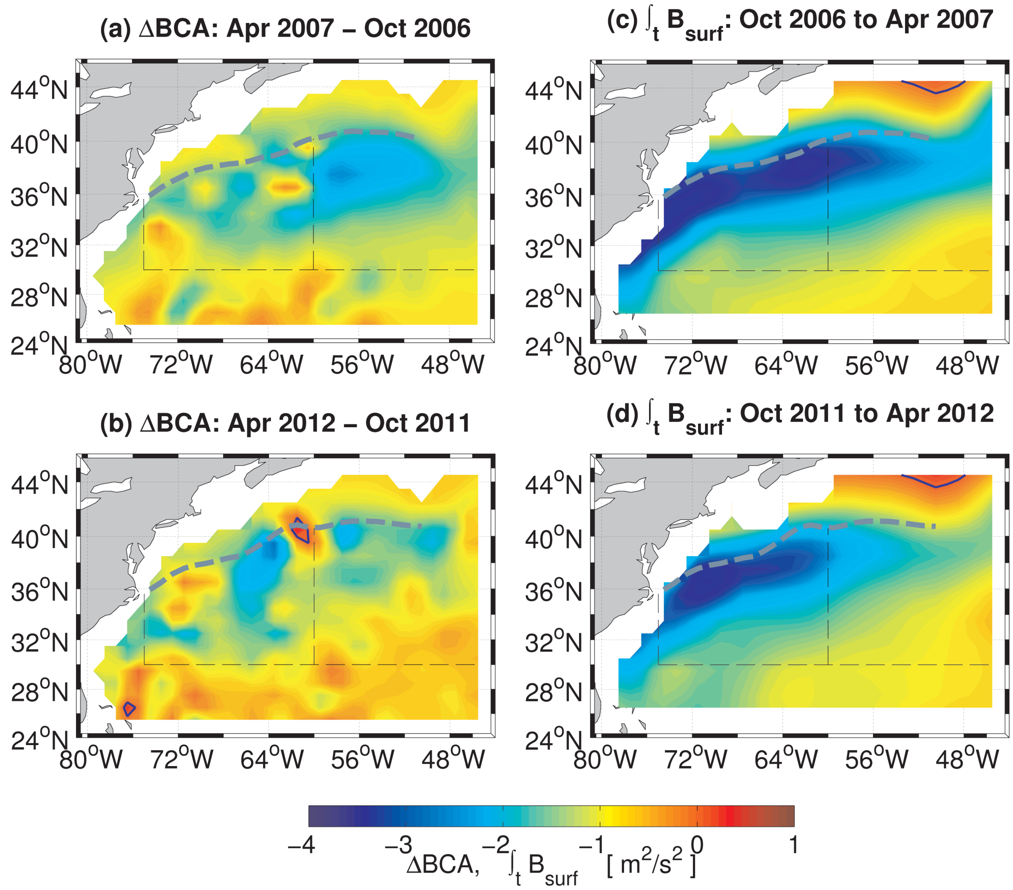

Figure 2.6: Seasonal changes in buoyancy content anomaly. (a),(b): Difference in buoyancy content anomaly (ΔBCA) over the course of the winter (April - October). (c),(d): Cumulative surface buoyancy flux ($\int_t B_{surf}$), integrated from October through April. Negative values indicate ocean buoyancy loss to the atmosphere. Blue curves signify the $\Delta BCA = 0$ and $\int_t B_{surf} = 0$ contours, dashed lines are as in Fig. 2.5, and the dashed grey curve represents the winter averaged Gulf Stream position, determined by the location of $T(z = 200\,\mathrm{m}) = 15\,°\mathrm{C}$, calculated from the RG Argo grid.

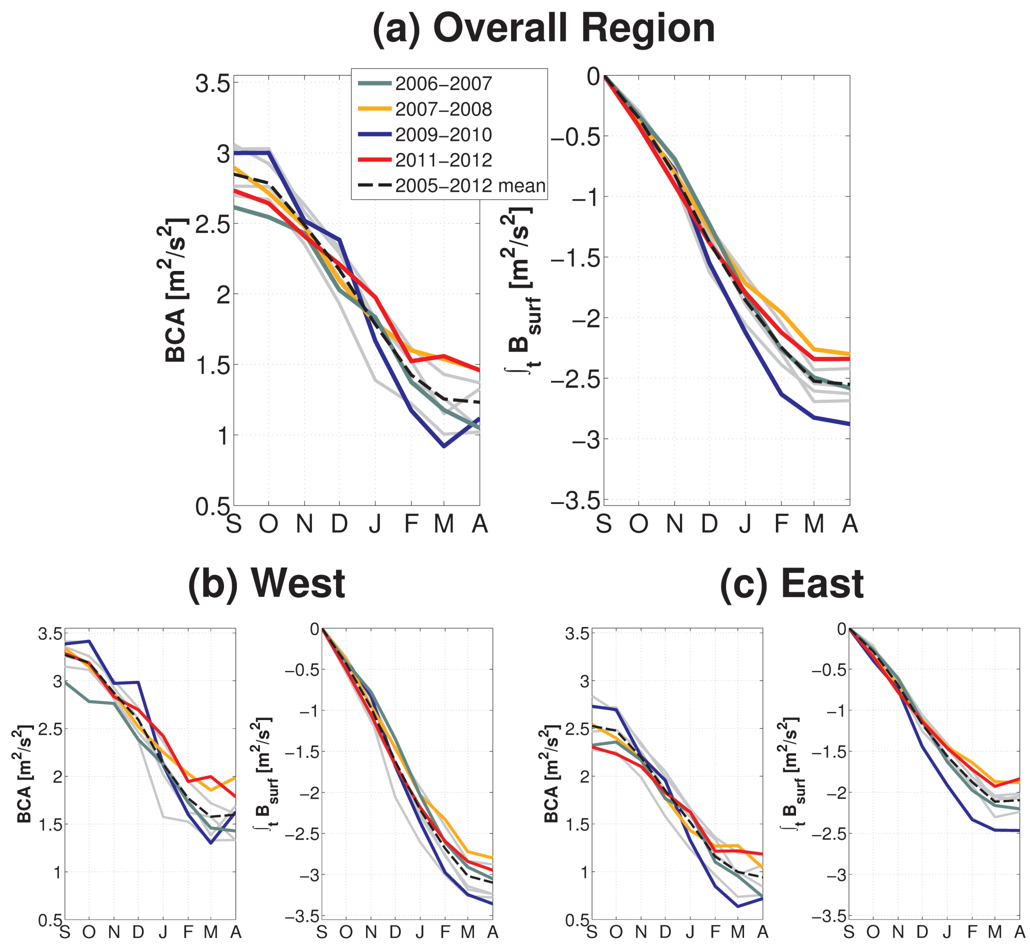

Figure 2.7: Area-averaged buoyancy content anomaly (BCA) and area-averaged cumulative air-sea buoyancy flux ($\int_t B_{surf}$) for September through April, 2005-2012 (grey), with the CLIMODE 4 (2006-2007) and A20/A22 (2011-2012) years highlighted in green and red, respectively. The 2007-2008 season is highlighted in orange, and the 2009-2010 season in blue. (a): The integration domain is the overall region north of 30 °N, and south of the Gulf Stream, bounded by 75 °W and 45 °W. (b): Averaging is over the western portion of the domain, bounded to the east by 60 °W. (c): Averaging is over the eastern portion of the domain, bounded to the west by 60 °W. These "east" and "west" regions are circumscribed by dashed lines in Fig. 2.5.

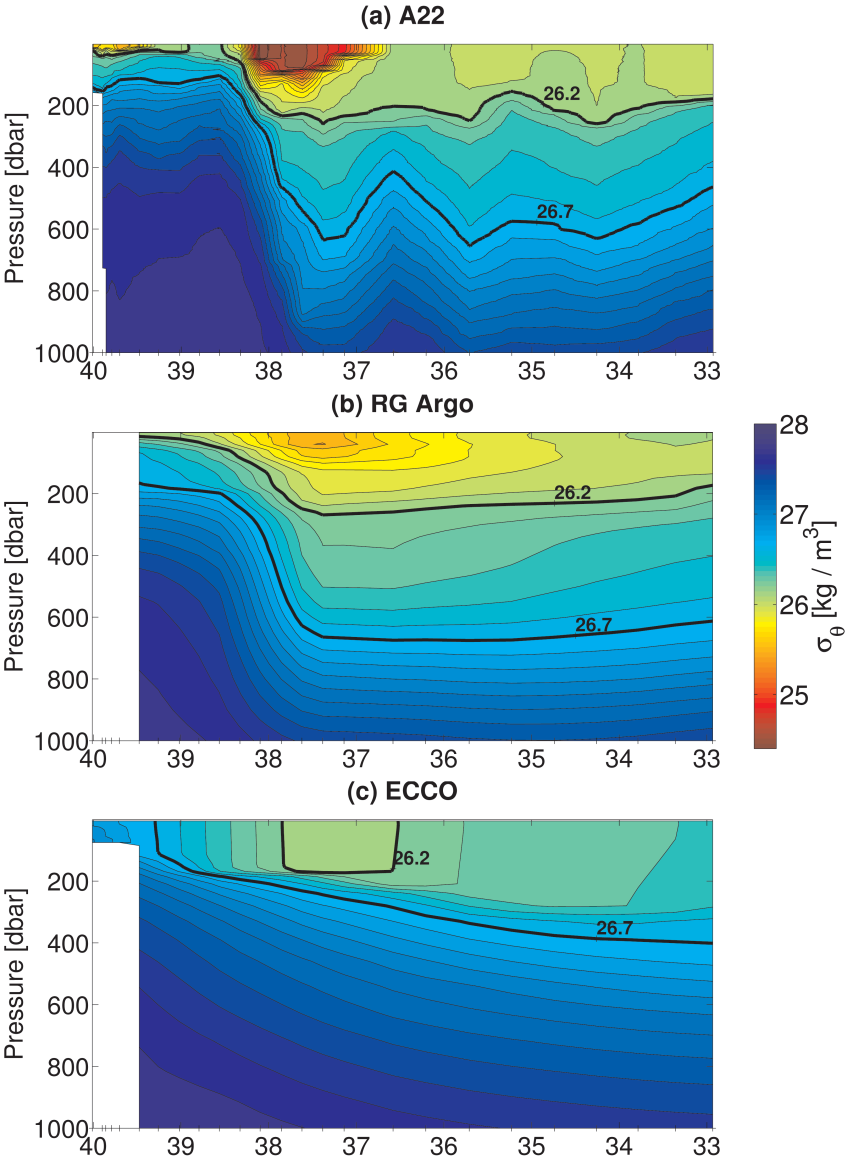

Figure 2.8: Potential density section comparison for A22, RG Argo, and ECCO. (a): Potential density section from the March 2012 occupation of A22. (b): Potential density from March 2012 RG gridded Argo, interpolated onto the A22 track. (c): Potential density from March 2012 ECCO output, interpolated onto the A22 track.

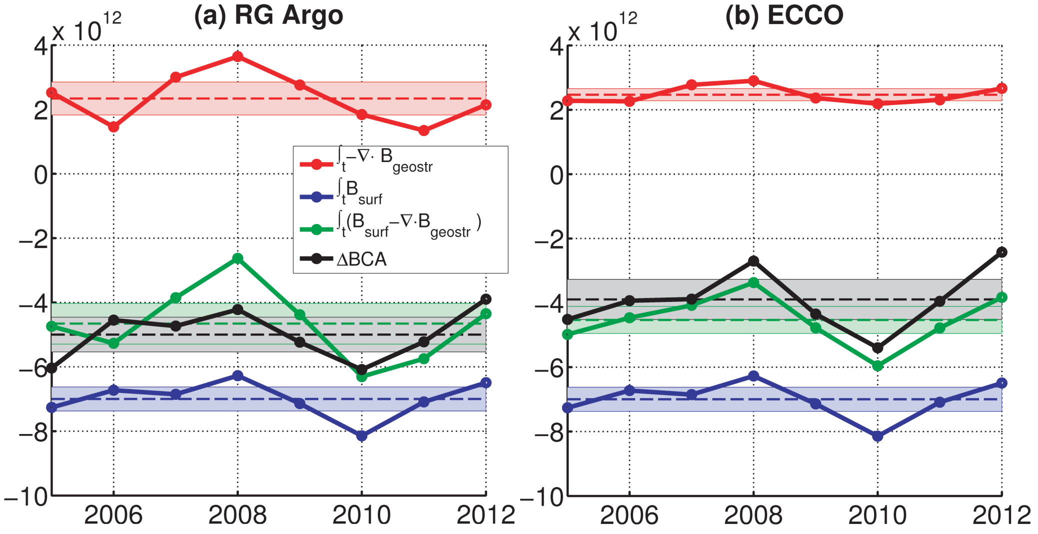

Figure 2.9: Buoyancy budget. Annual winter change, April minus the previous September, in area-integrated BCA ($\Delta\mathcal{BCA}$, black) and the sum of September to April cumulative surface and geostrophic buoyancy fluxes ($\int_t \mathcal{B}_{surf} + \int_t -\nabla \cdot \mathcal{B}_{geostr}$, green) for 2005-2012 (Eq. (2.9)). Cumulative surface and geostrophic buoyancy fluxes are also shown separately (blue and red, respectively). Units are m^4/s^2. Dashed lines represent the record mean with shaded regions spanning the 95% confidence interval for the mean, derived from bootstrap methods. (a): $\Delta\mathcal{BCA}$ and $\int_t -\nabla \cdot \mathcal{B}_{geostr}$ are calculated from RG gridded Argo, with velocities referenced to the surface using AVISO altimetry. (b): $\Delta\mathcal{BCA}$ and $\int_t -\nabla \cdot \mathcal{B}_{geostr}$ are calculated from ECCO output fields.

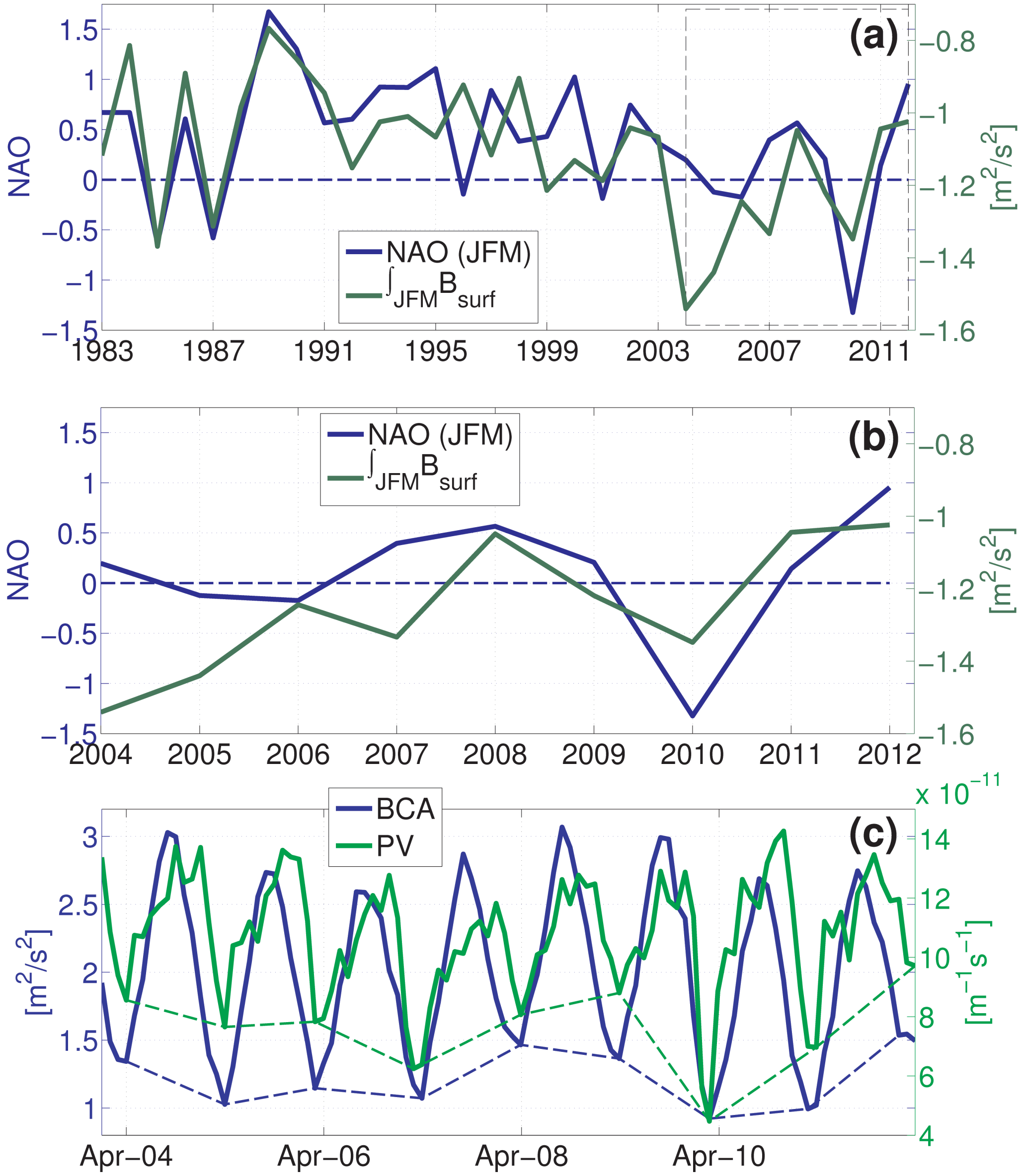

Figure 2.10: NAO and buoyancy flux correlation. (a): January-February-March (JFM) NAO (blue) and JFM cumulative, area-averaged NCEP air-sea buoyancy flux (green). NAO Index Data is provided by the Climate Analysis Section, NCAR, Boulder, USA, *Hurrell et al.* [2003], based on the primary component of EOF analysis on sea level pressure anomalies. (b): Same as in (a), except limited to the period from 2004 to 2012. (c): Area-averaged BCA and area-averaged Potential vorticity at the EDW core, represented by $\sigma_\theta = 26.5$, using RG gridded Argo. Dashed lines demarcate the winter minima. Averages for (a)-(c) are all performed over the region south of the Gulf Stream and north of 30 °N, bounded by 75 °W and 45 °W.

Chapter 3

Annual Cycle and Destruction of Eighteen Degree Water

3.1 Abstract

Eighteen Degree Water (EDW), the subtropical mode water of the western North Atlantic, is a voluminous, weakly-stratified upper ocean water mass that acts as a subsurface reservoir of heat, nutrients, and CO_2. This thick layer persists throughout the year, but nearly half of its volume is dispersed or mixed away, diffusing its properties into the thermocline, from the time it outcrops in winter until it is renewed the following year. CTD observations from Argo profiling floats and acoustically-tracked, isothermally-bound profiling floats are used to quantify EDW destruction rates and investigate the relevant processes responsible for the large annual cycle of EDW. EDW destruction occurs primarily at the top of the EDW layer, with the highest EDW destruction rates occurring during early summer. Slower, steadier EDW destruction is observed in early winter. EDW destruction is dominated by 1-D vertical diffusion, while mesoscale, along-isopycnal stirring is also significant, explaining

approximately 1/3 of the total annual EDW destruction. Destruction via along-isopycnal processes is more prevalent near the Gulf Stream than in the southern Sargasso Sea, due to higher potential vorticity gradients and enhanced mesoscale activity.

3.2 Introduction

Eighteen Degree Water (EDW) is the name given to the subtropical mode water that is associated with the Gulf Stream Extension in the western North Atlantic [*Worthington*, 1959]. The voluminous upper ocean water mass is an important pathway by which anomalous atmospheric heat and CO_2 are injected into the ocean mixed layer and subsequently subducted into the thermocline and deep ocean [*Dong et al.*, 2007; *Bates*, 2012]. The circulation and annual cycle of EDW also influence the pathways by which nutrients are dispersed about the oligotrophic subtropical gyre and supplied to the euphotic zone [*Palter et al.*, 2005].

While EDW persists interannually, the water mass has a large seasonal cycle in which it loses nearly half its volume between late winter/early spring and late fall/early winter [*Kwon and Riser*, 2004]. Despite the large volumetric fluctuation and importance for subduction of tracers into the deep ocean, the mechanisms responsible for EDW dispersal each year are at present poorly understood.

EDW is often defined by a temperature range of 17-19 °C or by an associated density range, but its nearly uniform temperature and salinity (and therefore weak stratification) warrants the inclusion of a Potential Vorticity (PV) threshold that the water mass shall not exceed. Here PV is defined following *Talley and Raymer* [1982], neglecting relative vorticity at large scales:

$$Q = -\frac{f}{\rho}\frac{\partial \rho}{\partial z}, \tag{3.1}$$

where f is the Coriolis parameter and ρ is in situ density. In accordance with *Kwon and Riser* [2004] and *Kwon and Riser* [2005], who employ the above temperature range with a vertical temperature gradient threshold of 0.006°C/m, we impose a potential density range of $\sigma_{EDW} = 26.2 - 26.7$ kg/m^3 and include a corresponding PV threshold of $Q_0 = 10^{-10}$ m^{-1}s^{-1}. Imposing this PV threshold eliminates approximately half the volume of the density class in the western North Atlantic subtropical gyre.

Considering our two defining criteria for EDW, "EDW destruction" refers to either an increase in PV above Q_0 within the σ_{EDW} density class or a modification of density beyond σ_{EDW} within the low PV layer $Q < Q_0$. Here we take the former description to be the most appropriate, where EDW is destroyed via restratification within the density class. This is because we have chosen σ_{EDW} liberally such that, in almost all observations, the weakly stratified $Q < Q_0$ layer generally associated with any mode water is contained completely within the EDW density class. This is illustrated by example of an individual profiling float in the EDW region in Fig. 1c. Looking at all available profiling float data in Fig. 2c,d, note that the potential densities at the top and bottom of the EDW layer are primarily within the interior σ_{EDW}, not on the boundaries, indicating that the EDW boundaries are controlled primarily by stratification and the location of Q_0.

In the present study, we aim to identify the dominant mechanisms driving the destruction of EDW by characterizing the restratification of the water mass in the context of the EDW PV budget. Within this context, two separate processes potentially drive EDW destruction by increasing EDW PV: (1) Diapycnal mixing at the EDW top and bottom boundaries would introduce high PV from above or below the EDW layer. This process would also alter the EDW density class. Associated mechanisms are large vertical shear near the Gulf Stream Extension and near-inertial wave breaking at any location in the subtropical gyre. (2) Lateral stirring of PV along isopycnals across large-scale lateral PV gradients would increase EDW PV. This process would not modify the EDW density class. Associated mechanisms are baroclinic instability and enhanced mesoscale activity near the Gulf Stream.

In what follows, we focus on the subducted EDW layer after it is isolated from the surface by a seasonal pycnocline. The seasonal pycnocline, which can be seen in Fig. 1c as the high PV layer in the upper 200 m of the water column and which is formed principally through seasonal air-sea fluxes, imparts an upper boundary condition for EDW destruction process (1). Discussion of the transition from actively outcropping EDW to subducted EDW via the development of the seasonal pycnocline is left to other studies.

In previous studies, vertical mixing plays a subdominant role in the modification of the EDW temperature class. Assuming a constant vertical diffusivity of $\kappa = 10^{-5}$ m^2/s, *Forget et al.* [2011] find that vertical mixing alone is not enough to describe the total observed EDW annual volume fluctuation, consuming only 1/3 of the peak EDW annual volume, where EDW is defined solely as the 17°C-19°C temperature class. The remaining 2/3 of the volume reduction is attributed to air-sea fluxes at the outcrop of the EDW temperature class, which persists throughout the year while migrating northward into North Atlantic, well beyond the subducted EDW region in the western subtropical basin. The possibility of seasonally elevated vertical diffusivity was not considered. Other studies have shown that vertical diffusivity has a significant seasonal cycle in the subtropical gyre regions, where upper ocean turbulence is elevated during winter [*Whalen et al.*, 2012, 2015].

Large scale lateral stirring of PV is important for North Pacific Subtropical Mode Water (NPSTMW) variability, where NPSTMW volume is strongly associated with the energetic state of the Kuroshio Extension [*Qiu et al.*, 2006]. During its highly energetic state, the Kuroshio Extension is elongated and eddy kinetic energy (EKE) is enhanced, driving lateral fluxes of high PV water southward into the NPSTMW region. This is shown to be the dominant mechanism driving subtropical mode water formation in the region.

For EDW near the Gulf Stream Extension, *Kelly and Dong* [2013] find that the path length of the Gulf Stream is a robust proxy for interannual variations in EDW destruction in that region. While the path length variability of the Gulf Stream has less pronounced states than that of the Kuroshio Extension, it is clear that enhanced EKE in that region is important for driving EDW destruction via lateral mixing across a large PV gradient.

Here we analyze profiling float data to assess the spatial and seasonal variability of EDW destruction and to determine the relative contributions from vertical vs. lateral processes. We show that seasonally elevated vertical mixing, mostly at the top of the EDW layer, is the most important factor influencing EDW destruction.

3.3 Data and Methods

3.3.1 EDW Intensity

In order to quantify both the thickness and low PV signature of the EDW layer in a single quantity, we define EDW Intensity, I, as the vertically integrated PV anomaly (following *Qiu et al.* [2006]):

$$I = \int_{z_2}^{z_1} (Q_0 - Q)\, dz \tag{3.2}$$

where z_2 is the depth of the bottom of the EDW layer, z_1 is the depth of the top of the EDW layer, and where $Q_0 = 10^{-10}$ m^{-1}s^{-1} is the EDW definition PV threshold. Notice that a profile featuring a thick, low PV EDW layer is quantified by a high value for Intensity.

3.3.2 Lagrangian Float Observations

EDW Intensities and estimated vertical diffusivities were calculated using all available Conductivity Temperature Depth (CTD) profiles from the array of profiling floats in the Argo program, from January 2005 to March 2015, with quality control flag “good”. In addition to Argo profiles, CTD data were utilized from nine profiling floats that were deployed during the CLIVAR Mode Water Dynamics Experiment (CLIMODE) observational campaign [*Marshall et al.*, 2009]. Unlike Argo floats, which typically park at 1000 m and profile every 10 days, the CLIMODE profiling floats parked in the EDW layer at 500 m, alternating between 500 m and 1800 m profiles every 5 days. Collectively, the total number of profiles was 9,451 from 169 floats in the EDW region during this period. The lateral extent of the profiles used to calculate Intensity was determined by imposing a dynamic topography minimum threshold of 0.4 m (SSALTO/DUACS 1/3° maps of absolute dynamic topography). This threshold was chosen to eliminate spurious EDW profiles that satisfy the EDW criteria, such as autumn mixed layers north of the Gulf Stream Extension, while still retaining all profiles satisfying EDW criteria that reside in the EDW region.

Isopycnal diffusivity associated with EDW layer circulation was estimated using velocity data from 40 acoustically tracked bobbers deployed as part of the CLIMODE observational campaign. The bobbers were profiling floats that were isothermally bound to the 18.5°C isotherm. They were acoustically tracked with RAFOS, giving daily velocity estimates over the course of approximately two years. They profiled EDW temperature, “bobbing” between $17-20^{\circ}$C every three days, and executed a deep (0-1000 m) temperature profile monthly. Details on bobber data and performance can be found in *Fratantoni et al.* [2013]. We describe the isothermal pathways of the bobbers as “isopycnal” because, within the EDW thermostad in which they resided, there are no large variations in temperature along isopycnals. While these small variations exist and are relevant to discussions of EDW formation [*Joyce et al.*, 2013], *Fratantoni et al.* [2013] illustrate that this approximation is reasonable based on hydrographic observations of the temperature-salinity-density relation in the region.

3.3.3 EDW Destruction Rate

At the end of the EDW outcropping season, the EDW layer restratifies and Intensity decreases. We quantify the "EDW destruction rate" as the temporal derivative of EDW Intensity, dI/dt. Taking the temporal derivative of Equation 3.2 gives

$$\begin{aligned} \frac{dI}{dt} &= \int_{z_2}^{z_1} -\frac{\partial Q}{\partial t}\, dz + \left[(Q_0 - Q)\frac{dz}{dt} \right]_{z_2}^{z_1} \\ &= \int_{z_2}^{z_1} -\frac{\partial Q}{\partial t}\, dz, \end{aligned} \tag{3.3}$$

where we have applied the Leibniz integral rule (since z_1 and z_2 are both time dependent), following *Qiu et al.* [2006]. The second right hand side term vanishes because $Q(z_1) = Q(z_2) = Q_0$. During the restratification season EDW is isolated from the atmosphere, and the evolution of EDW PV is given by the advection-diffusion equation:

$$\frac{\partial Q}{\partial t} + \mathbf{u} \cdot \nabla Q = \frac{\partial}{\partial z}\left(\kappa_z \frac{\partial Q}{\partial z} \right) + \nabla_H \cdot (\mathbf{K_H} \cdot \nabla_H Q) \tag{3.4}$$

where $\mathbf{u}$ is the velocity vector, κ_z is vertical diffusivity, ∇_H indicates the horizontal gradient, and $\mathbf{K_H}$ is a lateral diffusivity tensor with diagonal components κ_x and κ_y. In what follows, we examine each term on the right hand side of Equation 3.4 separately, assuming that the EDW destruction rate is driven entirely by either vertical or lateral mixing. Assuming only vertical mixing in Section 3.3.4, we obtain an estimate for EDW κ_z, which we inspect seasonally, and which is an upper limit as lateral processes are not included. While we calculate our estimate of κ_z in vertical coordinates, the interpretation is approximately equivalent to diapycnal diffusivity outside of the Gulf Stream, the northern boundary of the EDW region. In Section 3.3.5, assuming only lateral mixing, we determine the proportion of EDW destruction that could be driven by lateral processes and examine the result both seasonally and regionally. We simplify $\mathbf{K_H}$, describing lateral diffusivity as an isotropic scalar, κ_H. Given the Lagrangian nature of the isotherm-following observations used to compute κ_H, we interpret the result as isothermal, hence isopycnal, diffusivity and calculate horizontal gradients along isopycnals.

3.3.4 Vertical Mixing

Following *Qiu et al.* [2006], we use rate of change of EDW Intensity to estimate time series of vertical eddy diffusivity at the top of the EDW layer. Since we are interested in EDW destruction, we focus only on subducted EDW, ignoring the formation period when the layer is actively outcropping. For simplicity, assume that the evolution of PV is given by vertical diffusion only, so that Equation 3.4 reduces to the following:

$$\frac{\partial Q}{\partial t} = \frac{\partial}{\partial z}\left(\kappa_z \frac{\partial Q}{\partial z}\right) \tag{3.5}$$

Qiu et al. [2006] average together several profiles in the center of the recirculation gyre, calculating Intensity rate of change in an Eulerian fashion, and ignore advection based on the assumption that advection is negligible there. In this study, Equation 3.5 presumes negligible advection because temporal derivatives are calculated in a quasi-Lagrangian fashion, following individual float trajectories. Additionally, we anticipate that the advection term of Equation 3.4 is small on time scales of a few months, given the weak spatial gradients of Intensity within the EDW layer.

Argo floats, with a parking depth of 1000 m, are imperfect Lagrangian indicators of EDW pathways, so we employ criteria to restrict float records to suitably Lagrangian trajectories. After critically examining many EDW trajectories, we impose the criteria that subducted EDW Intensity must be decreasing over a time scale of one month and the EDW bottom isopycnal, $\sigma_\theta = 26.7$, must not exceed a 150 m displacement over the time scale of one month. These criteria are chosen subjectively, but limit the assimilation of float trajectories in which the float has been transported to a new regime, producing a misleading EDW destruction rate. While subducted EDW Intensity may increase via cross-frontal mixing near the Gulf Stream [*Joyce et al.*, 2013], possible cases are omitted from this analysis. It should also be noted that while all trajectories with increasing Intensity are omitted, some trajectories with spuriously decreasing Intensity, due to the effects of advection, are retained. While much of the random advection of Intensity is averaged out statistically, the inclusion of these trajectories may introduce a larger scatter in EDW destruction rate magnitudes and a potential inflation of the mean.

Substituting Equation 3.5 into Equation 3.3,

$$\frac{dI}{dt} = -\kappa_z(z_1)\frac{\partial Q}{\partial z}(z_1) + \kappa_z(z_2)\frac{\partial Q}{\partial z}(z_2) \tag{3.6}$$

Equation 3.6 states that, assuming vertical diffusion of PV only, the EDW destruction rate is given by the divergence of the vertical diffusive PV flux in the layer.

Several studies have assessed the EDW seasonal cycle within the framework of the PV budget and flux form of the PV equation [*Czaja and Hausmann*, 2009; *Maze and*

Marshall, 2011; *Deremble and Dewar*, 2013]. Within this framework, one can usefully employ the "impermeability theorem", which states that integral PV fluxes do not cross surfaces of potential density [*Haynes and McIntyre*, 1987]. *Deremble and Dewar* [2013] invoke the impermeability theorem to demonstrate that EDW PV is balanced by surface PV flux at the EDW outcrop and lateral eddy fluxes at the EDW boundaries, which import high PV fluid from outside the EDW region that erodes the EDW layer seasonally. It is important to note that in the methods described here above, there is no violation of the impermeability theorem because z_1 is not a potential density surface, but rather a surface of constant PV where $Q = Q_0$. Therefore EDW Intensity, I, may freely fluctuate throughout the subducted EDW season while the total integrated PV between any two isopycnal surfaces remains fixed.

The bottom of the EDW layer, z_2, lies just above the permanent pycnocline. Observations from Argo float profiles show that the vertical PV gradient at z_2 is several orders of magnitude smaller than the vertical PV gradient at the top of the EDW layer, z_1. Additionally, measurements of diapycnal diffusivity in the permanent pycnocline of the North Atlantic subtropical gyre are small, at O(10^{-5} m^{2}s^{-1}) [*Ledwell et al.*, 1993], and estimates just above the permanent pycnocline decrease with depth, from the 250m-500m depth interval to the 500m-1000m range [*Whalen et al.*, 2012]. Therefore, the second term on the right had side of Equation 3.6 is small, and we can approximate vertical eddy diffusivity κ_z at the top of the EDW layer as

$$\kappa_z(z_1) = \frac{dI/dt}{\partial Q/\partial z(z_1)} \tag{3.7}$$

dI/dt is calculated as the slope of a linear fit to each piece of the float record that satisfies the trajectory criteria described above. The vertical PV gradient at the top of the EDW layer is calculated as the finite difference between PV at the top of the EDW layer, Q_0, and PV at the PV maximum in the seasonal pycnocline, smoothed in time with a two month half-width gaussian filter. Since the evolution of the PV gradient determines the shape of the evolution of diapycnal diffusivity for individual float trajectories, we opt to smooth the PV gradient in time rather than subjectively choose a functional form to fit to the data. Estimates of mean seasonal vertical diffusivity are robust to variations in smoothing time scale between one and three month half-width filters.

Estimates for $\kappa_z(z_1)$ were verified by stepping forward Equation 3.6 and applying the time dependent $\kappa_z(z_1)$ estimated from Equation 3.7:

$$I(t_{i+1}) = I(t_i) - \int_{t_i}^{t_{i+1}} \kappa_z(z_1)\frac{\partial Q}{\partial z}(z_1)\,dz \tag{3.8}$$

On an individual float basis, the result of Equation 3.8 agrees well with the Intensity observed along float trajectories, thereby providing confidence in our methods for calculating $\kappa_z(z_1)$.

3.3.5 Isopycnal Mixing

Single-particle isopycnal diffusivity was calculated from the CLIMODE bobber trajectories using the methodology of *Davis* [1982] and following the specific approach of *Lumpkin et al.* [2002]:

$$\kappa_H = T_L\langle|u|'^2\rangle \tag{3.9}$$

where T_L is the Lagrangian time scale and $\langle|u|'^2\rangle$ is an ensemble averaged form of EKE. The above parameterization was used to produce both a $2^\circ \times 2^\circ$ map of bobber-period isopycnal diffusivity as well as seasonally varying isopycnal diffusivity, estimated on average across the entire EDW region.

To compute the integral Lagrangian time scale, T_L, the velocity autocorrelation was calculated for 75 non-overlapping, 90-day segments of Lagrangian bobber data, ensemble averaged, and integrated to the first zero crossing. No significant differences in T_L resulted from using zonal vs. meridional components of velocity. $|u|'$ was taken as the RMS velocity magnitude averaged over the 75 90-day bobber trajectory segments. For simplicity, we take κ_H in its scalar form since there were no significant differences in magnitude and regional variability between κ_x and κ_y, computed by evaluating $|u|'$ using zonal and meridional velocities separately. Further details, including sensitivity studies and comparisons with previous estimates, can be found in *Fratantoni et al.* [2013].

Using the map of isopycnal diffusivity calculated from bobber velocity data along with vertical structure from Argo profiles, we can estimate the proportion of isopycnal mixing responsible for the total EDW destruction rate. We calculate this "isopycnal destruction rate" as follows. Beginning with the time rate of change of EDW Intensity (Equation 3.3), we substitute Equation 3.4 assuming isopycnal mixing only and removing advection following bobber trajectories:

$$\frac{\partial Q}{\partial t} = \nabla_H \cdot (\kappa_H \nabla_H Q) \tag{3.10}$$

The result is

$$\frac{dI}{dt} = -\nabla_H \cdot \left(\kappa_H \overline{\nabla_H Q}\right), \tag{3.11}$$

where the overbar denotes vertical integration from z_2 to z_1, and where we have employed the Leibniz integration rule (since z_1 and z_2 vary with lateral coordinates), finding that all additional terms are identically zero as a result of $\nabla_H Q(z_1) = \nabla_H Q(z_2) = 0$ since Q is constant and equal to Q_0 at z_1 and z_2. Furthermore, we have taken κ_H to be depth independent within the EDW layer (between z_1 and z_2) since the bobbers resided almost exclusively within and throughout the EDW layer. Then, integrating over an arbitrary control volume, A, we apply the divergence theorem to obtain

$$\int_A \frac{dI}{dt} = -\oint_{\partial A} \kappa_H \overline{\frac{\partial Q}{\partial n}} + \text{other terms}, \tag{3.12}$$

where the right hand side contour integral is around the boundary of A, ∂A, and $\partial Q/\partial n$ is the lateral PV gradient normal to ∂A. The left hand side is the "total destruction rate", while the right hand side integral is the "isopycnal destruction rate", or the isopycnal mixing that contributes to the total destruction rate.

We calculate the left hand side of Equation 3.12 using the Roemmich-Gilson (RG) gridded Argo climatology [*Roemmich and Gilson*, 2009]. The product is objectively mapped from quality controlled Argo temperature and salinity profiles on a uniform, $1^\circ \times 1^\circ$ grid with 58 depth levels down to 2,000 m depth and monthly temporal resolution. The temporal derivative of EDW intensity is therefore set to a minimum timescale of one month. We can also employ RG Argo to calculate $\partial Q/\partial n$, where the lateral length scale is set by the maximum resolution of the RG grid. Finally, we apply our mapped isopycnal diffusivity inferred from the CLIMODE bobber velocity data set for κ_H on the right hand side, and the isopycnal destruction rate can be calculated, interpreted as a proportion of the total destruction rate.

3.4 EDW Destruction: Spatial and Seasonal Variability

3.4.1 Seasonal Evolution of Low PV EDW Layer

Following an individual profiling float with a 500 m parking depth (CLIMODE) gives a quasi-Lagrangian view of the seasonal cycle of EDW (Figure 3.1). Beginning in late winter (February/March; FM), the EDW layer outcrops and low PV is injected into the layer primarily via buoyancy forcing [*Maze and Marshall*, 2011; *Deremble and Dewar*, 2013]. At the onset of surface warming in early summer, the EDW layer is capped over by a high PV seasonal pycnocline. The EDW low PV signature decays throughout the remainder of the year as the layer restratifies and thins, and while the seasonal pycnocline weakens and deepens. The layer may or may not outcrop the following winter. This float in particular experienced its first winter (FM 2006) in the northeastern part of the EDW region, where it observed thorough EDW ventilation and deep mixed layers exceeding 400 m (Figure 3.1 a,c). It experienced its second winter (FM 2007) in the southern part of the EDW region near Bermuda, where the seasonal pycnocline remained intact in that region and the EDW layer remained isolated from the atmosphere.

Across all available Argo float profiles on average, the top of the EDW layer deepens throughout the EDW restratification season, while the depth of the bottom of the layer remains relatively constant (Figure 3.2 a,b). This indicates that EDW destruction occurs primarily at the top of the layer. Furthermore, the envelope of all observations of the depth of the top of the EDW layer narrows from the top during the restratification season, indicating the uniformity of this process across all locations of the EDW region. Also note that EDW outcropping occurs primarily in the northern part of the subtropical gyre near the Gulf Stream, whereas in the southern part of the gyre EDW tends to remain subducted (Figure 3.2a).

Additionally, the low PV EDW signature tends to erode faster in the shallowest portion of the EDW density class than the deepest portion of the density class. This can be seen by noting that the depth of the EDW top, which is controlled by the depth of the PV threshold Q_0, recedes into deeper lying isopycnals over the course of the restratification season, while the mean EDW bottom remains relatively fixed on the $\sigma_\theta = 26.57$ isopycnal (Figure 3.2 c,d).

3.4.2 EDW Intensity and Destruction Rate

Thick, low PV EDW layers are quantified by high values of EDW Intensity. The largest EDW Intensities occur during February/March/April (FMA) outcropping, particularly in the northern region of the Sargasso Sea that encompasses the EDW outcropping zone (Figure 3.3a,b). In the southern latitudes of the gyre, where EDW is generally isolated from the surface year-round, mean EDW Intensity remains relatively constant, with only a slight decrease throughout the restratification season (Figure 3.3a). During the restratification season (June-December), EDW Intensity is more uniformly distributed throughout the EDW region than in late winter (Figure 3.3c). There is an especially large fluctuation between FMA and June-December Intensities in the northern latitudes of the Sargasso Sea, with extraordinarily low intensity near the Gulf Stream during the June-December restratification period. We hypothesize that this low Intensity EDW is associated with cross-frontal exchange with high PV water north of the Gulf Stream Extension.

As EDW Intensity decreases throughout the region during the restratification season, we define the “EDW destruction rate” as the time rate of change of Intensity, dI/dt. Figure 3.4a shows EDW destruction rates calculated along trajectories of individual Argo floats, ensemble averaged into latitude bands (dashed). In the southern latitudes of the Sargasso Sea, the EDW destruction rate is relatively constant, indicating a seasonally steady mechanism for EDW destruction.

In the northern latitudes of the subtropical gyre, EDW destruction mechanisms are associated with those that restratify and strengthen the seasonal pycnocline. In this region, the EDW destruction rate exhibits a rapid phase from May to September and a steadily decreasing phase from October into early winter. The rapid phase of the EDW destruction rate coincides with a strengthening seasonal pycnocline, indicated by an increasing vertical PV gradient at the top of the EDW layer from May to mid-August (Figure 3.4b).

3.5 EDW Diffusivity

3.5.1 Vertical Diffusivity at EDW Layer Top

We estimate vertical diffusivity at the top of the subducted EDW layer following the methods of *Qiu et al.* [2006], reviewed in Section 3.3.4. These estimates range from O(10^{-5} m^2s^{-1}) to O(10^{-4} m^2s^{-1}) following individual Argo float trajectories (Figure 3.5a). In the ensemble mean, elevated vertical diffusivity of O(10^{-4} m^2s^{-1}) appears during winter. This period of elevated vertical diffusivity is associated with a weak PV gradient at the top of the EDW layer and weak seasonal pycnocline (Figure 3.4b). Ensemble average vertical diffusivity is lowest in late summer/early autumn, where estimates are O(10^{-5} m^2s^{-1}). Note that these vertical diffusivity magnitudes are upper bound estimates because they are formulated by assuming that vertical mixing is responsible for all of the EDW destruction. Furthermore, in the northern Sargasso Sea, larger lateral PV gradients may cause larger rates of change of Intensity along float trajectories. This is a potential source of error that would also inflate estimates of diapycnal diffusivity.

The magnitude and seasonal cycle of vertical diffusivity found in Figure 3.5a is consistent with other studies. Here, we have estimated a seasonal cycle of vertical diffusivity by observing the evolution of PV and inferring the vertical diffusivity required to produce that evolution. *Whalen et al.* [2012, 2015] take a more direct approach, using a finescale parameterization method for estimating turbulent kinetic energy dissipation and vertical diffusivity from Argo profiles. Just below the subtropical mode water layer in the EDW region, within a depth range of 250-500 m, *Whalen et al.* [2015] find diffusivities with consistent orders of magnitude, ranging from O(10^{-5} m^{2}s^{-1}) to O(10^{-4} m^{2}s^{-1}). Just below the subtropical mode water of the Northwest Pacific, within a depth range of 350-450 m, *Whalen et al.* [2012] find a seasonal cycle of turbulent dissipation that is similar the seasonal cycle of vertical diffusivity in Figure 3.5a, peaking in late winter with a minimum in late summer. These finescale strain parameterizations depend on several assumptions regarding turbulence and frequency content within the internal wave field and break down in the surface mixed layer and weakly stratified mode water layers, which have been carefully omitted from the estimations of *Whalen et al.* [2012]. The advantage of the method we present here is that it does not rely on an assumption about the underlying process for vertical diffusive mixing, and we obtain an estimate of vertical eddy diffusivity directly within the mode water layer (when it is not actively outcropping).

Direct microstructure observations in the EDW region are also consistent with our results. As part of the LatMix observational campaign [*Shcherbina et al.*, 2015], three E-M profiling floats equipped with microstructure thermistors were deployed in both quiescent and moderate mesoscale straining regions of the western subtropical gyre in June. At $\sigma_\theta = 26.2$ kg/m^3, the top of the σ_{EDW} density layer, floats reported summer diapycnal diffusivities of O(10^{-5} m^{2}s^{-1}), comparable to those shown in June in Figure 3.5a.

In this first step of our analysis we assumed that vertical mixing is the only process responsible for the evolution of EDW PV, yet obtained reasonable magnitudes for vertical diffusivity. This indicates that vertical mixing is an important process in the destruction of EDW.

3.5.2 Isopycnal Diffusivity

Since EDW may also be destroyed by increasing PV along isopycnals, lateral mixing may also be important. We calculate isopycnal diffusivity, κ_H, using daily velocity data obtained from CLIMODE bobbers (see Section 3.3.5). The result (Figure 3.5b) is a seasonal cycle that is similar to that of vertical diffusivity (Figure 3.5a) which is high in winter and low in summer, with a minimum in October. The Lagrangian time scale is ~ 3.1 days, which corresponds to a 60 km length scale. The seasonality of EDW isopycnal diffusivity is dominated by variability in $\langle |u|'^2 \rangle$ (Figure 3.5c). The Lagrangian time scale does not appear to exhibit strong seasonality.

A map of isopycnal diffusivity was also calculated, using all available bobber data for the duration of the bobber record (Figure 3.6b). Spatial variability of EDW isopycnal diffusivity is very similar to that of EKE, which is elevated near the Gulf Stream (see *Fratantoni et al.* [2013] for EDW EKE map). The spatial variability of our EDW isopycnal diffusivity estimates are consistent with previous studies [*Kwon and Riser*, 2005; *Cole et al.*, 2015], while the magnitudes are larger than those of *Kwon and Riser* [2005], who made the calculation using floats parked at 1000 m depth, deeper than the bobbers which drifted between roughly 100-450 m.

Both lateral and vertical diffusivities exhibit a similar seasonal cycle, peaking in winter. The seasonality of vertical diffusivity coincides with near inertial energy in the mixed layer [*Chaigneau et al.*, 2008], indicating breaking near inertial waves as a likely mechanism. It is important to point out that since our estimate of vertical diffusivity was derived under the assumption that all EDW destruction is vertically diffusive, isopycnal diffusive processes may be present in that seasonal signal. In order to separate the effects of vertical and lateral processes contributing to EDW destruction, we apply our estimated isopycnal diffusivity to its respective PV gradient field in the next section.

3.6 EDW Destruction Mechanisms: Vertical Mixing vs. Lateral Stirring of PV

3.6.1 Isopycnal EDW Destruction Rate

We evaluate the efficiency of isopycnal stirring as the primary component of seasonal EDW PV evolution by calculating an EDW destruction rate using monthly PV fields derived from RG Argo and the map of isopycnal diffusivity derived from CLIMODE bobbers (Sections 3.3.5 and 3.5.2). This "isopycnal destruction rate" is the component of the total EDW destruction rate that is attributed to lateral processes that erode the low PV layer by introducing high PV waters along isopycnals.

As a control volume, we choose a box located in the center of the recirculation gyre (solid green, Figure 3.6a, 3.6b) to limit the influence of advection of PV, which was ignored in the formulation of the isopycnal destruction rate. Advection of PV would appear as noise or bias in our isopycnal destruction estimates. A map of PV on $\sigma_\theta = 26.5$ kg/m^3 is shown for October 2006 (Figure 3.6a) as an arbitrary example of the EDW PV field during the restratification season.

Figure 3.6b compares the total destruction rate, dI/dt, with the isopycnal destruction rate. Periods during which $dI/dt > 0$ are periods of seasonal EDW formation. Since EDW Intensity is both a measure of EDW thickness and EDW stratification, high positive peaks indicate strong EDW formation winters and low positive peaks indicate weak EDW formation winters within this region. This interannual variability is consistent with previous studies, which show strong EDW formation winters in 2004/05 and 2009/10 and weak

EDW formation winters in 2007/08 and 2011/12 [*Billheimer and Talley*, 2013], linked to the phase of the late winter North Atlantic Oscillation (NAO). Winters 2013/14 and 2014/15 were extraordinarily weak years for EDW formation, consistent with strongly positive NAO winters [*Billheimer and Talley*, 2016a].

Focusing on periods when $dI/dt < 0$, we find that the isopycnal stirring of PV that destroys EDW in this region is a weak, steady process relative to the total observed seasonal EDW destruction (Fig. 6b). During time periods of isopycnal and net EDW destruction (shaded Fig. 6b where $dI/dt < 0$ and the right hand side of Equation 3.12 is negative), the isopycnal destruction rate constitutes 36% of the total EDW destruction rate from 2004-2015.

3.6.2 Regional Mechanisms

Repeating our calculation of isopycnal destruction rate, we vary the location of the control volume so that the importance of lateral processes in the GS region may be compared to that of the southern gyre region (dashed boxes Figure 3.6a). We find that isopycnal destruction constitutes 39% of the total EDW destruction rate seasonally in the northern control volume (blue dashed box Figure 3.6a), but only 17% in the southern region (red dashed box Figure 3.6a). The quantification could be biased by the effect of advection, which is neglected, but regardless we see a reduction in the lateral stirring contribution to EDW destruction by about one half in the south. Greater effectiveness of lateral processes in the north is due to both the enhanced lateral diffusivity resulting from higher eddy activity and the adjacent source of high PV in and north of the Gulf Stream.

Additionally, by contrasting observations that vary spatially, we quantify EDW profile vertical structure to determine the prevalence of lateral vs. vertical processes for

EDW destruction regionally. Figure 3.7 suggests that dispersion via lateral processes in the northern part of the gyre near the Gulf Stream is likely more prevalent than in the south, consistent with the finding above. Looking at EDW Intensity vs. EDW thickness, we find that for a given Intensity, EDW layers in the northern part of the Sargasso Sea near the Gulf Stream are thin, whereas EDW layers in the southern part of the gyre are thick. This implies that thin, low mean PV (strong) EDW layers tend to exist in the Gulf Stream region, whereas thick, high mean PV (weak) EDW layers are more prevalent in the southern gyre region.

By vertical diffusion of PV only, a low PV EDW density profile would tend to linearize, increasing its mean PV, while only slightly reducing its thickness. By lateral PV stirring mechanisms (e.g. baroclinic instability, shear dispersion, or submesoscale instabilities), vertical segments of the low PV EDW signature would be stirred away, leaving a significantly thinner, but still strongly low PV EDW layer.

These lateral PV stirring mechanisms are more prevalent in the northern part of the subtropical gyre near the Gulf Stream than in the more quiescent central gyre. *Joyce et al.* [2013] find that during winter, lateral mixing across the Gulf Stream provides a source of EDW. Wind-driven instabilities and large vertical and lateral shear within the Gulf Stream modify wintertime convection, producing negative Ertel PV and enhancing EDW formation. It is possible that instabilities within the Gulf Stream that drive cross-frontal mixing may also occur during the remainder of the year, enhancing lateral PV stirring and EDW destruction in that region.

3.7 Final Remarks

The results shown in this study are summarized as follows: (1) EDW destruction is dominated by 1-D vertical mixing. (2) EDW destruction occurs primarily at the top of the EDW layer. (3) The EDW destruction rate exhibits a rapid phase during early summer, which is associated with the development of the seasonal pycnocline, and as the seasonal pycnocline weakens in autumn the EDW destruction rate steadily declines. (4) EDW vertical and lateral diffusivities exhibit seasonal cycles: They are both high in late winter and low in late summer, consistent with the seasonality of EDW eddy kinetic energy. (5) Mesoscale isopycnal stirring of EDW is a relatively weak and steady process, constituting approximately 36% of the total EDW destruction over the Argo period. (6) Along-isopycnal stirring of PV plays a more important role in EDW destruction in the northern part of the Sargasso Sea near the Gulf Stream Extension, where eddy kinetic energy and isopycnal diffusivity are enhanced and where there are large along-isopycnal PV gradients, compared to the southern part of the EDW region.

The time scales of EDW reemergence in subsequent winters are consistent with our finding of the dominance of 1-D diffusion for EDW destruction. Tracing e-particle tracers in an eddy-resolving simulation, *Kwon et al.* [2015] find that 2/3 of outcropping EDW particles reemerge the following winter, while 80% of those reemerging particles become non-EDW before their first re-outcropping. Particles that re-outcrop within one year remain in the region, while those that outcrop in subsequent years leave the region first, i.e. the re-outcropping time scale is set by how long the particles remain in the region. *Kwon et al.* [2015] also deduce that the eddy field is subdominant to the mean flow in controlling the advection of particles out of the outcropping region and thereby their one-year re-outcropping. These results suggest a dominantly one-dimensional vertical cycle of EDW destruction and reemergence on a year-to-year time scale.

Near-inertial wave breaking is likely the dominant mechanism driving the destruction of subducted EDW. The breaking of downward propagating, near-inertial internal waves excited by high frequency wind fluctuations is a significant source for elevated mixing levels in the upper ocean [*Alford*, 2001]. In the EDW region, the seasonal cycle of mixed layer near-inertial energy [*Chaigneau et al.*, 2008] coincides with the cycle of both vertical and isopycnal diffusivities of Figure 3.5 a,b, with enhanced near-inertial energy occurring in late winter when EDW vertical diffusivity peaks. This is consistent with *Whalen et al.* [2012], who find a seasonal correlation between mixed layer near-inertial energy and turbulent dissipation at subtropical latitudes.

We find a small but significant contribution to EDW destruction from along-isopycnal processes, especially near the Gulf Stream, in which low PV EDW is stirred with outside high PV sources. The time and length scales of our isopycnal destruction calculation (1-2 months, O(100 km)) reflect a contribution to this PV stirring from mesoscale activity. A large PV gradient across the Gulf Stream and enhanced mesoscale activity in the region suggest that the high PV water that destroys EDW is imported slope water originating north the Gulf Stream. This was not thoroughly investigated and is a hypothesis that remains to be tested in models. Furthermore, the submesoscale processes that are left unresolved in this study, such as rapid restratification via mixed layer instabilities [*Boccaletti et al.*, 2007], may be important for restratifying EDW immediately after it outcrops and require further investigation.

3.8 Acknowledgments

The authors thank the reviewers for their helpful comments. Funding was provided by NSF Ocean Sciences OCE-0960928 (CLIMODE). Argo data were collected and made freely available by the International Argo Program and the national programs that contribute to it (http://www.argo.ucsd.edu, http://argo.jcommops.org). The altimeter products were produced by Ssalto/Duacs and distributed by Aviso, with support from Cnes (http://www.aviso.altimetry.fr/duacs/). The Roemmich-Gilson Argo Climatology is available at http://sio-argo.ucsd.edu/RG_Climatology.html.

Chapter 3 is a reprint of the material as it appears in Billheimer, S., and L. D. Talley (2016), Annual cycle and destruction of Eighteen Degree Water, *J. Geophys. Res. Oceans*, doi:10.1002/2016JC011799 (Copyright of the American Geophysical Union 2016). The dissertation author was the primary researcher and first author.

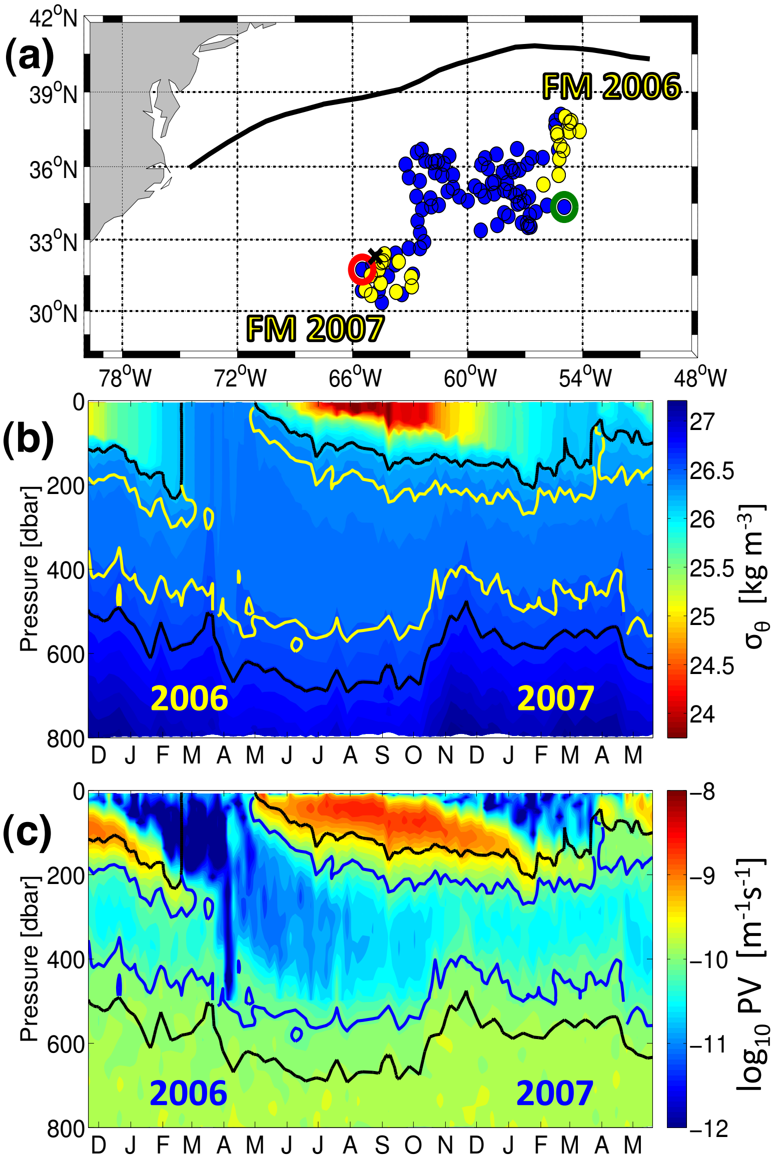

Figure 3.1: CLIMODE float "2723". (a) Trajectory of CLIMODE float "2723". Dots indicate locations of float profiles, while late winter (February/March) profile locations are highlighted in yellow. The green circle marks the location of the float's first profile while the red circle marks the location of the float's last successful report. For reference, the location of Bermuda is marked by a black "x" while the mean location of the Gulf Stream during the floats active mission is delineated by the black curve. The Gulf Stream location is defined by the 15°C temperature contour at 200 m depth [*Fuglister*, 1963] during the float's reporting period, calculated from RG Argo. (b) Potential density from float "2723" (color contour). Black contours are the boundaries of the EDW potential density range $\sigma_{EDW} = 26.2 - 26.7$ kg/m^3. The yellow curve contours the EDW potential vorticity threshold, $Q_0 = 10^{-10}$ m^{-1}s^{-1}. (c) Potential vorticity from float "2723". Black contour is as in panel b, and blue contour is Q_0.

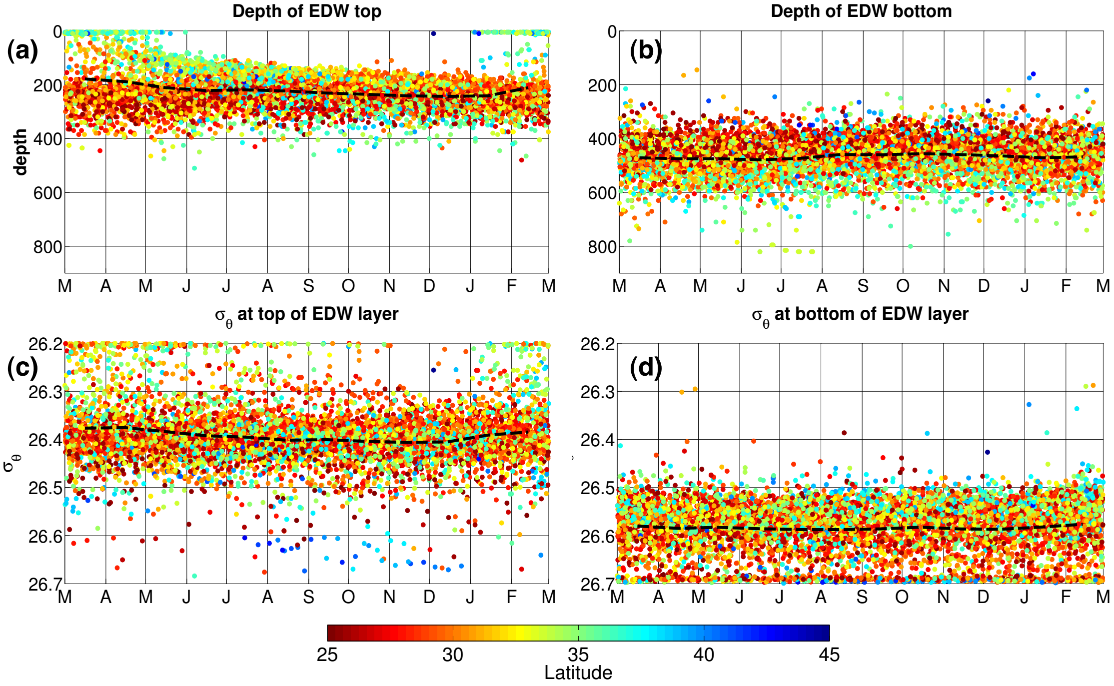

Figure 3.2: (a) Depth of the top and (b) bottom of the EDW layer from all available Argo profiles in the EDW region, 2005-2015. (c) Potential density at the top and (d) bottom of the EDW layer. Color indicates the latitude of the float profile. Black dashed curves are the ensemble average of observations in 30 day bins.

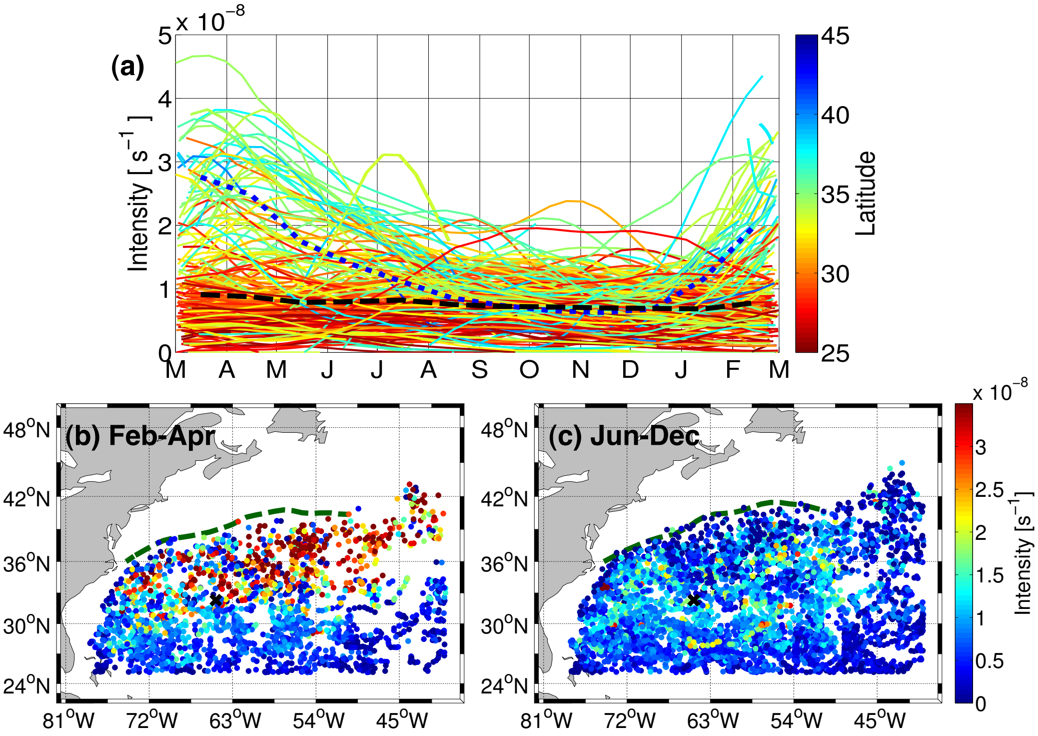

Figure 3.3: EDW Intensity. (a) EDW Intensity, following Argo float trajectories, 2005-2015. Color indicates a profiling float's annual mean latitude. Intensity is smoothed in time with a two month half-width gaussian filter for presentation. Bold curves indicate ensemble average Lagrangian Intensity for latitudes greater than (dotted blue) and less than (dashed black) 34°N. (b) EDW Intensity from all Argo profiles in the EDW region during the EDW outcropping season, February through April, 2005-2015. Dashed green curve delineates the mean Gulf Stream position during this period. (c) EDW Intensity from Argo profiles during the EDW restratification season, June through December, 2005-2015. Dashed green curve is mean Gulf Stream position, June through December, 2005-2015.

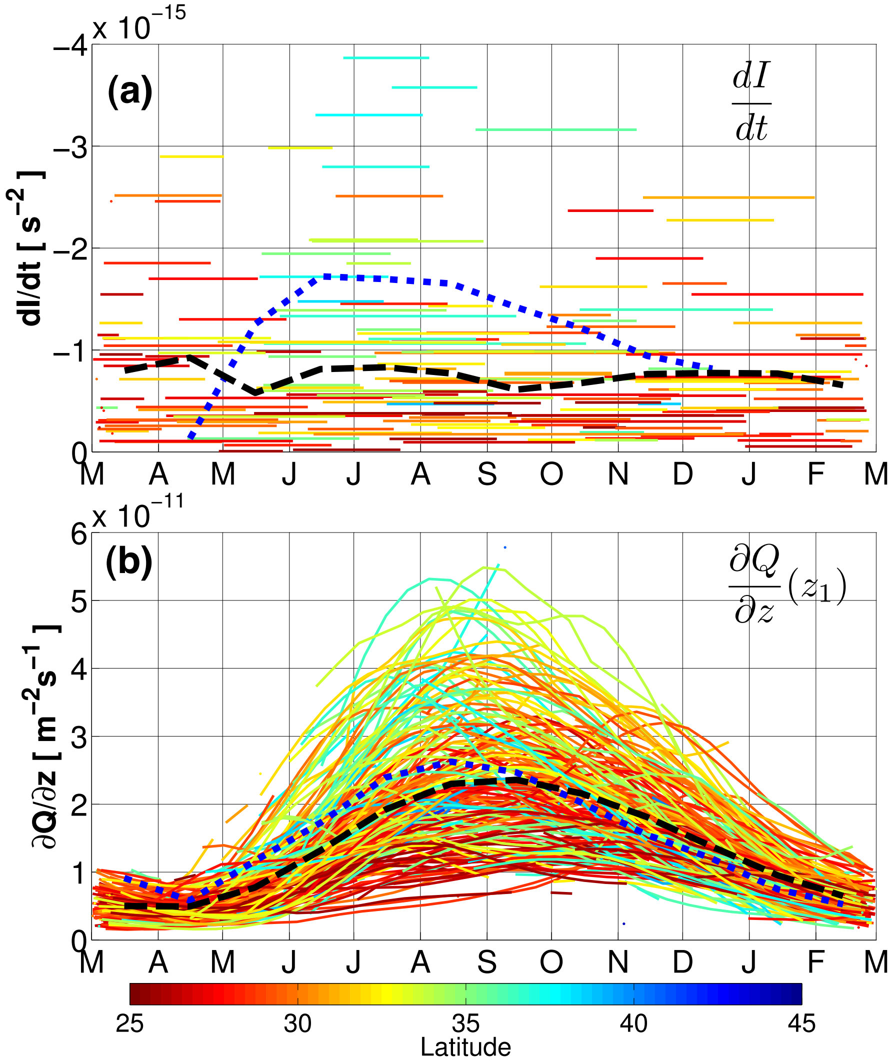

Figure 3.4: EDW destruction rate and potential vorticity gradient. (a) EDW destruction rate, following Argo float trajectories while they are suitably Lagrangian (see section 3.3.4 for description). Color indicates annual mean latitude. Bold curves are ensemble average EDW destruction rates for latitudes greater than (dotted blue) and less than (dashed black) 34°N. Note that $dI/dt < 0$ indicates EDW destruction and that the vertical axis is reversed. (b) Vertical potential vorticity gradient at the top of the EDW layer, following Argo float trajectories, smoothed in time with a two month half-width gaussian filter. Color and dashed curves as in panel a.

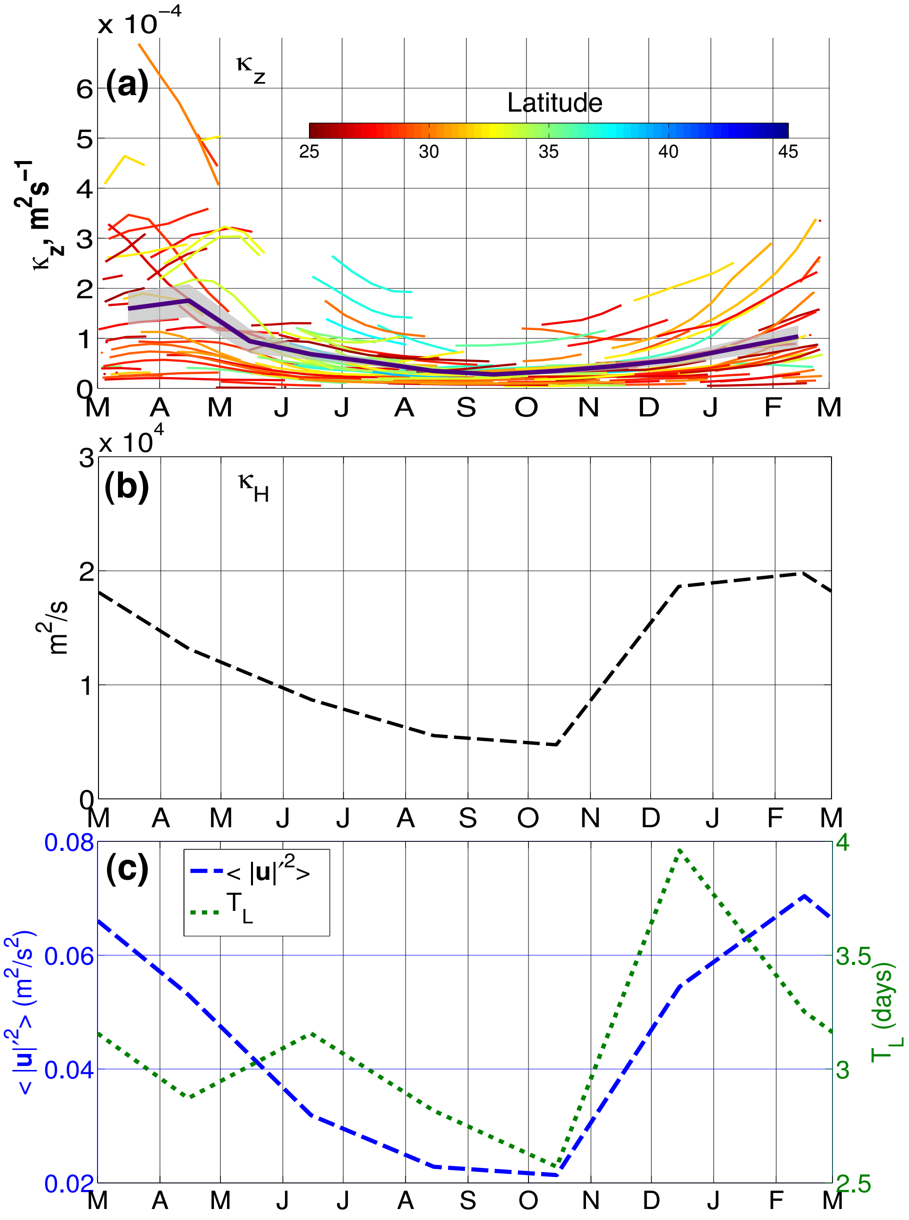

Figure 3.5: EDW vertical and isopycnal diffusivity. (a) Vertical diffusivity at the top of the EDW layer following Argo float trajectories, 2005-2015. Color is as in Figure 4 a,b. The ensemble average is shown (bold indigo) with a 95% confidence interval (gray shading) obtained from bootstrapping methods. (b) Seasonal isopycnal diffusivity calculated from CLIMODE bobber velocity data. (c) Ensemble average eddy kinetic energy, $\langle |u|'^2 \rangle$, and Lagrangian time scale, T_L, from CLIMODE bobbers, used to calculate the isopycnal diffusivity of panel b.

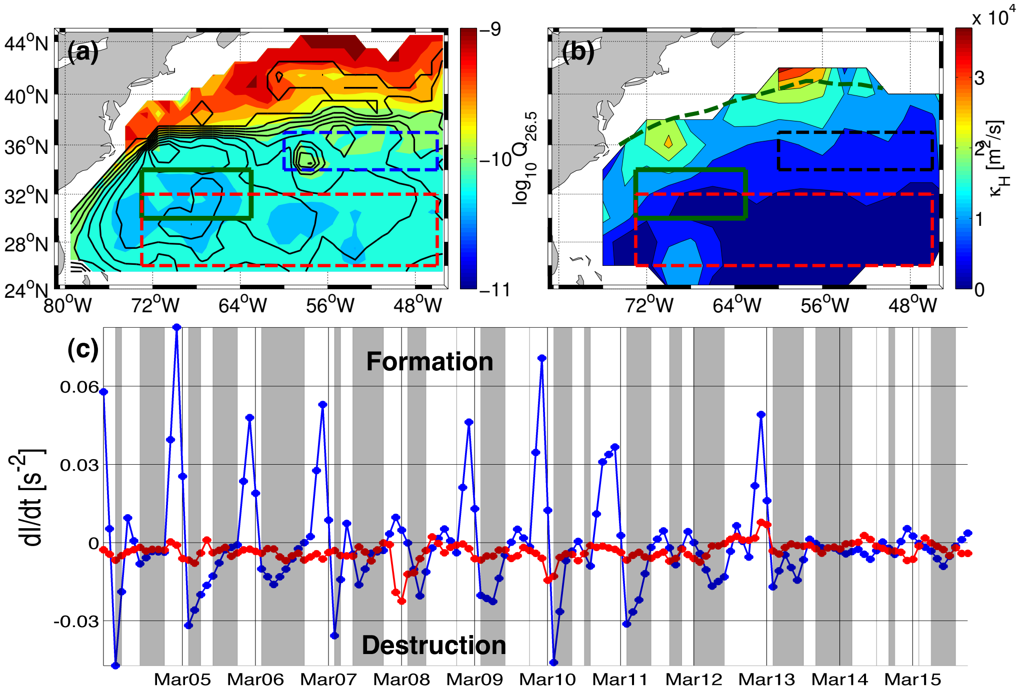

Figure 3.6: Isopycnal EDW destruction rate. (a) Potential vorticity at the EDW core, $\sigma_\theta = 26.5$, (color contours) and EDW thickness (black contours, 50 m intervals, ranging from 0-400 m) for October 2006 using *Roemmich and Gilson* [2009] gridded Argo data. See section 3.6.2 for description of dashed boxes. (b) Isopycnal diffusivity calculated from CLIMODE bobber velocity data. Dashed boxes are the same as shown in panel a. Dashed green curve shows the mean Gulf Stream position. (c) Total EDW destruction rate (blue) and isopycnal EDW destruction rate (red), calculated for the region outlined by the solid green box in panel a. Note that $dI/dt < 0$ indicates EDW destruction. Time periods for which both total and isopycnal EDW destruction rates are less than zero are highlighted by gray shading.

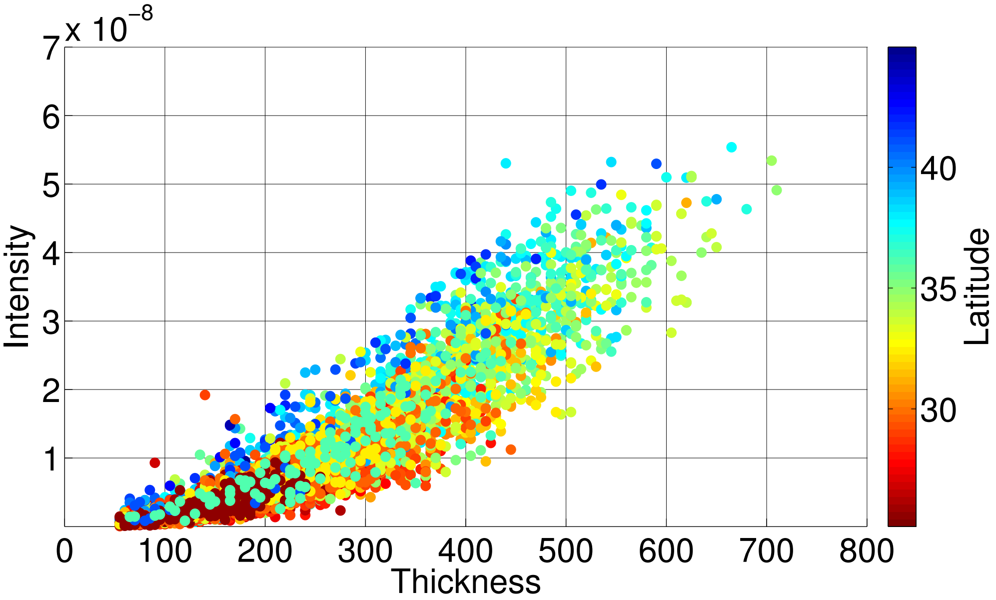

Figure 3.7: EDW thickness vs. EDW Intensity from Argo float profiles in the EDW region, where the EDW layer is defined as the low PV ($Q < 10^{-10}$ m^{-1}s^{-1}) portion of the potential density class, $\sigma_{EDW} = 26.2 - 26.7$ kg/m^3. EDW Intensity is defined in Equation 3.2. Color indicates profile latitude.

Chapter 4

Seasonality in upper ocean oxygen structure and utilization rate in the Sargasso Sea observed by profiling floats

4.1 Abstract

A comprehensive survey of seasonal oxygen structure and utilization in the Sargasso Sea is carried out using nine Clivar Mode Water Dynamics Experiment (CLIMODE) profiling floats equipped with oxygen sensors. A shallow oxygen maximum (SOM) layer consisting of supersaturated oxygen concentration is observed and reflects the annual development of the seasonal pycnocline. Within the SOM layer, nearly year-round net production indicates that the region is a net producer of fixed carbon, consistent with recent studies of subtropical open ocean net community production. The seasonality and depth dependence of oxygen utilization rates (OUR) are consistent with the seasonal maximum production in the SOM and sinking of particulate organic carbon (POC). Below the SOM lies a shallow

oxygen minimum produced by a layer of maximum remineralization, between $\sim 100-200$ m depth. From $\sim 200-500$ m, in the high-oxygen Eighteen Degree Water (EDW) layer, OUR steadily decreases with depth. The complex vertical structure of oxygen in the region, composed of multiple upward and downward gradients, suggests that vertical diffusive flux could play a role in modifying the oxygen distribution. The contribution of vertical mixing to the evolution of oxygen is assessed, with the conclusion that ignoring mixing in the oxygen rate of change would lead to 19% error underestimating the maximum remineralization rates and 88% error underestimating maximum net production rates. While the errors for estimating these maxima are substantial, vertical mixing makes a negligible contribution to oxygen evolution in deeper layers, so that the error in estimating total integrated remineralization would range from $5-9\%$.

4.2 Introduction

Oxygen in the ocean interior is sourced by ventilation and drawn down by aerobic respiration. It follows that, on a sufficient time scale, one can estimate the oxygen utilization rate (OUR) below the euphotic zone by physically tracing a previously ventilated water parcel while measuring its oxygen concentration [*Riley*, 1951]. OURs in the ocean interior indicate the strength of the biological pump, which biologically draws carbon from the atmosphere and sequesters it into the deep ocean. One can determine the net export of fixed carbon at a given depth by integrating the rate of the annual oxygen consumption below, inferring the amount of organic carbon required to sustain remineralization [*Jenkins*, 1982; *Martz et al.*, 2008; *Bushinsky and Emerson*, 2015]. That respiration is also correlated with the rate of regeneration of the nutrients that support photosynthesis. Thus, understanding the variability of remineralization in the ocean interior, in particular the rate, depth dependence, and seasonality, is fundamental when using oxygen concentrations to diagnose the carbon cycle. This variability is complicated by the modification of oxygen concentration by physical transport, including advection and mixing.

Upper ocean variability in the Sargasso Sea of the western North Atlantic is marked by the subtropical mode water, Eighteen Degree Water (EDW), erosion and regeneration and by the cycle of the seasonal pycnocline [*Worthington*, 1959]. The seasonal pycnocline is identified by the strongly stratified layer in the upper 200 m of the water column. The underlying EDW layer is defined by the portion of the $\sigma_\theta = 26.2 - 26.7$ kg/m^3 density layer with potential vorticity (PV) less than 1×10^{-10} m^{-1}s^{-1} [*Billheimer and Talley*, 2016b], where PV is defined neglecting relative vorticity on large scales:

$$PV = -\frac{f}{\rho}\frac{\partial \rho}{\partial z}, \tag{4.1}$$

where f is the Coriolis parameter and ρ is locally referenced density. Each winter, cold air outbreaks drive the formation of deep mixed layers through convection, destroying the seasonal pycnocline, injecting low PV and high, near-saturation O_2 concentration into the EDW layer. Beginning roughly in May, solar insolation drives the formation of the seasonal pycnocline, isolating the EDW layer from the surface. Over the course of summer and fall, EDW PV increases, due to mixing with surrounding water masses, while EDW oxygen decreases, driven by both mixing and aerobic remineralization. The uniform oxygen of the thick winter EDW layer provides a canvass for observing oxygen utilization rates throughout the remainder of the year while EDW is isolated from the atmosphere. The thickness of the layer also acts as a buffering zone, separating high nutrients below the main nutricline from the euphotic zone where they can be utilized.

The Sargasso Sea has a rich history of biogeochemical observations thanks to longstanding repeat hydrographic profiles at Station S and Bermuda Atlantic Time Series Study (BATS). Many studies have estimated OUR, primarily using two distinct methods. The first method models the oxygen budget, estimating the physical transport of oxygen by evaluating upper ocean advection and diffusion [*Riley*, 1951; *Ono et al.*, 2001], mixed layer/thermocline models [*Jenkins*, 1987], or inverse models [*Sarmiento et al.*, 1990; *Rintoul and Wunsch*, 1991], while observing changes in oxygen concentration. The second method evaluates the time rate of change of oxygen concentration, or "age equation" using various chemical tracers to determine the ventilation date [*Jenkins*, 1982; *Jenkins and Goldman*, 1985; *Sarmiento et al.*, 1990]. Assuming near-100% oxygen saturation during ventilation, one can take a single observation of oxygen saturation at a later time and determine the OUR using the chemical tracer age.

Jenkins and Goldman [1985] estimate OUR using the latter age equation approach (with He/H^3 ratios) and compare that estimate with seasonal changes in oxygen concentration at Station S. The authors find that OUR obtained from the age equation is consistent with observations of oxygen rate of change seasonally, though the oxygen rate of change is thought to ultimately underestimate biologically-driven OUR. The reasons for this are physical: (1) Not accounting for mixing. Seasonally, oxygen saturation is mirrored across the compensation depth, Z_c, defined as the depth at which Net Community Production (NCP) equals zero. Immediately after ventilation, during the development of the seasonal thermocline, photosynthetically produced oxygen in the euphotic zone drives the development of a Shallow Oxygen Maximum (SOM), where oxygen trapped beneath the seasonal thermocline develops a layer of supersaturation. Below the compensation depth, the SOM is mirrored by a layer of undersaturation, presumably driven by the oxidation of carbon rain, producing a clear seasonal cycle in OUR. Turbulence in the vicinity of this large vertical gradient in oxygen concentration would drive a substantial vertical flux of oxygen across Z_c, rendering an underestimate in OUR below Z_c. Conversely, mixing across the permanent pycnocline would enhance OUR estimates in the layer just below the compensation depth, though the effect would be less substantial due to weaker oxygen gradients in that part of the water column. (2) Not accounting for advection. The authors observe an increasing lag with depth in the seasonal oxygen maximum. The lag is explained by the Eulerian nature of the observations at Station S, located in the southern region of the tight recirculation gyre where recently ventilated water is advected in from the northeast, so that the lag in oxygen maximum results from the increasing distances from outcrops. This interior lateral transport of oxygen during the local non-ventilation season introduces an underestimate of OUR. The amplitude of the oxygen cycle decreases with depth, which is attributed to exponentially decreasing oxygen consumption rates combined with decreasing ventilation rates.

Ono et al. [2001], focusing on the seasonal pycnocline and 150m layer below the compensation depth, also observe a seasonal cycle in OUR that decreases with depth, with peak remineralization seasonally mirroring the development of the SOM. Combining six years of BATS oxygen data while estimating the effects of advection and diffusion on oxygen concentration, the authors find that turbulent mixing across Z_c has a large influence on the oxygen rate of change just below Z_c ($\sim 40\%$), with a secondary but also substantial contribution from advection ($\sim$ 25%). The net result is a substantial underestimation of OUR by observing oxygen rate of change without considering oceanic transport of oxygen concentration, agreeing with the previous inferences by *Jenkins and Goldman* [1985].

In recent years, the development of stable oxygen optode sensors [*Körtzinger et al.*, 2005] has allowed high quality, high resolution, year-round Lagrangian observations of the annual oxygen cycle by profiling floats [*Riser and Johnson*, 2008; *Martz et al.*, 2008;

Bushinsky and Emerson, 2015; *Hennon et al.*, 2016]. Profiling floats provide a new platform for observing the annual oxygen budget and estimating OURs, providing greater spatial coverage and reducing the effects of advection on that estimate.

With profiling floats equipped with oxygen sensors that span the northern Sargasso Sea, we can assess remineralization rates, depth dependence, and seasonality of oxygen concentration in the region. We also diagnose the effect of vertical turbulent flux on the seasonal evolution of oxygen using previous profiling float-based estimates of vertical eddy diffusivity.

4.3 Data and Methods

Nine APEX-SBE profiling floats were deployed in the Sargasso Sea region in November 2005 as part of the CLIVAR Mode Water Dynamics Exeriment (CLIMODE; *http://www-pord.ucsd.edu/climode_apexfloats/*). The profilers were equipped with conductivity-temperature-depth (CTD) instruments and Aanderaa oxygen optode sensors, parked at 500 dbar, and alternately profiled from 500 dbar and 1800 dbar to the surface every five days. Profiling float lifetimes ranged from 5.5 to 28 months. Float deployment and delayed mode calibration information is given in Table 4.1. See Figure 4.1 for a map of the float deployment locations and trajectories. Data from an individual float, “2721”, is presented in Figure 4.2.

4.3.1 Float Sensor Delayed Mode Calibration

Conductivity was corrected for thermal lag following *Johnson et al.* [2007] and corrections for salinity drift and offset were made using the methodology of *Owens and*

Wong [2009], using salinity data from alternating deep profiles. Delayed mode pressure corrections were made for all floats following protocol from the Argo QC manual.

Delayed mode corrections to oxygen optode sensors were made for all floats. The data were first corrected for pressure and salinity according to the optode manual (November 4, 2005), using the raw pressure and raw salinity. Next, a quality control process was performed by taking each float individually, partitioning the data into four depth bins (chosen relative to the sampling frequency- 0-200, 200-500, 500-1000, 1000-1850 dbar), and removing any data whose fluctuation from the mean was greater than three standard deviations, where the mean and standard deviation are relative to each depth bin for each float. This resulted in removing $\sim 0.1\%$ of the data. Then the pressure was re-corrected, reversing the suggested correction of the 2005 manual and using the recommended pressure compensation of 3.2% per 1000 dbar of *Uchida et al.* [2008], this time using the corrected pressure and salinity.

A final oxygen concentration dependent correction was made using bottle oxygen data from the CLIMODE hydrography campaign. Float oxygen was corrected by comparing the closest (in time and space) profiles of float optode oxygen to the Winkler-derived oxygen of the cruises. For each CLIMODE float, the closest float-to-cast profiles were found within a specified time window of 23 days. Bottle data above 100 m depth were excluded for use in the correction.

The comparison of float to bottle oxygen was considered on pressure or density levels, depending on the correlation of the bottle to float oxygen concentration. For example, float-to-bottle profile pairs near or within the Gulf Stream or far away from each other in space and/or time were especially more highly correlated when compared on density levels. Comparisons on pressure levels were more highly correlated where large oxygen gradients in density space existed. Seven out of nine floats were compared on density levels. The result of the comparison was an oxygen-dependent correction, derived from model II regression of the float-to-bottle oxygen difference, and was applied to the rest of the profiles of a given float.

Float oxygen records were also checked for sensor drift by comparing float oxygen time series on isopycnal levels with the WOCE Global Hydrographic Climatology (WGHC). For each float, the isopycnal level was chosen to be that with the least oxygen variation in the climatology. No evidence of significant sensor drift was found for any float.

The quality of the oxygen-dependent correction relative to the climatology was assessed for each float by comparing all float observations to WGHC on depth levels. The root mean square error relative to WGHC was reduced after the correction for all floats except for 2722, which had the shortest record (with only 17 full depth profiles) and spent its entire life in and out of the Gulf Stream, a region with large error for the climatology.

4.3.2 OUR and Float Profile Time Series

Remineralization rates were obtained by evaluating the equation for oxygen rate of change:

$$\frac{\partial O_2}{\partial t} + \mathbf{u} \cdot \nabla O_2 = \nabla \cdot (\mathbf{K} \cdot \nabla O_2) + OUR \tag{4.2}$$

where $\mathbf{u}$ is the velocity vector, $\mathbf{K}$ is a diffusivity tensor, and OUR is the remineralization-driven oxygen utilization rate. For simplicity, we have used the convention that $OUR < 0$ indicates oxygen consumption. Following the quasi-Lagrangian trajectories of profiling floats, advective terms are neglected. Then, also ignoring lateral mixing components, the oxygen utilization rate is given as follows:

$$OUR = \frac{\partial O_2}{\partial t} - \frac{\partial}{\partial z}\left(\kappa_z \frac{\partial O_2}{\partial z}\right) \tag{4.3}$$

where κ_z is vertical eddy diffusivity.

Seasonal estimates of upper ocean vertical diffusivity in the Sargasso Sea were obtained from the potential vorticity budget analysis of *Billheimer and Talley* [2016b]. One part of the profiling float analysis assumed that vertical mixing is the sole driver of the evolution of PV, leading to an upper bound estimate for κ_z just below the seasonal thermocline. Lateral mixing was also addressed, with the conclusion that lateral mixing in the northern Sargasso Sea is relatively steady and contributes up to 30% to the total seasonal PV evolution in the EDW layer. With this in mind (and with a lack of time-varying lateral oxygen gradient data), we ignore processes that mix oxygen laterally and apply the seasonally varying κ_z (ranging from $\sim 3 \times 10^{-5}$ to $\sim 17 \times 10^{-5}$ m^2/s) at 55 m, linearly fit in depth to a constant 1×10^{-5} m^2/s at 720 m, just above the permanent thermocline. This diffusivity profile is consistent with previous measurements of diapycnal diffusivity in the permanent pycnocline of the North Atlantic subtropical gyre [*Ledwell et al.*, 1993] as well as estimates above the permanent pycnocline that decrease with depth, from the 250m-500m depth interval to the 500m-1000m range [*Whalen et al.*, 2012].

Float data were averaged together annually to obtain a general representation of the Sargasso Sea seasonal cycle (Figure 4.3). Averaging also reduced abrupt changes in float oxygen concentrations on depth and density levels, when floats were occasionally caught in eddies or transported into different regimes in a non-Lagrangian fashion. An example of such sampling behavior is evident for float 2721 from August to November (Figure 4.2). Three floats (2713, 2719, and 2722) were deployed in the Gulf Stream, and are omitted from the average in order to obtain the best representation of the Sargasso Sea EDW region and to eliminate spurious rates of change of oxygen arising from crossing the Gulf Stream repeatedly. Float 2713 was deployed in the Gulf Stream, crossing multiple times and taking repeated forays into the northern and eastern Sargasso Sea before being rapidly swept eastward by the Azores current. Float 2719 was deployed in the Gulf Stream and eventually transported eastward into the North Atlantic Current. Float 2722 was deployed in the Gulf Stream and spent the remainder of its short life there. The average of the remaining six floats (Figure 4.3) consisted of roughly eight seasonal cycles. Float profiles were interpolated onto 5 m intervals and then averaged together in 15 day, 10 m bins.

In this study, oxygen rate of change was calculated on both depth and density levels (Figure 4.4 a,b) using a sliding six month time scale over the seasonally averaged float oxygen concentration. That is, for every 15 day time step, a line was fit to the oxygen concentrations spanning 90 days before and after the time step (on a looping annual record), the slope of which yielded dO/dt. Depth levels were 0-800 m on 10 m intervals while density levels were σ_θ =25.7-26.3 kg/m^3 on 0.2 kg/m^3 intervals and σ_θ =26.4-27.1 kg/m^3 on 0.05 kg/m^3 intervals, since a coarser range of isopycnals was needed to represent even depth spacing within the seasonal pycnocline.

The vertical gradient of oxygen was calculated uniformly on a 50 m vertical scale, while the second derivative was calculated on a 50 m scale above 200 m depth and on a 100 m vertical scale below 200 m depth.

Changes in oxygen concentration due to aerobic remineralization are often described by

$$\Delta[O2]_{remin} = [O2]_{observed} - [O2]_{preformed} \tag{4.4}$$

so that the time rate of change gives OUR. Since oxygen is close to saturation during ventilation, it is convenient to define OUR as $-AOU/\Delta t$, where $AOU = [O_2]_{sat} - [O_2]_{observed}$ and where Δt is the time since ventilation. This can be advantageous when an observation of oxygen is paired with a tracer indicating time since ventilation, or "age", since observations in only one point in time are required to determine OUR. Profiling floats provide a high temporal resolution of oxygen observations, enabling us to refrain from the common approach of defining OUR as time rate of change of AOU, and instead define OUR in terms of oxygen concentration rate of change. Focussing on the water column below the mixed layer, temperature effects on oxygen solubility do not affect oxygen concentration, so that rate of change of oxygen concentration is the most appropriate choice for estimation of OURs.

4.4 Results

4.4.1 Seasonal Cycles

We describe the seasonal cycle of potential temperature, PV, and oxygen concentration in five distinct layers: the seasonal pycnocline, shallow oxygen maximum layer, shallow oxygen minimum layer, EDW layer, and permanent pycnocline.

Seasonal Pycnocline

The seasonal cycle of potential temperature in the northern Sargasso Sea (Figure 4.3a) is fairly steady on all depth levels other than the upper 150 m (and below 500 m, discussed in Section 4.4.1). The seasonal pycnocline warms from May to September. During this time oxygen decreases just above the seasonal pycnocline, consistent with decreasing oxygen solubility and outgassing. Conversely, as this layer cools beginning in mid-September, the oxygen concentration begins to increase, consistent with enhanced solubility and ingassing.

In early winter, deeper mixed layers begin to form, also increasing the oxygen concentration in the uppermost layer. At the onset of surface cooling in mid-September, Figure 4.3b demonstrates that the seasonal pycnocline begins to weaken and deepen until it is obliterated by the deep mixed layers that connect all the way through to the underlying EDW layer in late winter.

Shallow Oxygen Maximum

Just below the seasonal pycnocline, a Shallow Oxygen Maximum develops (often referred to as the "SOM"). The phenomenon is known as the Schulenberger-Reid effect [*Shulenberger and Reid*, 1981], where oxygen supersaturation is observed within the euphotic zone, beneath the development of a seasonal thermocline in spring. The seasonal thermocline acts as a barrier for oxygen outgassing, trapping photosynthetically produced oxygen below.

Riser and Johnson [2008] used profiling floats equipped with oxygen sensors to observe the shallow oxygen maximum in the subtropical North and South Pacific. The observed continuous growth of the shallow oxygen maximum ($\sim$0.05 μmol/kg/day in the subtropical North Pacific and $\sim$0.025 μmol/kg/day in the subtropical South Pacific) was used to show that the subtropical euphotic zone is an annual net producer of fixed carbon, contrary to previous bottle experiments, without having to invoke episodic bloom events.

In the euphotic zone of the Sargasso Sea, the shallow oxygen maximum was described by *Jenkins and Goldman* [1985], who confirmed that it is of photosynthetic origin in this region, but complicated by the loss of oxygen to the atmosphere and downward mixing as the seasonal thermocline breaks down. The reported increase in oxygen concentration in the SOM between March and July was 0.20 ml/l, corresponding to an oxygen rate of change of ~ 0.071 μmol/kg/day.

Figure 4.3 shows that the shallow oxygen maximum reflects the strength and depth of the seasonal pycnocline. Supersaturation of oxygen begins to develop in early May, as photosynthetically produced oxygen is trapped beneath the newly-formed seasonal pycnocline. Oxygen concentration in this layer continues to increase until September, when surface heating changes sign and the seasonal pycnocline begins to weaken. As the surface mixed layer gradually deepens, isopycnals are successively stripped from the seasonal pycnocline and outcrop, deepening the extremum of the seasonal pycnocline. As this occurs, the SOM begins to equilibrate from the top, reducing its magnitude and revealing a new, deepening maximum that tracks the seasonal pycnocline downward until both the pycnocline and SOM are destroyed by the winter convection that produces and ventilates the EDW.

Note that temperature in the seasonal thermocline increases during the time of the development of the oxygen maximum, penetrating to the depth of the oxygen maximum layer. Below the mixed layer, this does not change the oxygen concentration, but does have an influence on AOU, leading to differing rates of change of oxygen concentration vs. AOU. We focus on time rate of change of oxygen concentration as the more appropriate indicator of OUR.

Shallow Oxygen Minimum

Just below the euphotic zone and below the SOM, at ~ 100 m, an oxygen minimum layer appears (Figure 4.3c). The existence of this layer is consistent with previously estimated OUR depth profiles, which peak just below the compensation depth and exponentially decrease with depth [*Riley*, 1951; *Jenkins*, 1980; *Martin et al.*, 1987; *Jenkins*, 1987; *Sarmiento et al.*, 1990; *Martz et al.*, 2008]. In late winter, the mixed layers that regenerate

EDW greatly exceed the compensation depth, introducing a nearly uniform, near-saturation oxygen concentration. Oxygen consumption just below the compensation depth draws down the oxygen concentration the fastest, leaving behind the shallow oxygen minimum layer. In other regions, shallower mixed layers that do not exceed the compensation depth (or that only exceed Z_c by a small amount) produce an oxygen gradient that already decreases with depth before the exponentially decreasing profile of OUR is allowed to act to produce a shallow oxygen minimum.

EDW Layer

The EDW layer is characterized by nearly uniform temperature, with a low PV core residing between the σ_θ=26.4 and σ_θ=26.5 isopycnals. EDW is formed in late winter, when convective mixing injects high oxygen concentration into deep mixed layers. While the average late winter mixed layer depth among CLIMODE floats is $\sim$ 250 m (Figure 4.3), winter mixed layer depths regularly exceed this level in the most intense EDW formation region in the northern Sargasso Sea near the Gulf Stream extension [*Worthington*, 1972a], reaching as deep as 450 m in some cases (Figure 4.2). This deep introduction of high oxygen concentration is apparent in Figure 4.3c, as oxygen concentration increases from 250 m to 450 m during late winter. The increasing oxygen at this level lags with an increase in depth, indicating oxygen introduction via advection and lateral stirring.

After the development of the seasonal pycnocline in May, isolating the EDW layer from the atmosphere, the oxygen concentration appears to decrease at seasonally variable rates: From May through July, oxygen appears to be rapidly depleted, while from August through December the rate appears to decrease.

Permanent Pycnocline

The permanent pycnocline, which resides beneath the EDW layer, appears to deepen from winter to early summer and shoal from summer to autumn. This can be seen by following the depth of the σ_θ=26.5 to σ_θ=27.0 isopycnals in Figure 4.3. Previous studies conjecture that the depth of the subtropical gyre permanent pycnocline exhibits seasonality consistent with that observed in Figure 4.3 [*Worthington*, 1972b] and observe permanent pycnocline deepening by 100 to 150 m in regions with intense late winter convective mixing [*Worthington*, 1977]. Additionally, the late summer shoaling of isopycnals in Figure 4.3 appears to be influenced by a significant number of floats sampling cyclonic eddies during the same months (Float "2721" of Figure 4.2 provides an example). From August to October, EDW layer PV and oxygen exhibit an inflection point, so that the rate of change of each quantity changes sign in September. This behavior must be a spurious result of sampling, since there are no sinks of PV in subducted EDW during this time of year and EDW PV tends to consistently increase.

4.4.2 Oxygen Rate of Change

We calculate the oxygen rate of change in both depth and density layers. The result of each calculation is described below, and we go on to combine the results in an attempt to compensate for the deficiencies that each method presents. Oxygen rates of change, calculated from temporal derivatives of Figure 4.3c, are shown in Figure 4.4. Each plotted time step represents the middle of a six-month differentiation time scale. Note that these rates of change are not our final estimate of OUR, which includes an adjustment for vertical mixing (Section 4.4.3).

Figure 4.4a shows the oxygen time rate of change with differentiation along depth levels. In the upper 300 m, note the late winter ingassing and introduction of oxygen via mixed layer development. When the seasonal pycnocline develops beginning in May, the near-surface layer warms, driving oxygen outgassing above the mixed layer depth. When surface heat flux changes sign in September, the oxygen rate of change in this surface layer reverses, indicating oxygen ingassing as a result of enhanced solubility.

Below the seasonal pycnocline, a thin, $\partial O_2/\partial t > 0$ layer driving the development of the SOM appears from May to mid-August, descending from ~ 40 to ~ 75 m. A $\partial O_2/\partial t < 0$ tongue, descending over the same depth range from Semptember to December, is an artifact of isobaric differentiation, differentiating across a deepening SOM that reflects the seasonal pycnocline and descends from summer into autumn.

A layer of maximum oxygen consumption is observed, peaking in magnitude from May to August at depth levels between 100 to 150 m. This layer also reflects the seasonality of the SOM and seasonal pycnocline, descending while weakening from July to December, where the maximum reaches a depth of 250 m.

Below 300 m depth, it is clear that the oxygen rate of change is dominated by the heaving of isopycnals discussed in Section 4.4.1. The oxycline is coherent with the permanent pycnocline (Figure 4.3c), so that when density changes along an isobar there is a corresponding change in oxygen concentration. From January to May, as isopycnals below 300 m descend, oxygen concentration uniformly increases throughout the water column below 300 m. From May to September, the reverse occurs. As isopycnals descend over a short time period beginning in September, it is reflected by the rate of change of oxygen along isobars between October and December.

In order to get the best representation of OUR below 300 m, where $\partial O_2/\partial t$ is greatly influenced by heaving isopycnals, we differentiate oxygen concentration along isopycnal levels. Oxygen concentration in isopycnal coordinates is shown in Figure 4.4b. Note that for densities greater than $\sigma_\theta = 26.5$, oxygen concentration is much more uniform in time, compared with oxygen in depth coordinates below 400 m in Figure 4.4a.

Differentiation of oxygen concentration along isopycnals produces a more reasonable description of oxygen evolution below 300 m than differentiation along isobars. Figure 4.4c shows the rate of change of oxygen concentration in isopycnal coordinates, projected back to depth coordinates using mean isopycnal depth. In late winter, introduction of mixed layer, high oxygen concentration penetrates the deeper layers through advection and along-isopycnal stirring. The lag of high oxygen concentration with depth is to be expected. While we estimate the mean mixed layer depth of the Sargasso Sea to penetrate as deep as 250 m, mixed layer depths in the most intense EDW formation regions exceed 500 m. Over the course of the summer, along-isopycnal transport of oxygen fills in the deeper isopycnals of the recirculation gyre (and therefore the Sargasso Sea mean), producing deep oxygen rates of change that are positive during this time of year. Below 600 m (densities greater than $\sigma_\theta = 26.8$), we suspect that the observed positive rate of change of oxygen is a result of along-isopycnal mixing of oxygen with water masses ventilated north of the Gulf Stream.

Large $\partial O_2/\partial t$ magnitudes in the upper 200 m of Figure 4.4c are a result of isopycnal outcropping in winter and isopycnal subduction in summer, and do not reflect the depth-dependent nature of oxygen consumption and production. In winter, when isopycnals outcrop, oxygen dramatically increases due to oxygen ingassing. In summer, when isopycnals subduct under the effect of downward surface heat flux, they cross depths of net oxygen production (i.e. the SOM), cross the compensation depth, and descend into a layer of maximum oxygen consumption (i.e. the shallow oxygen minimum). This subduction produces a spurious, large magnitude negative oxygen rate of change during this time of year.

In order to obtain the best representation of oxygen evolution throughout the water column, we combine the portions of Figure 4.4a and Figure 4.4c that do not produce spurious features. We choose a midpoint isopycnal of $\sigma_\theta = 26.4$ because it does not outcrop or cross the compensation depth, is not affected by fluctuations in the permanent pycnocline depth, and does not appear to be influenced by the eddy sampling discussed in Section 4.4.1. The mean depth of $\sigma_\theta = 26.4$ is 250 m, so we take the upper 250 m of Figure 4.4a and the 250 to 800 m depth range of Figure 4.4c, splicing the two together with linear interpolation to produce Figure 4.4d.

Figure 4.5 shows mean profiles of Figure 4.4d, summarizing its features during the time of year when the seasonal pycnocline remains intact. Averages are taken separately over early summer and late summer/autumn, and over both three-month periods from May to November.

In the uppermost portion of the water column, within the mixed layer, seasonal in/outgassing of oxygen is apparent. From May to August, outgassing is observed due to seasonal warming of the layer decreasing solubility. From August to November, mean outgassing occurs due to mean seasonal cooling.

Below the seasonal pycnocline, between 50 and 100 m, peaks in $\partial O_2/\partial t$ indicate the maximum net production layer that forms the SOM. Note that the peak weakens and descends seasonally, from May-August to August-November, reflecting the behavior of the seasonal pycnocline. Since the peak in $\partial O_2/\partial t$ changes depth seasonally, averages across depth levels mask its magnitude, disguising the persistent tongue of positive $\partial O_2/\partial t$ from May to September (visible in Figure 4.4d) that produces the SOM.

Negative peaks in the 100 to 200 m range indicate the maximum consumption layer that produces the shallow oxygen minimum. These peaks mirror the maximum net production layer above: $\partial O_2/\partial t$ is strongly negative from May to August, while weaker and deeper from August to November.

Across the EDW layer, from 200 to 500 m, oxygen depletion decreases approximately linearly with depth. Below 500 m, there is an early summer net introduction of oxygen via along-isopycnal transport (discussed above).

It is important to consider Figure 4.5 only as a description of oxygen rates of change, rather than using it to directly infer estimates of NCP and remineralization rates. With a significant contribution from turbulent mixing, equating oxygen rate of change with OUR could lead to large error (Equation 4.3). We expect this to be the case, considering the significant correlation between subsurface oxygen and PV observed in the subducted EDW layer (Figure 4.6). If both quantities evolved linearly, one would expect a strong correlation, but the evolution of each could be driven by separate mechanisms. Neither PV nor oxygen concentration evolves linearly with time [*Billheimer and Talley*, 2016b], (Figure 4.4d), so the fact that they are strongly correlated ($r = -0.63$, 95% significance level of 0.015, zero lag on 5-day resolution) suggests a shared evolution mechanism that is physical in nature.

4.4.3 Vertical Mixing

In this section we consider the influence of vertical mixing on the seasonal evolution of oxygen in the Sargasso Sea. The contribution of vertical mixing is analyzed by diagnosing the components of the last term of Equation 4.3.

The vertical gradient of oxygen in the Sargasso Sea has a rich vertical structure and reflects the seasonality of the SOM, shallow oxygen minimum layer, and EDW layer(Figure 4.7a). At the bottom of the EDW layer at 500 m, a band of $\partial O/\partial z > 0$ persists throughout the year, as oxygen increases upward from the underlying permanent pycnocline to the oxygen-rich EDW layer. At the top of the EDW layer at ~ 200 m, the sign of the gradient reverses to $\partial O/\partial z < 0$, ascending from the EDW layer to the shallow oxygen minimum. Transitioning from the shallow oxygen minimum to the SOM at ~ 100 m, the oxygen gradient reverses sign once again, becoming strongly positive. There is one final sign reversal, crossing from the SOM into the mixed layer, which has a lower oxygen concentration. The upper 300 m bands of positive and negative oxygen vertical gradient seasonally track the progression of the SOM and shallow oxygen minimum, deepening throughout the subduction season. The second vertical derivative of oxygen (Figure 4.7b) is weakly positive just below the EDW layer, weakly negative within the EDW layer, strongly positive in the shallow oxygen minimum layer, and very strongly negative in the SOM.

Seasonally varying vertical eddy diffusivity, κ_z, is taken from *Billheimer and Talley* [2016b], based on PV evolution in the EDW layer (see Section 4.3.2 for details). κ_z is applied below the mixed layer depth only, with seasonal values ranging from $\sim 3 \times 10^{-5}$ m^2/s in September to 17×10^{-5} m^2/s in April. The profile of κ_z consists of the time varying value at 55 m linearly interpolated to the fixed value of 1×10^{-5} m^2/s at 720 m, just above the permanent pycnocline.

The mixing term of Equation 4.3 is plotted in Equation 7c, calculated using the time-evolving κ_z profile described above and the vertical oxygen gradient of Figure 4.7a and taking the vertical derivative of the product. The color scale is identical to Figure 4.4d for simplified comparison. Outside of the mixed layer, the result is weakly seasonal, with its dominant features summarized by the May to November mean profile (Figure 4.7c).

In the SOM layer, vertical mixing reduces the observed rate of change (incline) of oxygen. Turbulent mixing in this layer introduces low oxygen water from the seasonal pycnocline above and from the oxygen minimum layer below. Therefore, ignoring vertical mixing in this oxygen maximum layer would result in an overestimate of respiration and hence an underestimate of NCP.

The effect of mixing on the EDW layer oxygen concentration is similar, although much weaker. Low oxygen water from the oxygen minimum layer above and low oxygen water from the permanent thermocline below are transported via turbulent flux into the oxygen-rich EDW layer. Thus, again in this oxygen maximum layer, ignoring vertical mixing would result in an overestimate of remineralization rate.

Turbulent mixing of oxygen-rich water from the SOM and EDW layers into the shallow oxygen minimum layer produces the reverse effect. That is, ignoring vertical mixing would result in a lower remineralization rate estimate.

The turbulent mixing rate of oxygen (Figure 4.7c) is subtracted from the oxygen rate of change (Figure 4.4d) to produce an OUR estimate (Figure 4.8a). In comparison with the oxygen rate of change, the estimate of OUR primarily differs by revealing enhanced magnitudes of remineralization rate and NCP in the shallow oxygen minimum layer and SOM, respectively. Seasonally, the estimate of OUR features a seasonally continuous oxygen production layer, indicating a layer of positive NCP throughout the time of year when the seasonal pycnocline remains intact. Note that our estimate of OUR is limited to the water column below 55 m since that is the deepest level at which we could generate estimates for second vertical derivatives using reasonable vertical length scales. Additionally, OUR is not presented above the mixed layer depth since our estimates of κ_z are not valid there.

To quantify the effect of vertical mixing of oxygen on NCP and remineralization rates, we select a small temporal span of profiles from Figure 4.8a and compare their average to the corresponding time frame from Figure 4.4d (Figure 4.8b). This method provides a simple comparison to previous profiling float studies that produce a single seasonal estimate of OUR (or NCP) by fitting a line to oxygen concentrations over a set period of time, usually a six to eight month time scale [*Riser and Johnson*, 2008; *Martz et al.*, 2008; *Hennon et al.*, 2016]. The time scale in these studies is chosen during the time of year when the mixed layer does not influence interior oxygen concentration. For this reason we select August profiles of $\partial O_2/\partial t$ and OUR. Due to the six month differentiation time scale employed in this analysis, an individual August profile represents a rate of change using information from May to November, excluding mixed layer data. These profiles provide our best estimate for the overall annual magnitude of OUR.

The overall effect of vertical mixing on the annual magnitude of OUR is negligible in all of the water column except in the extrema in the upper 200 m (Figure 4.8b). As suggested by the profile of vertical mixing contribution to OUR (Figure 4.7d), ignoring the effects of vertical mixing of oxygen reduces estimates of both NCP in the SOM layer and remineralization rate in the shallow oxygen minimum layer. For the most extreme values, not including vertical mixing in a remineralization rate estimate would produce a 19% error (0.099 μmol/kg/day, or 0.081μmol/kg/day ignoring mixing). Not including vertical mixing in an estimate for net production in the SOM would be more severe, producing an error of 88% (0.042 μmol/kg/day, or 0.005μmol/kg/day ignoring mixing). By evaluating the nitrate budget of Station S data, *Jenkins and Goldman* [1985] estimate that the downward turbulent flux of photosynthetically produced oxygen in the region produces a 24% error in OUR integrated from 100 to 400 m (5.4 M/m^2/yr, or 4.1 M/m^2/yr ignoring mixing). Integrating from the compensation depth to 400 m using our profiling float-based estimate of OUR in the northern Sargasso Sea, we obtain a much smaller underestimate introducing only 5% error (6.2 M/m^2/yr, or 5.9 M/m^2/yr ignoring mixing). The large difference in estimated downward turbulent flux of photosynthetically produced oxygen in these studies (0.3 M/m^2/yr vs. 1.3 M/m^2/yr) may stem from analyzing the PV budget to obtain mixing rates vs. evaluating the nitrate budget to determine the flux of correlated oxygen. *Ono et al.* [2001] apply a constant vertical diffusivity of 1×10^{-4} m^2/s to seasonally averaged oxygen concentrations from six years of BATS sampling, and conclude that vertical mixing of photosynthetically produced oxygen introduces an error of 23% in remineralization estimates, integrated from 100 to 250 m over 240 days (2.08 ± 0.38 M/m^2, with a contribution of 0.48 ± 0.12 M/m^2 by removing effects of vertical mixing). In this study, vertical mixing produces only 9% error in OUR integrated to 250 m depth (2.84 M/m^2, with a contribution of 0.25 M/m^2 by removing effects of vertical mixing). The enhanced mixing contribution of *Ono et al.* [2001] likely results from the application of a flat vertical eddy diffusivity of 1^{-4} m^2/s, compared to the application of a vertical diffusivity in this study that seasonally varies and tapers with depth.

Comparing the vertical structure of $\partial O_2/\partial t$ against OUR, the estimated compensation depth at 78 m is negligibly modified. Within the limitations of our chosen 10 m vertical resolution, extrema in the upper 200 m are slightly shallower when considering OUR, with peak NCP occurring at 65 m and peak consumption occurring at 115 m, rather than at 75 m and 125 m, respectively.

4.4.4 Seasonal NCP and Remineralization Rates

The oxygen cycle in the upper ocean of the Sargasso Sea is marked by strong seasonality in both photosynthetic production of oxygen and remineralization. We use our time series of OUR (Figure 4.8a) to qualitatively describe seasonal cycles, while referencing the mean August profile of OUR (Figure 4.8c) to quantitatively compare our results to previous studies.

The most notable feature of the SOM layer is the persistence of a positive production layer throughout the time of year when the layer is capped by the seasonal pycnocline (Figure 4.8a). This suggests that NCP is positive throughout the entire year, indicating that the Sargasso Sea is a net producer of fixed carbon. Mass balance estimates at BATS, along with time series located in other subtropical regions, agree [*Emerson*, 2014]. Profiling floats equipped with oxygen sensors have been employed to show the same result in both the subtropical North and South Pacific [*Riser and Johnson*, 2008]. The positive NCP layer appears to be strongest and shallowest from May to August, weakening and deepening from August to November (Figure 4.8c). The maximum magnitude is attributed to the maximum production and spring bloom that occurs in the region during spring [*Michaels and Knap*, 1996]. We attribute the apparent deepening of the maximum production layer to the erosion of the seasonal pycnocline and consequent outgassing of supersaturated oxygen that slowly occurs from the top. The compensation depth also varies seasonally, consistent with *Ono et al.* [2001], ranging from 55 m in May to 95 m in October Figure 4.8a. The August compensation depth (representing the overall May to November seasonal value) is 78 m.

The seasonal cycle of respiration is extremely prominent from the compensation depth down to 200 m, mirroring the cycle of net production above (Figure 4.8 a,c). As is found by *Ono et al.* [2001], the mirroring is consistent with the paradigm that seasonal remineralization is driven by sinking particulate organic carbon (POC), maximized during the spring bloom, although remineralization of dissolved organic carbon (DOC) is also enhanced during this time of year [*Carlson et al.*, 1994]. While the net remineralization qualitatively mirrors production in the layer above, we do not attempt to construct the annual NCP integrated through the seasonal pycnocline and mixed layer to construct the oxygen budget quantitatively.

For a comparison of magnitudes with other studies, we select a mean of August profiles of OUR (Figure 4.8b) as our best estimate of the overall magnitude of annual OUR. Due to the six month differentiation time scale, interpretation of the OUR magnitudes presented in Figure 4.8a should be approached with caution when this temporal window overlaps with the mixed layer. The method allows for a sliding and adjustable scale for computing OUR, yielding a qualitative picture of its seasonality, but error is associated with estimates a few months before and after oxygen is introduced via deep winter mixed layers.

Within the SOM layer, we infer a net production rate of 0.04 μmol/kg/day in the Sargasso Sea. This rate is within the range of estimates by *Riser and Johnson* [2008] of 0.05 μmol/kg/day in the subtropical Pacific near the Hawaiian Ocean Time Series (HOT) and 0.025 μmol/kg/day in the subtropical South Pacific.

In the shallow oxygen minimum layer, where remineralization is at an extreme, we estimate a remineralization rate of 0.099 μmol/kg/day, significantly higher than the range of maxima summarized by *Sarmiento et al.* [1990] of 0.013 to 0.063 μmol/kg/day, but more conservative than the maximum rate of 0.14 μmol/kg/day found by *Ono et al.* [2001]. Averaging together several profiles of oxygen rate of change from profiling floats in the Sargasso Sea, *Hennon et al.* [2016] estimate a maximum remineralization rate of $0.077\pm.031$ μmol/kg/day, centered identically on the value of $\partial O_2/\partial t$ shown in Figure 4.8b before removing the effects of mixing.

In the low PV EDW core at 300 m, the remineralization rate is estimated at 0.038 μmol/kg/day. This rate falls between previous estimates by *Worthington* [1959] and *Palter et al.* [2005], who use very different methodologies. *Worthington* [1959] reports oxygen observations from *Rakestraw and Carritt* [1948], who repeatedly occupied a Montauk-

Bermuda section during 1937-1938. In the EDW formation region in the Sargasso Sea, biological consumption of oxygen in the EDW core is reported at 0.060 μmol/kg/day over the course of nine months. *Palter et al.* [2005] utilize World Ocean Circulation Experiment (WOCE) sections through the EDW region in the Sargasso Sea to estimate an EDW remineralization rate of 0.015 ± 0.004 μmol/kg/day. This estimate is produced by computing $-AOU/\Delta t$ (discussed in Section 4.3.2), where Δt, the time since ventilation, is given by CFC age. We suspect that the estimate of *Worthington* [1959] is substantially larger than both *Palter et al.* [2005] and our estimate because it does not take into account the substantial vertical and lateral mixing that takes place in the EDW formation region in the northern Sargasso Sea, introducing high PV, low oxygen water to the EDW layer. It is possible that the results of all three studies differ due to interannual variability: Remineralization of sinking POC mirrors NCP, and net annual primary productivity is known to vary interannually depending on the severity of winter mixing in the region.

Integrating OUR from the compensation depth to the zero crossing at 425 m, we obtain a total remineralization estimate of 4.09 mol O_2/m^2 over 240 days, corresponding to 4.2 mol C/m^2 export production extrapolated through the year using $1.45\,O_2 : 1\,C_{org}$ [*Anderson and Sarmiento*, 1994]. This integrated estimate is greater than mass balance estimates of annual net community production at BATS of 2.5 ± 1.2 mol C/m^2/yr [*Emerson*, 2014], indicating that either we have overestimated export production or export production is enhanced in the northern Sargasso Sea compared with Bermuda. The latter is unlikely considering the apparent consistency of global subtropical NCP estimates [*Emerson*, 2014].

For simple comparison with other studies, we integrate from 100 to 250 m to obtain a shallow remineralization estimate of 2.86 mol O_2/m^2. This compares with estimates by *Ono et al.* [2001] of 2.08 ± 0.38 mol O_2/m^2 over 240 days (April-December) and *Jenkins and*

Goldman [1985] 1.7-3.0 mol O_2/m^2 (April-November) and falls within the range of Sargasso Sea estimates summarized by *Sarmiento et al.* [1990] of 0.6-3.3 mol O_2/m^2 annually.

Positive rates of change of oxygen below 430 m (Figure 4.8 b) result from the introduction of oxygen via along-isopycnal mixing, which was ignored in Equation 4.3. Averaging oxygen data from the quasi-Lagrangian profiling floats produces a quasi-Eulerian estimate of OUR, so one might attribute the increases in oxygen at depth to advection. In this scenario, months after deep ventilation in the most intense EDW formation regions, high oxygen concentration is advected at depth throughout the remainder of the gyre. Calculating OUR for individual profiling floats, *Hennon et al.* [2016] also observe in increase in oxygen below 500 m during this time of year in subtropical mode water regions. Since neither *Hennon et al.* [2016] nor this study account for along-isopycnal mixing, we believe homogenization of oxygen via mixing along the deepest EDW isopycnals plays a large role in producing this effect.

4.5 Conclusions

In this study we provide a comprehensive survey of Sargasso Sea seasonal oxygen structure and utilization using profiling floats. It is the first such survey, to our knowledge. The results are summarized as follows:

(1) We observe a seasonality and depth dependence of OUR that is consistent with the seasonal maximum production and sinking of POC. Maximum late spring production in the Sargasso Sea is mirrored by maximum remineralization in the layer below, with a profile of OUR that decays with depth.

(2) A layer of positive NCP near the bottom of the euphotic zone exists from May to November, and possibly year-round, indicating that the Sargasso Sea is a net producer

of fixed carbon. This result is complementary to previous studies showing the same result at BATS and in other subtropical regions of the global ocean [*Riser and Johnson*, 2008; *Emerson*, 2014].

(3) The contribution of vertical mixing to estimates of OUR is substantial, enhancing remineralization estimates in the shallow oxygen minimum layer while enhancing production estimates in the SOM layer. Vertical mixing makes a small contribution to OUR in the EDW layer, reducing estimates of remineralization. Considerations of vertical mixing also contribute to the seasonal structure of OUR, enhancing production estimates in the SOM in late summer. The finding that vertical mixing plays a substantial role in modifying oxygen rates of change may be applicable to other parts of the world upper ocean, particularly regions with large vertical oxygen gradients such as the oxygen minimum zone in the tropics.

(4) We observe a seasonal fluctuation in depth and strength of the SOM that coincides with the depth and strength of the seasonal pycnocline, which indicates the prominent role that stratification plays on the seasonality and depth structure of the Sargasso Sea oxygen distribution.

(5) We show that the oxygen rate of change provides more accurate representation of the evolution of oxygen when calculated on depth levels above maximum mixed layer depth, and when calculated in density coordinates for deeper levels.

(6) We observe magnitudes of OUR throughout the water column and depth integrated remineralization that fall within the range of previous Sargasso Sea studies that use a wide range of methods.

This study does not attempt to close the upper ocean oxygen budget or the budget of any other biogeochemical variable. Our estimates of NCP and remineralization are not balanced, as one would expect them to be on an annual time scale [*Brix et al.*, 2006]. We have not considered the influences of mixed layer development and gas exchange that play large roles in the oxygen evolution in the upper 200 m of this region and leave that analysis to later study. We also anticipate error in OUR estimates associated with neglecting advection and lateral diffusion, which may be significant at times of year within months of the maximum mixed layer depth and in the deeper layers of our domain.

With the ongoing deployment of profiling floats equipped with oxygen sensors in this region, one could extend this study to examine the influence of interannual variability of EDW formation on remineralization rate and structure. The large interannual variability of EDW formation has a significant impact on annual net production in the region [*Palter et al.*, 2005], and therefore may influence the remineralization of POC and overall export production on interannual time scales.

Table 4.1: CLIMODE float deployment and delayed-mode calibration: CLIMODE float UW ID number, date, number of 500 dbar profiles (n_p), time and distance between the closest float profile and bottle cast (Δt, Δd), correlation coefficients between matches on density and pressure levels (r_σ, r_p), and approximate magnitude of oxygen-dependent correction (Δo_{cor}). $\Delta t < 0$ indicates that the nearest float profile to a bottle cast occurred before the bottle cast.

UW ID	Deploy date	Last date	n_p	Δt (days)	Δd (km)	r_σ	r_p	Δo_{cor} (μmol/kg)
2713	11/10/2005	10/31/2007	143	4	38	0.9976	0.6789	< 5
2719	11/13/2005	10/13/2007	139	6	137	0.9971	0.9628	$5 - 8$
2720	11/17/2005	10/07/2006	65	15	74	0.9761	0.9528	$10 - 25$
2721	11/17/2005	09/03/2007	130	-13	42	0.9625	0.9719	< 5
2722	11/14/2005	04/27/2006	34	-6	11	0.9637	0.9810	$10 - 25$
2723	11/18/2005	05/22/2007	109	14	67	0.9876	0.9782	$22 - 30$
2724	11/20/2005	04/08/2008	174	-14	44	0.9940	0.9826	$22 - 30$
2725	11/23/2005	07/21/2006	48	23	88	0.8857	0.8575	15
2726	11/15/2005	01/18/2007	86	15	68	0.9944	0.9920	$10 - 15$

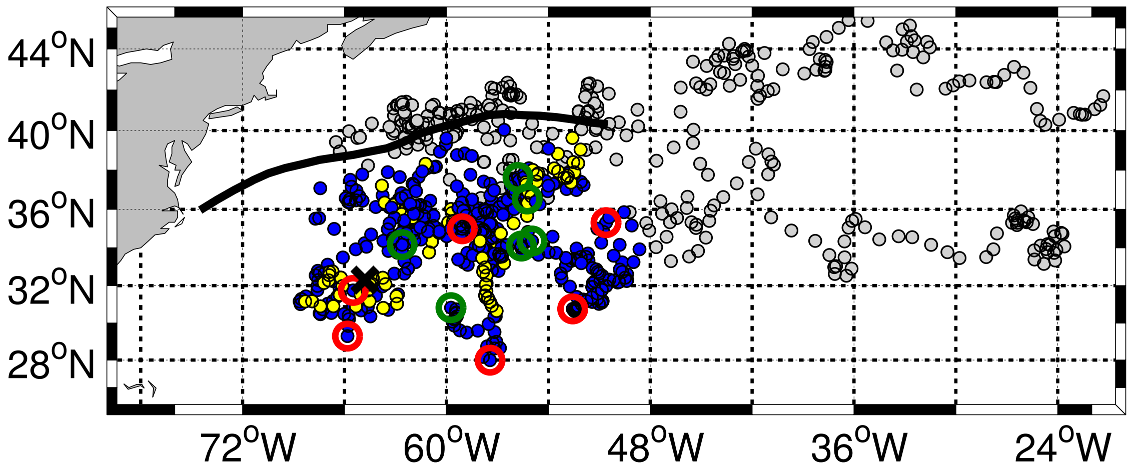

Figure 4.1: Profile locations of CLIMODE floats, November 2005 to April 2008. Grey dots indicate profiles not included in the averages presented in Figure 4.3. Yellow dots indicate profiles in February/March, when the deepest mixed layers occur in the region. Green circles indicate the first profile of a given float, while red circles indicate the last profile before a float stopped reporting. The location of Bermuda is marked by a black “x”. The mean Gulf Stream location during the sampling period is delineated by the thick black curve, calculated as the location at which the temperature at 200 m equals 15°C [*Fuglister*, 1963] using the Roemmich-Gilson Argo Climatology [*Roemmich and Gilson*, 2009].

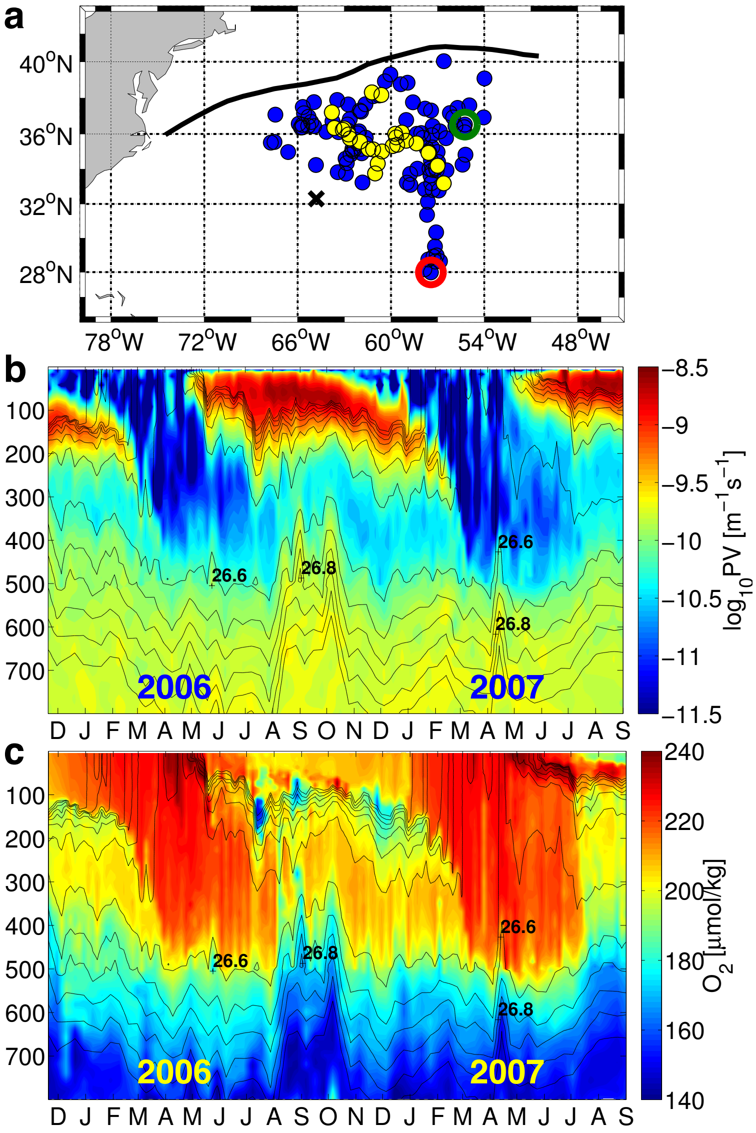

Figure 4.2: CLIMODE float "2721". Thin black curves are isopycnal contours, ranging from $\sigma_\theta = 25.8 - 28$ kg/m^3 on 0.1 kg/m^3 intervals. (a) Float profile locations, with the same features shown in Figure 4.1. (b) Log potential vorticity. (c) Oxygen concentration.

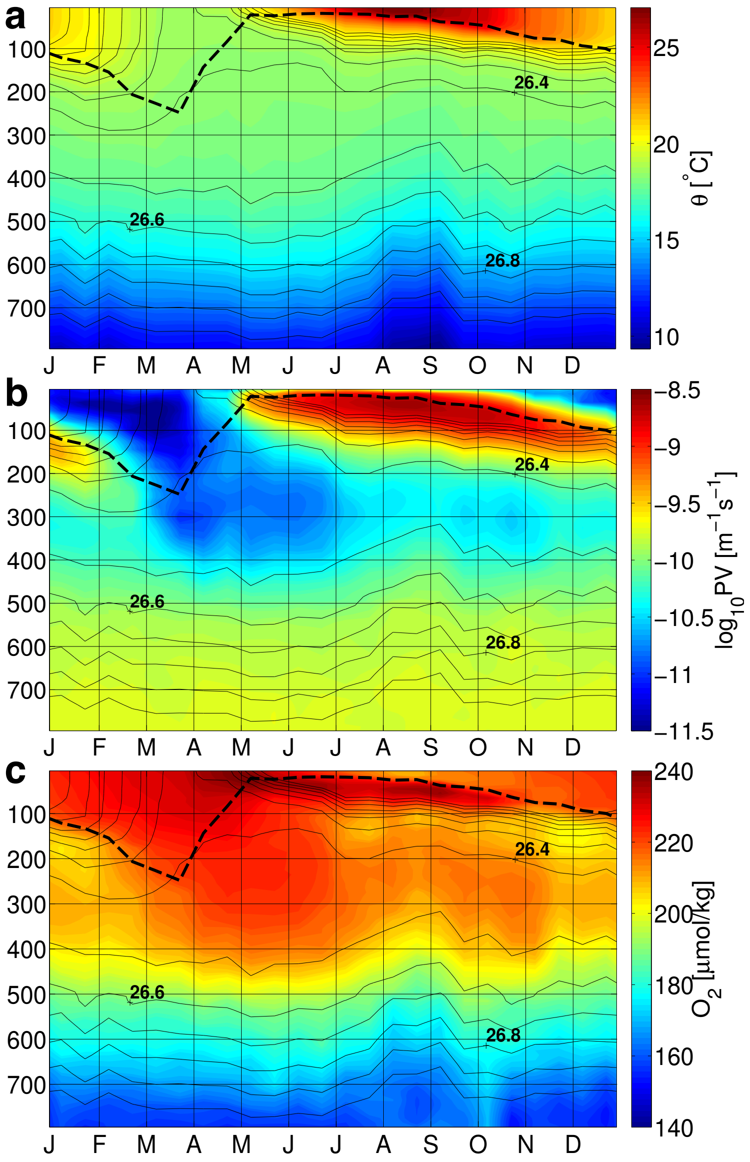

Figure 4.3: Annual mean of float profiles indicated by blue and yellow dots in Figure 4.1. Mean mixed layer depth is indicated by the black dashed curve. The mixed layer depth of a given profile is defined by the depth at which the difference in density exceeds a threshold of $\Delta\sigma_\theta = 0.03$ kg/m^3 from the density at 10 m depth [*de Boyer Montégut et al.*, 2004]. Thin black curves contour the same isopycnals as in Figure 4.2. (a) Potential temperature, θ. (b) Log potential vorticity. (c) Oxygen concentration.

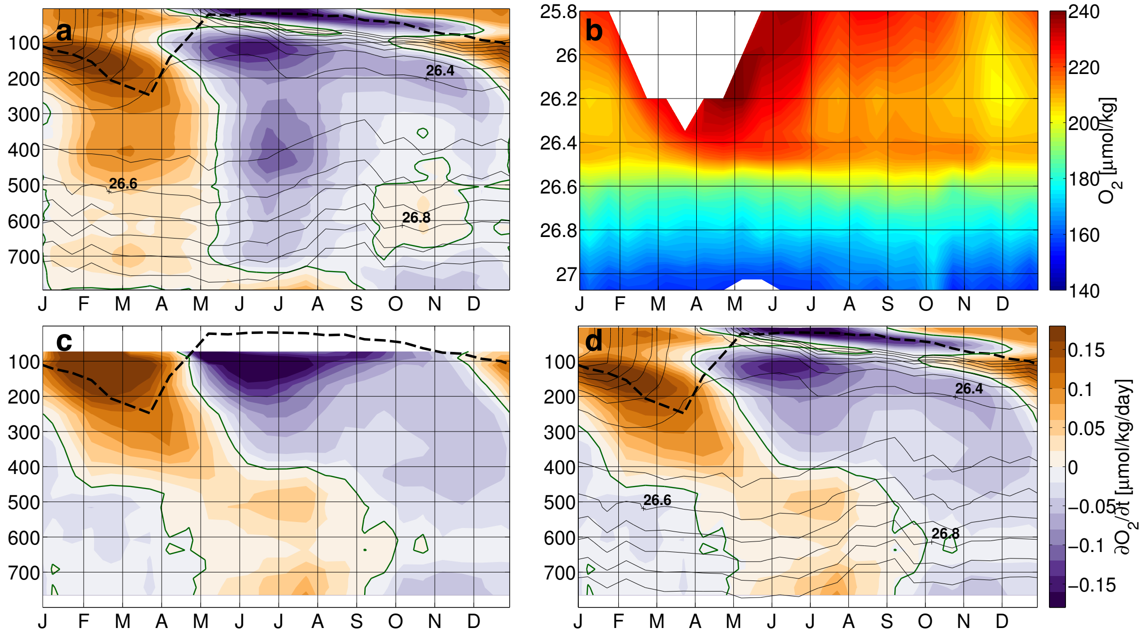

Figure 4.4: Oxygen rates of change and oxygen in isopycnal coordinates. Black dashed curve indicates mean mixed layer depth. (a) Oxygen rate of change, calculated along isobars from the values of Figure 4.3c. (b) Oxygen of Figure 4.3c, presented in isopycnal coordinates. (c) Oxygen rate of change, calculated along isopycnals from the values of Figure 4.4b, retranslated to depth coordinates using mean isopycnal depth. Depth range cut off above 73 m because that is the mean depth level of $\sigma_\theta = 25.8$ kg/m^3. (d) Oxygen rate of change, composed of the upper 250 m of Figure 4.4a and lower 250 m of Figure 4.4c.

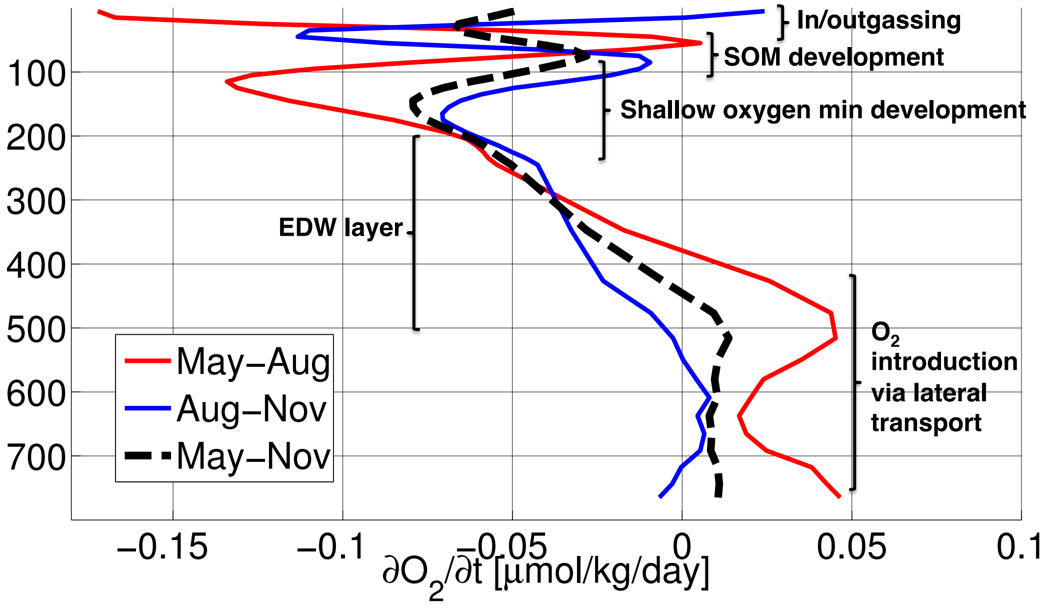

Figure 4.5: Average profiles of oxygen rate of change from Figure 4.4d. The solid black dashed curve represents the mean profile from May through November, while the red curve represents the mean profile from May to August and the blue curve the mean profile from August to November.

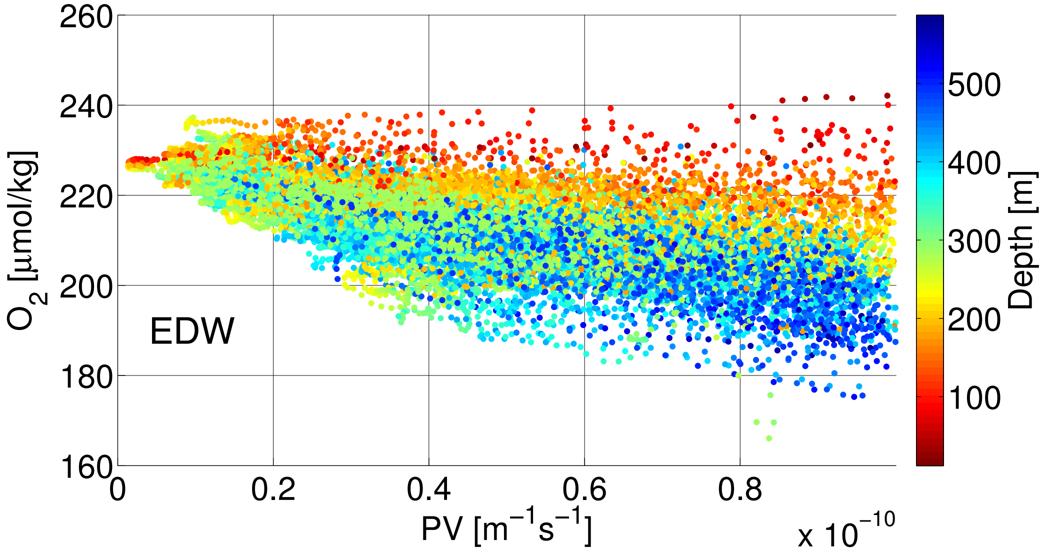

Figure 4.6: Potential vorticity vs. oxygen concentration within the EDW layer, using all CLIMODE float profile data.

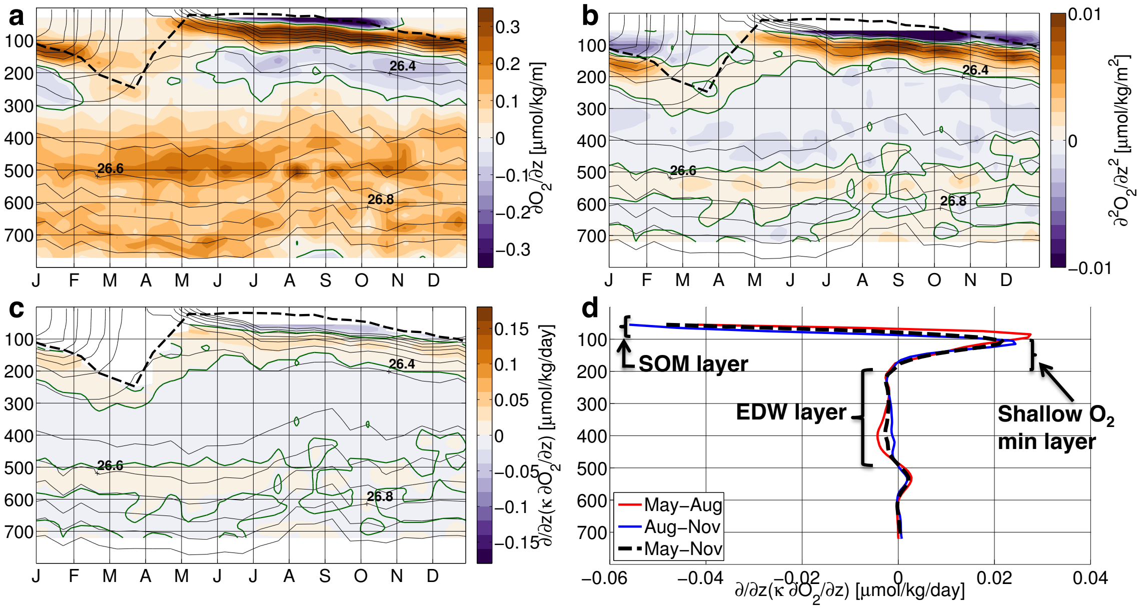

Figure 4.7: Oxygen vertical derivatives and mixing rate. (a) Vertical gradient of oxygen concentration presented in Figure 4.3c. Green curves delineate the zero contour. Mean mixed layer depth and isopycnal contours as in previous figures. (b) Second vertical derivative of oxygen concentration. Note the change in color scale to clarify vertical structure. (c) Vertical mixing rate of oxygen. The color scale matches Figure 4.4d for simple comparison. (d) Mean profiles of vertical oxygen mixing rate. Black dashed, red, and blue curves are averages over the time periods specified in Figure 4.5.

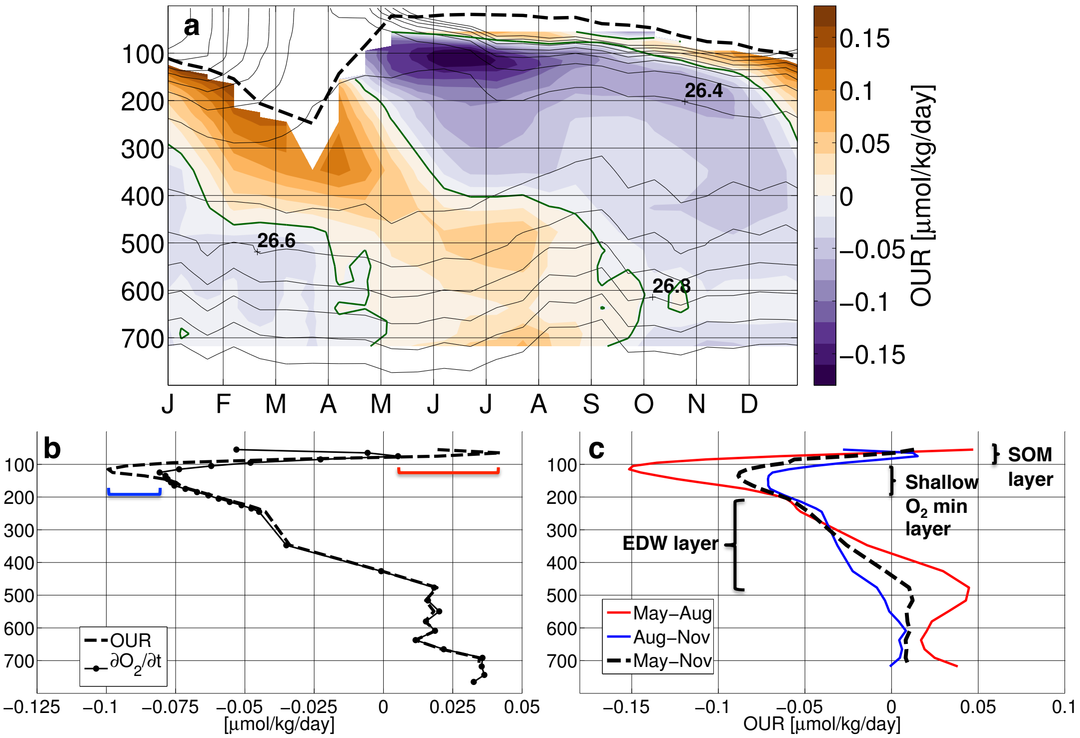

Figure 4.8: Oxygen utilization rate. (a) Oxygen utilization rate (OUR), obtained from subtracting the vertical mixing rate (Figure 4.7c) from the oxygen rate of change (Figure 4.4b). Mean mixed layer depth, zero contour, and isopycnal contours are indicated as in previous figures. (b) Mean August profiles of oxygen rate of change (Figure 4.4d) and OUR (Figure 4.8a). The red bar indicates the difference in maximum net production rate while the blue bar indicates the difference in maximum consumption rate. (c) Mean profiles of OUR, with dashed black, red, and blue curves indicating the mean over May to November, May to August, and August to November, respectively.

Bibliography

Alford, M. H. (2001), Internal swell generation: The spatial distribution of energy flux from the wind to mixed layer near-inertial motions, *J. Phys. Oceanogr.*, *31*(8), 2359–2368.

Anderson, L. A., and J. L. Sarmiento (1994), Redfield ratios of remineralization determined by nutrient data analysis, *Global biogeochemical cycles*, *8*(1), 65–80.

Bates, N. (2012), Multi-decadal uptake of carbon dioxide into subtropical mode water of the North Atlantic Ocean, *Biogeosciences*, *9*, 2649–2659.

Bates, N. R., A. C. Pequignet, R. J. Johnson, N. Gruber, et al. (2002), A short-term sink for atmospheric CO_2 in subtropical mode water of the North Atlantic Ocean, *Nature*, *420*(6915), 489–493.

Billheimer, S., and L. D. Talley (2013), Near cessation of Eighteen Degree Water renewal in the western North Atlantic in the warm winter of 2011–2012, *J. Geophys. Res. Oceans*, *118*(12), 6838–6853.

Billheimer, S., and L. D. Talley (2016a), Extraordinarily weak Eighteen Degree Water production concurs with strongly positive North Atlantic Oscillation in late winter 2014/15 [in “State of the Climate in 2015”], *Bull. Amer. Meteor. Soc.*, *97*(8), S78–S79.

Billheimer, S., and L. D. Talley (2016b), Annual cycle and destruction of Eighteen Degree Water, *J. Geophys. Res. Oceans*, doi:10.1002/2016JC011799.

Boccaletti, G., R. Ferrari, and B. Fox-Kemper (2007), Mixed layer instabilities and restratification, *J. Phys. Oceanogr.*, *37*(9), 2228–2250.

Brix, H., N. Gruber, D. M. Karl, and N. R. Bates (2006), On the relationships between primary, net community, and export production in subtropical gyres, *Deep Sea Res. Part II*, *53*(5), 698–717.

Bushinsky, S. M., and S. Emerson (2015), Marine biological production from in situ oxygen measurements on a profiling float in the subarctic Pacific Ocean, *Global Biogeochemical Cycles*, *29*(12), 2050–2060.

Carlson, C. A., H. W. Ducklow, A. F. Michaels, et al. (1994), Annual flux of dissolved organic carbon from the euphotic zone in the northwestern Sargasso Sea, *Nature*, *371*(6496), 405–408.

Cerovečki, I., L. D. Talley, and M. R. Mazloff (2011), A comparison of Southern Ocean air-sea buoyancy flux from an ocean state estimate with five other products, *J. Clim.*, *24*(24), 6283–6306.

Chaigneau, A., O. Pizarro, and W. Rojas (2008), Global climatology of near-inertial current characteristics from Lagrangian observations, *Geophys. Res. Lett.*, *35*(13).

Cole, S. T., C. Wortham, E. Kunze, and W. B. Owens (2015), Eddy stirring and horizontal diffusivity from Argo float observations: Geographic and depth variability, *Geophys. Res. Lett.*, *42*(10), 3989–3997.

Curry, R. G., and M. S. McCartney (2001), Ocean gyre circulation changes associated with the North Atlantic Oscillation, *J. Phys. Oceanogr.*, *31*(12), 3374–3400.

Czaja, A., and U. Hausmann (2009), Observations of entry and exit of potential vorticity at the sea surface, *J. Phys. Oceanogr.*, *39*(9), 2280–2294.

Davis, R. E. (1982), On relating Eulerian and Lagrangian velocity statistics: single particles in homogeneous flows, *J. Fluid Mech.*, *114*, 1–26.

de Boyer Montégut, C., G. Madec, A. S. Fischer, A. Lazar, and D. Iudicone (2004), Mixed layer depth over the global ocean: An examination of profile data and a profile-based climatology, *J. Geophys. Res.*, *109*, C12003, doi:10.1029/2004JC002378.

Deremble, B., and W. Dewar (2013), Volume and potential vorticity budgets of Eighteen Degree Water, *J. Phys. Oceanogr.*, *43*(11), 2309–2321.

deSzoeke, R. A., and M. D. Levine (1981), The advective flux of heat by mean geostrophic motions in the Southern Ocean, *Deep Sea Res.*, *28A*(10), 1057–1085.

Dickson, R., J. Lazier, J. Meincke, P. Rhines, and J. Swift (1996), Long-term coordinated changes in the convective activity of the North Atlantic, *Prog. Oceanogr.*, *38*(3), 241–295.

Dong, S., and K. A. Kelly (2004), Heat budget in the Gulf Stream region: The importance of heat storage and advection, *J. Phys. Oceanogr.*, *34*(5), 1214–1231.

Dong, S., S. L. Hautala, and K. A. Kelly (2007), Interannual variations in upper-ocean heat content and heat transport convergence in the western North Atlantic, *J. Phys. Oceanogr.*, *37*(11), 2682–2697.

Emerson, S. (2014), Annual net community production and the biological carbon flux in the ocean, *Global Biogeochemical Cycles*, *28*(1), 14–28.

Forget, G., G. Maze, M. Buckley, and J. Marshall (2011), Estimated seasonal cycle of North Atlantic eighteen degree water volume, *J. Phys. Oceanogr.*, *41*(2), 269–286.

Fratantoni, D. M., Y.-O. Kwon, and B. A. Hodges (2013), Direct observation of subtropical mode water circulation in the western North Atlantic Ocean, *Deep Sea Res. Part II*, doi:10.1016/j.dsr2.2013.02.027.

Fuglister, F. C. (1963), Gulf Stream 60, *Prog. Oceanogr.*, *1*, 265–373.

Gill, A. E. (1982), *Atmosphere-ocean dynamics*, vol. 30, Academic Press.

Hausmann, U., and A. Czaja (2012), The observed signature of mesoscale eddies in sea surface temperature and the associated heat transport, *Deep Sea Res. Part I*, *70*, 6072.

Haynes, P., and M. McIntyre (1987), On the evolution of vorticity and potential vorticity in the presence of diabatic heating and frictional or other forces, *J. Atmos. Sci.*, *44*(5), 828–841.

Hennon, T. D., S. C. Riser, and S. Mecking (2016), Profiling float-based observations of net respiration beneath the mixed layer, *Global Biogeochemical Cycles*.

Hurrell, J. W., Y. Kushnir, G. Ottersen, and M. Visbeck (Eds.) (2003), *The North Atlantic Oscillation: climatic significance and environmental impact*, vol. 134, American Geophysical Union, Washington, D.C., doi:10.1029/GM134.

Inoue, R., M. Gregg, and R. Harcourt (2010), Mixing rates across the Gulf Stream, part 1: on the formation of eighteen degree water, *J. Mar. Res.*, *68*(5), 643–671.

Jenkins, W. (1980), Tritium and he-3 in the Sargasso Sea, *J. Mar. Res.*, *38*(3), 533–569.

Jenkins, W. (1982), Oxygen utilization rates in North Atlantic subtropical gyre and primary production in oligotrophic systems, *Nature*, *300*(5889), 246–248.

Jenkins, W. J. (1987), 3h and 3he in the Beta Triangle: Observations of gyre ventilation and oxygen utilization rates, *J. Phys. Oceanogr.*, *17*(6), 763–783.

Jenkins, W. J., and J. C. Goldman (1985), Seasonal oxygen cycling and primary production in the Sargasso Sea, *J. Mar. Res.*, *43*, 465–491.

Johnson, G. C., J. M. Toole, and N. G. Larson (2007), Sensor corrections for Sea-Bird SBE-41CP and SBE-41 CTDs*, *J. Atmos. Oceanic Technol.*, *24*(6), 1117–1130.

Joyce, T. M. (2012), New perspectives on eighteen-degree water formation in the North Atlantic, *J. Oceanogr.*, *68*(1), 45–52.

Joyce, T. M., R. S. Pickart, and R. C. Millard (1999), Long-term hydrographic changes at 52 and 66°w in the North Atlantic Subtropical Gyre and Caribbean, *Deep Sea Res. Part II*, *46*, 245–278.

Joyce, T. M., C. Deser, and M. A. Spall (2000), The relation between decadal variability of subtropical mode water and the North Atlantic Oscillation, *J. Clim.*, *13*(14), 2550–2569.

Joyce, T. M., L. N. Thomas, and F. B. Bahr (2009), Wintertime observations of Subtropical Mode Water formation within the Gulf Stream, *Geophys. Res. Lett.*, *36*, L02607, doi:10.1029/2008GL035918.

Joyce, T. M., L. N. Thomas, W. K. Dewar, and J. B. Girton (2013), Eighteen Degree Water formation within the Gulf Stream during CLIMODE, *Deep Sea Res. Part II*, doi: 10.1016/j.dsr2.2013.02.019.

Kalnay, E., M. Kanamitsu, R. Kistler, W. Collins, D. Deaven, L. Gandin, M. Iredell, S. Saha, G. White, J. Woollen, Y. Zhu, A. Leetmaa, and R. Reynolds (1996), The NCEP/NCAR 40-year reanalysis project, *Bull. Amer. Meteor. Soc.*, *77*(3), 437–471.

Kelly, K. A., and S. Dong (2013), The contributions of atmosphere and ocean to North Atlantic subtropical mode water volume anomalies, *Deep Sea Res. Part II*, doi: 10.1016/j.dsr2.2013.02.020.

Knutson, T. R., F. Zeng, and A. T. Wittenberg (2013), The extreme March–May 2012 warm anomaly over the eastern United States: Global context and multimodel trend analysis [in "Explaining Extreme Events of 2012 from a Climate Perspective"], *Bull. Amer. Meteor. Soc.*, *94*(9), S13–S17.

Körtzinger, A., J. Schimanski, and U. Send (2005), High quality oxygen measurements from profiling floats: A promising new technique, *J. Atmos. Oceanic Technol.*, *22*(3), 302–308.

Kwon, Y.-O., and S. C. Riser (2004), North Atlantic Subtropical Mode Water: A history of ocean-atmosphere interaction 1961–2000, *Geophys. Res. Lett.*, *31*(19), L19,307.

Kwon, Y.-O., and S. C. Riser (2005), General circulation of the western subtropical North Atlantic observed using profiling floats, *J. Geophys. Res.*, *110*, C10012, doi: 10.1029/2005JC002909.

Kwon, Y.-O., J.-J. Park, S. F. Gary, and M. S. Lozier (2015), Year-to-year reoutcropping of Eighteen Degree Water in an eddy-resolving ocean simulation, *J. Phys. Oceanogr.*, *45*(4), 1189–1204.

Ledwell, J. R., A. J. Watson, and C. S. Law (1993), Evidence for slow mixing across the pycnocline from an open-ocean tracer-release experiment, *Nature*, *364*(6439), 701–703.

Lumpkin, R., A.-M. Treguier, and K. Speer (2002), Lagrangian eddy scales in the northern Atlantic Ocean, *J. Phys. Oceanogr.*, *32*(9), 2425–2440.

Marshall, J., A. Andersson, N. Bates, W. Brown, W. Dewar, S. Doney, J. Edson, R. Ferrari, G. Forget, D. Fratantoni, M. Gregg, T. Joyce, K. Kelly, S. Lozier, R. Lumpkin, G. Maze, J. Palter, A. Plueddemann, R. Samelson, K. Silverthorne, E. Skyllingstad, F. Straneo, L. Talley, L. Thomas, J. Toole, and R. Weller (2009), The CLIMODE field campaign: Observing the cycle of convection and restratification over the Gulf Stream, *Bull. Amer. Meteor. Soc.*, *90*, 1337–1350, doi:10.1175/2009BAMS2706.1.

Martin, J. H., G. A. Knauer, D. M. Karl, and W. W. Broenkow (1987), VERTEX: carbon cycling in the northeast Pacific, *Deep Sea Res.*, *34*(2), 267–285.

Martz, T. R., K. S. Johnson, and S. C. Riser (2008), Ocean metabolism observed with oxygen sensors on profiling floats in the South Pacific, *Limnol. Oceanogr.*, *53*(5), 2094–2111.

Maze, G., and J. Marshall (2011), Diagnosing the observed seasonal cycle of Atlantic subtropical mode water using potential vorticity and its attendant theorems, *J. Phys. Oceanogr.*, *41*(10), 1986–1999.

Maze, G., G. Forget, M. Buckley, J. Marshall, and I. Cerovečki (2009), Using transformation and formation maps to study the role of air-sea heat fluxes in North Atlantic Eighteen Degree Water formation, *Journal of Physical Oceanography*, *39*(8), 1818–1835.

Michaels, A. F., and A. H. Knap (1996), Overview of the US JGOFS Bermuda Atlantic Time-series Study and the Hydrostation S program, *Deep Sea Res. Part II*, *43*(2), 157–198.

Newton, C. W. (1961), Estimates of vertical motions and meridional heat exchange in Gulf Stream eddies, and a comparison with atmospheric disturbances, *J. Geophys. Res.*, *66*(3), 853–870.

NOAA National Climatic Data Center (2012), State of the climate: National overview for March 2012, *URL http://www.ncdc.noaa.gov/sotc/national/2012/3*, NOAA, published online April 2012, retrieved on 23 March 2013 from http://www.ncdc.noaa.gov/sotc/national/2012/3.

Ono, S., A. Ennyu, R. Najjar, and N. Bates (2001), Shallow remineralization in the Sargasso Sea estimated from seasonal variations in oxygen, dissolved inorganic carbon and nitrate, *Deep Sea Res. Part II*, *48*(8), 1567–1582.

Owens, W. B., and A. P. Wong (2009), An improved calibration method for the drift of the conductivity sensor on autonomous CTD profiling floats by θ–s climatology, *Deep Sea Res. Part I*, *56*(3), 450–457.

Palter, J. B., M. S. Lozier, and R. T. Barber (2005), The effect of advection on the nutrient reservoir in the North Atlantic subtropical gyre, *Nature*, *437*(7059), 687–692.

Peterson, T. C., M. P. Hoerling, P. A. Stott, and S. C. Herring (2013), Explaining extreme events of 2012 from a climate perspective, *Bull. Amer. Meteor. Soc.*, *94*(9), S1–S74.

Qiu, B., and S. Chen (2006), Decadal variability in the formation of the North Pacific Subtropical Mode Water: Oceanic versus atmospheric control, *J. Phys. Oceanogr.*, *36*(7), 1365–1380.

Qiu, B., P. Hacker, S. Chen, K. Donohue, D. Watts, H. Mitsudera, N. Hogg, and S. Jayne (2006), Observations of the subtropical mode water evolution from the Kuroshio Extension, *J. Phys. Oceanogr.*, *36*, 457–473.

Rakestraw, N. W., and D. E. Carritt (1948), Some seasonal chemical changes in the open ocean, *J. Mar. Res.*, *7*, 362–368.

Reynolds, R. W., T. M. Smith, C. Liu, D. B. Chelton, K. S. Casey, and M. G. Schlax (2007), Daily high-resolution blended analyses for sea surface temperature, *J. Clim.*, *20*, 5473–5496.

Riley, G. A. (1951), *Oxygen, phosphate, and nitrate in the Atlantic Ocean*, vol. 13, Bingham Oceanographic Laboratory.

Rintoul, S. R., and C. Wunsch (1991), Mass, heat, oxygen and nutrient fluxes and budgets in the North Atlantic Ocean, *Deep Sea Res.*, *38*, S355–S377.

Riser, S. C., and K. S. Johnson (2008), Net production of oxygen in the subtropical ocean, *Nature*, *451*(7176), 323–325.

Roemmich, D., and J. Gilson (2009), The 2004–2008 mean and annual cycle of temperature, salinity, and steric height in the global ocean from the Argo Program, *Prog. Oceanogr.*, *82*(2), 81–100.

Sarmiento, J. L., G. Thiele, R. M. Key, and W. S. Moore (1990), Oxygen and nitrate new production and remineralization in the North Atlantic subtropical gyre, *J. Geophys. Res. Oceans*, *95*(C10), 18,303–18,315.

Shcherbina, A. Y., M. A. Sundermeyer, E. Kunze, E. DAsaro, G. Badin, D. Birch, A.-M. E. Brunner-Suzuki, J. Callies, B. T. Kuebel Cervantes, M. Claret, et al. (2015), The LatMix summer campaign: Submesoscale stirring in the upper ocean, *Bull. Amer. Meteor. Soc.*, *96*(8), 1257–1279.

Shulenberger, E., and J. L. Reid (1981), The Pacific shallow oxygen maximum, deep chlorophyll maximum, and primary productivity, reconsidered, *Deep Sea Res. Part I*, *28*(9), 901–919.

Talley, L. D. (1996), North Atlantic circulation and variability, reviewed for the CNLS conference, *Physica D*, *98*(2), 625–646.

Talley, L. D., and M. Raymer (1982), Eighteen degree water variability, *J. Mar. Res.*, *40*, 757–775.

Thomas, L. N. (2005), Destruction of potential vorticity by winds, *J. Phys. Oceanogr.*, *35*(12), 2457–2466.

Thomas, L. N., J. R. Taylor, R. Ferrari, and T. M. Joyce (2013), Symmetric instability in the Gulf Stream, *Deep Sea Res. Part II*, doi:10.1016/j.dsr2.2013.02.025.

Uchida, H., T. Kawano, I. Kaneko, and M. Fukasawa (2008), In situ calibration of optode-based oxygen sensors, *J. Atmos. Oceanic Technol.*, *25*(12), 2271–2281.

Vivier, F., K. A. Kelly, and L. A. Thompson (2002), Heat budget in the Kuroshio Extension region: 1993-99, *J. Phys. Oceanogr.*, *32*(12), 3436–3454.

Whalen, C., L. Talley, and J. MacKinnon (2012), Spatial and temporal variability of global ocean mixing inferred from Argo profiles, *Geophys. Res. Lett.*, *39*(18), L18612, doi: 10.1029/2012GL053196.

Whalen, C. B., J. A. MacKinnon, L. D. Talley, and A. F. Waterhouse (2015), Estimating the mean diapycnal mixing using a finescale strain parameterization, *J. Phys. Oceanogr.*, *45*(4), 1174–1188.

Worthington, L. (1977), Intensification of the Gulf Stream after the winter of 1976-77, *Nature*, *270*, 415–417.

Worthington, L. V. (1959), The 18° water in the Sargasso Sea, *Deep Sea Res.*, *5*, 297–305.

Worthington, L. V. (1972a), Negative oceanic heat flux as a cause of water-mass formation, *J. Phys. Oceanogr.*, *2*(3), 205–211.

Worthington, L. V. (1972b), *Anticyclogenesis in the oceans as a result of outbreaks of continental polar air*, Woods Hole Oceanographic Institution.

Wunsch, C. (1999), Where do ocean eddy heat fluxes matter?, *J. Geophys. Res.*, *104*(C6), 13,235–13.

Yu, L. (2007), Global variations in oceanic evaporation (1958-2005): The role of the changing wind speed, *J. Clim.*, *20*(21), 5376–5390.

Zeng, X., M. Zhao, and R. E. Dickinson (1998), Intercomparison of bulk aerodynamic algorithms for the computation of sea surface fluxes using TOGA COARE and TAO data, *J. Clim.*, *11*, 2628–2644.